STRESS AND FATIGUE ANALYSIS OF SVI-TESTED CAMSHAFT LOBES

by

Jose Alejandro Escobar

Thesis submitted to the faculty of
Virginia Polytechnic Institute and State University
in partial fulfillment of the requirements for the degree of

Master of Science
in
Materials Science and Engineering

APPROVED:

Dr. Robert W. Hendricks, Chairman
Dr. Stephen L.Kampe
Dr. Ronald W.Landgraf
Dr. William T. Reynolds

November, 1996

Keywords: camshaft lobes, grinding residual stress, fatigue life prediction, rolling contact stress, fatigue engine testing, fracture surfaces, thermal damage

STRESS AND FATIGUE ANALYSIS OF SVI-TESTED CAMSHAFT LOBES

by

Jose Alejandro Escobar

Dr. Robert W. Hendricks, Chairman
Materials Science and Engineering

(ABSTRACT)

Nondestructive evaluation techniques were employed to fully characterize three 2.3L camshafts tested in an engine simulator for an equivalent of 100,000 miles. Optical microscopy, acoustic microscopy (SAM), and profilometry were used to characterize wear and fatigue, crack depth, and surface roughness, respectively. Results show cracking to occur mainly in the opening ramp of the most abusively ground cam lobes. No clear evidence was found for subsurface cracking at depths as great as 200 μm from the lobe s surface. Profilometry results show no evidence of any major tribological effect due to the sliding friction of the follower.

Fractography studies show a difference between fracture surfaces among the cracks examined; straight cracks exhibit features resembling fatigue propagation, while fracture surfaces from pitted cracks show a more brittle behavior. Small grinding cracks (approximately 300 μm in length) were found in the opening ramps of the most abusively ground lobes prior to testing. Knoop and Nanoindenter microhardness indicate a near-surface rehardening for the most abusively ground lobe (confirmed by metallography), and temper burn for the remaining lobes. X-ray residual stress results made in the opening ramp of the tested lobes show evidence of residual stress relaxation. X-ray line width data as a function of depth does not correlate with residual stress.

ACKNOWLEDGMENTS

Financial support for this research was provided under the National Science Foundation Strategic Manufacturing Initiative project #230-11-110F-108-323622-1 (sponsor number DDM-9215629), Ford Motor Company, and Landis (division of Western Atlas). Other organizations that contributed by providing parts and services include the following: American Stress Technologies, Presta Someflor, Oak Ridge National Laboratory and Scintag Inc.

Industrial participation in this project was intense, and I would like to recognize several key researchers and engineers who gave of their time, research materials, and special knowledge to enhance the quality of the work presented herein:

- Jim DeVerna, John Glowa, and Ming Loo of Ford Motor Company for providing practical research goals,
- Bill Pflager and David Horst at Landis for generously assisting and providing the instruments for surface roughness measurements,
- Mike Vinarcik at Ford s Central Laboratory for help with sample preparation,
- Laura Ritcher at Oak Ridge National Lab for her help on the operation of the Nanoindenter. Laura volunteered time over weekends to perform microhardness measurements.
- William English at GE Superabrasives for his help and suggestions in developing a design of experiment,
- Thomas Geer at Oak Ridge National Lab for his assistance in metallography studies and the use of the Knoop indenter,
- Mac McCord at Virginia Tech, for his guidance and assistance during scanning acoustic microscopy studies, and
- Bill Shaver at Virginia Tech s ESM machine shop for always accommodating time for camshaft cutting on last-minute request.

I would also like to thank the students that worked on this project for their help and guidance: Heidi Allison, Greg Moller, Brian Biggi, Bill Cooper and Andrew Galloway. Gratitude is also expressed to the office staff of the Materials Science and Engineering department: Jan Doran, Amy Hill and Suzzette Sowers.

Special thanks should be given to my committee members. I would like to acknowledge their comments and suggestions, which was crucial for the successful completion of this project: Professor Robert W. Hendricks, my advisor, whose guidance and work ethics had a profound impression on my work and in my persona. Professor Ronald W. Landgraf, provided invaluable assistance in fatigue-related mechanisms. Professor William T. Reynolds helped me with the metallurgical aspects of the project. Professor Stephen L. Kampe, whose knowledge in physical metallurgy was of great importance in my research. Professor Norman E. Dowling, though not part of the committee, gave advice and assistance on the experimental setup.

Finally, my greatest debt goes to my family who supported me through good and bad times. My father Ricardo, whose fortitude in character and wisdom I will always admire. My mother Marcela, whose love and affection always shine light at every step of my life, and my brother Esteban, whose competitive nature and athletic ability served as inspiration for self-improvement.

Table of Contents

List of Figures

List of Tables

Chapter 1

INTRODUCTION

Split second timing is essential for the smooth and powerful running in a car engine. It is achieved by the engine s camshaft and crankshaft working in concert. As the pistons move up and down in the cylinders, they drive the crankshaft which turns the flywheel and, ultimately, the wheels. But, through a chain linkage, the crankshaft also turns the camshaft. As the camshaft rotates, the cams operate the cylinder valves. ¾ David Macaulay, The Way Things Work

One of the main concerns of engineers in the field of internal combustion engines is to reliably predict and extend the service life of a camshaft. Fatigue performance of a camshaft is influenced by a host of variables such as cam material, lift profile, valvetrain configuration and manufacturing processes. Major efforts are currently underway in the manufacturing industry to characterize the effects of grinding on the lifetime performance of a cam. Camshaft lobes are ground to produce the desired lift profile and surface finish. Manufacturers have found that the quality and service life of a camshaft is related to the way in which the camshaft is ground (gentle, moderate, abusive).

Mass production grinding of camshafts involve millions of parts. Output production rates are sometimes inherently limited by the detrimental effect of grinding thermal damage to the workpiece. A link between grinding process and engineering design of a camshaft is necessary to meet the demands for higher production rates as well as to secure a ever-more efficient design. This project addresses this problem by characterizing the fatigue life performance of ground camshafts in a simulated engine environment and correlating the results with the effects of grinding.

1.1 The Valvetrain: The Role of the Camshaft

The valvetrain is composed of an array of parts such as the cam followers, pushrods, rocker arms and shafts, valves, springs, retainers, rotators, seals, and locks. Its purpose is to open and close the intake and exhaust ports that lead to the combustion chamber. Figure 1.1 shows a cut away view of an internal combustion engine, showing the location of the camshaft with respect to other valvetrain components.

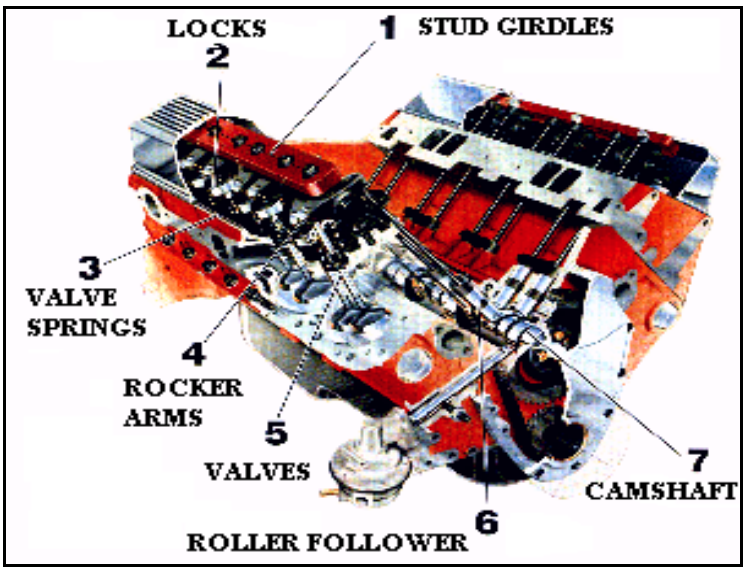

Figure 1.1 Combustion engine showing components of the valvetrain.

The camshaft s function in an engine is to open and close the valves. Its design results in valves being opened and closed at a controlled rate of speed as well as at a precise time in relation to piston position. Camshafts normally have two lobes per cylinder, one to drive the intake valve and one to drive the exhaust valve. Thus, a V4-engine will have a camshaft with eight lobes. Figure 1.2 shows a typical camshaft and its parts.

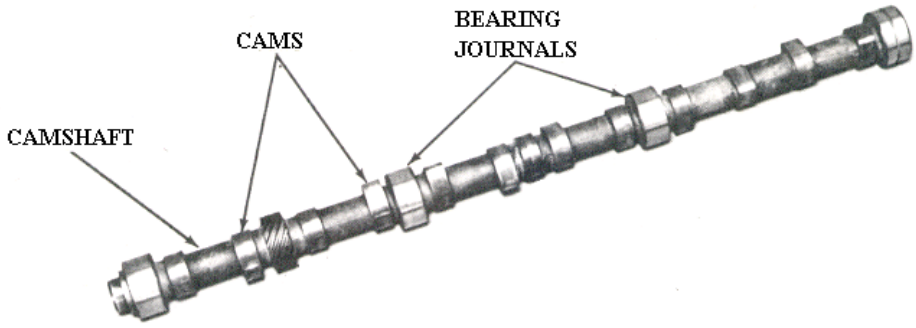

Figure 1.2 Typical camshaft in an internal combustion engine with camshaft parts named

The part of the valvetrain in direct contact with the cam is the follower or lifter. Generally there are two kinds of followers: flat-faced and roller. One of the advantages of

the roller follower over the flat-faced follower is that it reduces the friction loads due to its rolling nature, thereby reducing valvetrain noise and enhancing engine performance. However, the roller follower s geometry dictates reduced contact area with the cam which increases contact stresses at the interface. If we considered the fact that a car at its 100,000 mile mark will have subjected the cams to over 120 million cyclic revolutions, this increase in contact stress becomes an important factor in the study of the wear mechanisms of the part. Figure 1.3 shows a schematic of the valvetrain components.

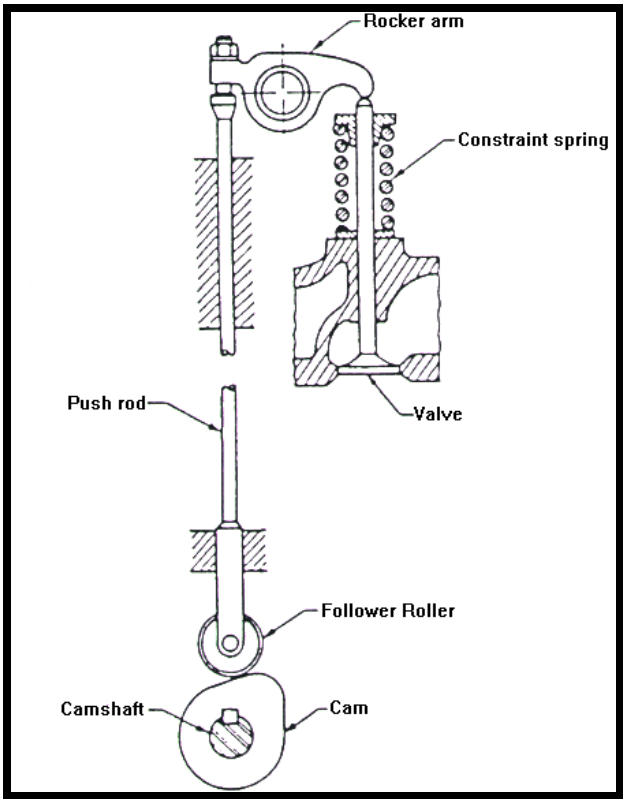

Figure 1.3 Overhead valve and roller-follower configuration[1].

1.2 Camshaft Nomenclature

Three camshafts manufactured by Presta Someflor in Liechtenstein were received from Ford Motor company for this study. These camshafts (labeled V-11, V-13, and V-15) are designed for a four cylinder engine, and thus each contains eight lobes. They are assembled from a hollow steel tube with forged 52100 steel lobes press fitted to the surface. The head of each camshaft is characterized by a protruding journal, and each lobe is numbered from this end (see Figure 1.4). The three 2.3L camshafts were chosen to permit life testing in a pushrod-type camshaft test fixture designed by Specialized Vehicles International (SVI).

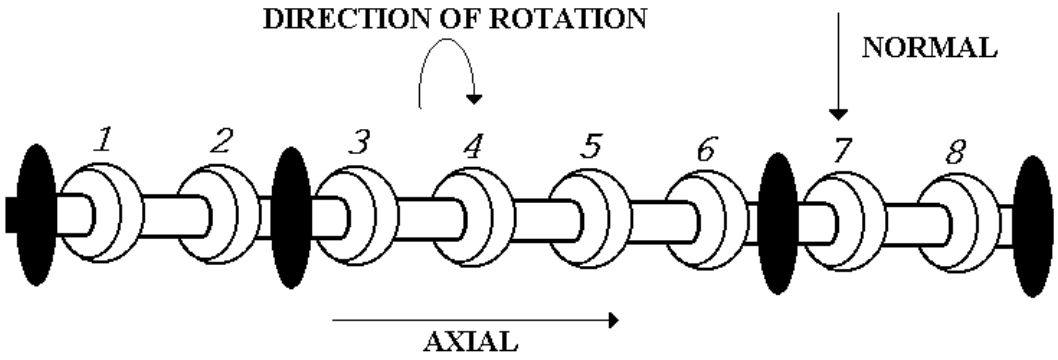

Figure 1.4 Camshaft nomenclature

The arrows indicate the different directions in which experimental measurements could be made. The direction of rotation of the camshaft as it opens and closes the valves is illustrated as a clockwise revolution, which also corresponds with the direction of grinding.

1.3 General Overview of Cam Lobes

The cam lobes convert the rotary motion of the camshaft to reciprocating motion of the valve train and valves. The design of the cam lobe contour has a major effect on engine performance. The amount of valve opening, how long the valve remains open, when the valves open and close, and the speed at which valves open and close are all determined by cam lobe design[2]. Figure 1.5 depicts a typical cam and its distinct regions.

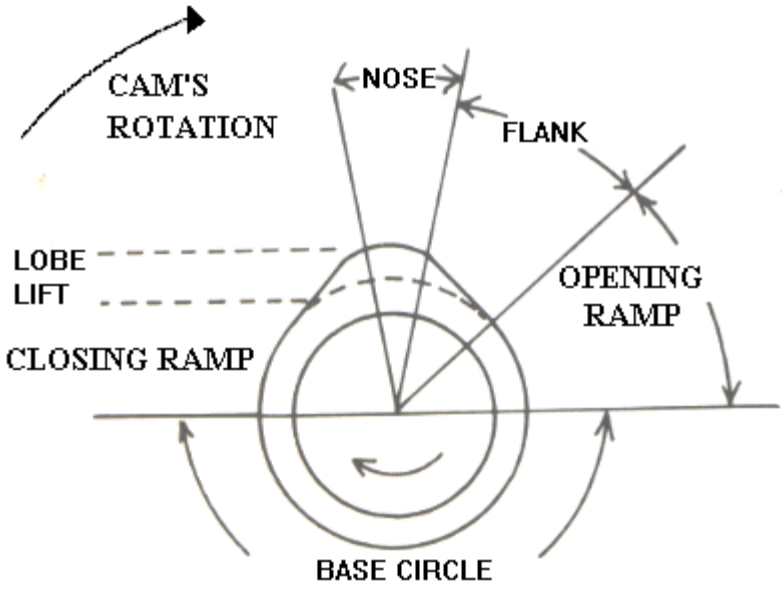

Figure 1.5 Cam Lobe terminology.

The camshaft rotates in a clockwise direction. Four regions are identified starting from the bottom in a counter-clockwise direction: base circle, opening ramp, nose and closing ramp. Each region is identified by degree locations, starting at 0° at the nose, 60° at the closing ramp, 180° at the base circle, and 300° at the opening ramp.

Camshaft lobe wear is caused by friction between the cam lobe and the cam follower. Insufficient lubrication, excessive valve spring tension, excessive valve lash, hydraulic lifter failure, and dirty oil will contribute to early and rapid wear[3]. Worn cam lobes retard valve timing which is detrimental to engine power and performance.

1.4 Scope of the Project

The objective of this research is to perform an examination of the fatigue failure life of camshaft lobes tested to 100,000 miles in engine simulator as a function of abusive grinding processes. The engine simulator is a special test fixture manufactured by Specialized Vehicles Inc. (SVI) to Ford design, and hereafter is referred as the SVI. Experimental results will be used to develop a method that will link the grinding process to the product lifetime through a fatigue life model developed previously[4]. This study is sponsored by Ford Motor Company with participation from Landis, General Electric, American Stress Technologies, and under the auspices of a National Science Foundation Strategic Manufacturing Initiative.

The overall project is divided into three parts: sample preparation, nondestructive evaluation (NDE), and destructive testing. Figure 1.6 shows a diagram of the different stages in the experiment design.

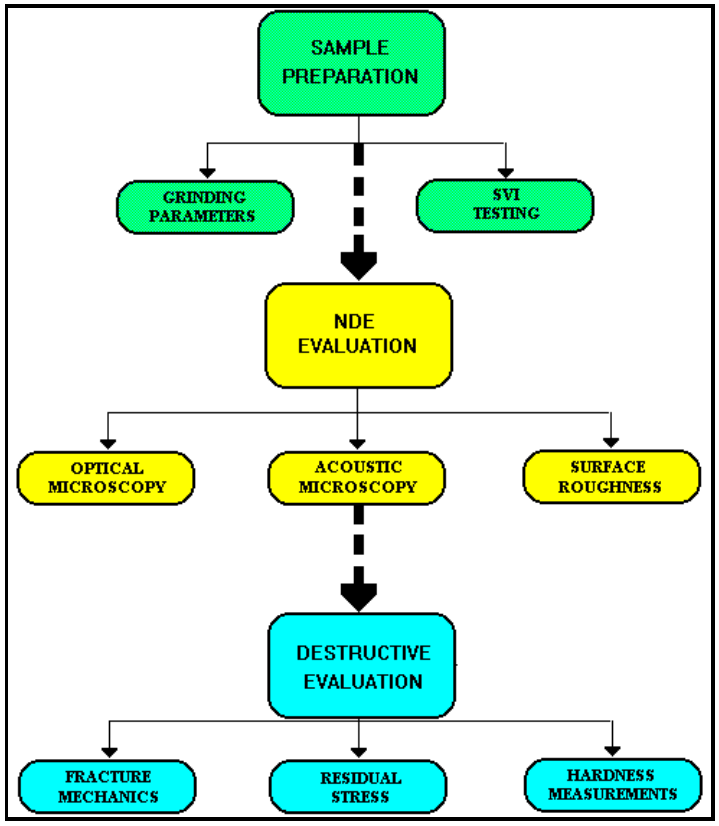

Figure 1.6. Basic structure of the research project: level 1(green) involves sample preparation, level 2 (yellow) comprises all NDE techniques used and level 3 (blue) shows the main destructive techniques used.

Chapter 2

BACKGROUND RESEARCH

The aims of pure science, unlike those of applied science, are neither fast-flowing nor pragmatic. The quick harvest of applied science is the usable process, the medicine, the machine. The shy fruit of pure science is understanding. - Lincoln Barnett

The material presented in this chapter is divided into three sections: First, the reader is introduced to experimental research done prior to the inception of this project. Topics include grinding protocol, X-ray residual stress data, and accelerated lifetime testing using an engine simulator. Next, a review of the properties and manufacturing processes of a cam is presented. Finally, a general overview of the mechanisms of thermal damage during grinding is given.

2.1 Grinding Protocol

The lobes of three 2.3L camshafts were abusively ground to induce cracking during subsequent life testing. The camshafts are labeled as V-11, V-13, and V-15. Grinding of the camshafts was done by Scott Courtney[5] at Landis (division of Western Atlas Inc.) using a research version of their Landis 3L-CNC cam lobe grinder.

In order to correlate the induced residual stress due to grinding with the part s fatigue life, the eight lobes in each of the camshafts were ground with various depths of cut (depth of cut is defined as how far into the material the grinding wheel channels in a single pass). Table 2.1 shows the depth of cut per grinding pass used in this experiment:

Table 2.1 Depth of Cut per Grinding Pass by Lobe Number

LOBE #	GRINDING PASSES	SINGLE PASS DEPTH OF CUT (mm)	TOTAL MATERIAL REMOVED (mm)
Lobe 8	16	0.03	.480
Lobe 7	12	0.04	.480
Lobe 6	10	0.05	.500
Lobe 5	8	0.06	.480
Lobe 4	7	0.07	.490
Lobe 3	6	0.08	.480
Lobe 2	5	0.09	.450
Lobe 1	5	0.10	.500

Lobe 1 received the highest depth of cut (0.1mm) and thus is the most abusively ground lobe, whereas lobe 8 is the least abusively ground lobe and conforms with Ford s grinding practice. As reported by Courtney, burn could only be achieved by using a Sterling Abrasives vitrified bond Al_2O_3 wheel at full coolant pressure (as opposed to a plastic bond Al_2O_3 wheel). The grinding parameters are given in Table 2.2:

Table 2.2 Grinding Parameters

Work Material	Induction Hardened, Tempered SAE 52100
Work Speed	60 rpm base circle
Wheel specifications	
• Abrasive grain	Al_2O_3
• Manufacturer	Sterling Abrasives
• Grain Size	60 (medium)
• Bond Type	8 (medium)
Wheel Speed	1958 rpm (80m/s)
Coolant Type	6 percent Castrol 768
Coolant Pressure	120 psi, 35 gallons/minute

2.2 X-ray Residual Stress Profiles of Untested Camshafts

Courtney measured x-ray residual stresses as a function of depth at several locations on a camshaft (labeled as V-8) identical to those used for SVI testing. The results showed significant near-surface tensile residual stresses at the opening ramp. A plot of residual stress to depths of 250 μm at the ramp is shown in Figure 2.1, where increasing lobe number corresponds to decreasing depth of cut (Table 2.1).

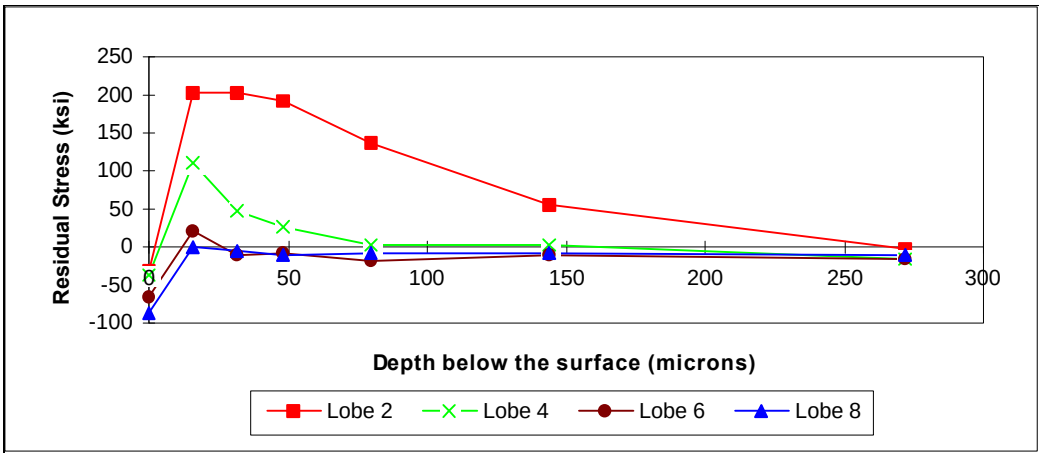

Figure 2.1 X-ray residual stress variation with depth on the opening ramp region of shaft V-8. Lobes 2 and 4 are most abusively ground, as evidenced by large tensile residual stresses (Courtney).

Similar results showed no significant subsurface tensile residual stresses at the nose and at the 90° point between the ramp and base circle. The fact that the largest residual stresses were found at the opening ramp will help explain microscopy results (see Chapter 6) which show cracking to occur only at the opening ramp.

2.3 Accelerated Lifetime Testing (SVI)

Accelerated life testing was performed on the three 2.3L camshafts for an equivalent of 100,000 miles using a standard SVI (Specialized Vehicles Inc.) model laboratory cam fatigue test system. All three camshafts sustained the same grinding history and were tested for service performance in identical conditions.

The accelerated durability test is accomplished by increasing the roller lifter wear by a factor of six for each lobe and applying it to all eight lobes. To achieve the accelerated wear, a hexagonal array of heads is mounted around the camshaft, thus allowing six roller tappets to be run on a given cam lobe. The unit s speed was set to a constant 1200 rpm and run for 336 hours. The springs in the SVI unit were set manually, using a torque wrench, to approximately 116 pounds on the base circle and 263 pounds at the nose (since the same springs were used for all three camshafts, loads were held constant throughout the experiment). Each camshaft was visually monitored for lobe cracking after a determined number of hours (75, 100, 150, 250 or 336 hours). If cracking occurred, the lobe was unloaded and the test continued on the remaining lobes. Table 2.3 provides a summary of the hours to which each lobe was tested.

Table 2.3. Time of testing for each lobe in all three shafts

	Camshaft V-11	Camshaft V-13	Camshaft V-15[¥]
Lobe 1	336 hours	336 hours	-
Lobe 2	100 hours	150 hours	-
Lobe 3	336 hours	150 hours	-
Lobe 4	250 hours	not loaded	-
Lobe 5	75 hours	336 hours	-
Lobe 6	250 hours	336 hours	-
Lobe 7	not loaded	336 hours	-
Lobe 8	336 hours	150 hours	-

2.4 Cam Manufacture

While considering materials and manufacturing processes for engine cams, the design engineer is faced with a variety of limitations and compromises. First, consider the choice of a roller follower over the flat tappet. Even though the roller configuration, among other things, reduces engine noise and decreases surface wear of the cam, the reduced contact area increases contact stresses at the cam-roller interface substantially[6]. Another important design factor to consider is the shift in the choice of raw materials, from gray cast iron to powder metal and forged steel cam lobes. Steels allow maximum permissible compressive stresses far greater than gray cast iron, however, casting remains the most economic processing choice for mass production cam manufacture[7]. Finally, consider the drive for the reduction of cam size and the implementation of a more aggressive displacement profile. The apparent advantages of these steps are the design of a smaller engine, the increase of fuel economy due to a more rapid valve response, and the reduction of valve train vibrations[8]. Nevertheless, the counteracting disadvantage faced is the increase in residual stresses due to grinding. The following list summarizes the main processes involved in the manufacture of the cams:

1. Heat treatments make the material less brittle, without compromising strength or hardness. The following processing sequence for 52100 steel was taken from the Heat Treater s guide[9]:

- forge at temperatures between 925°C and 1150°C,
- normalize by heating to 885°C and air cool,

[¥] Data for camshaft V-15 were not available for analysis

- anneal to form the spheroidized structure desired for both machining and heat treatment, heat to 795°C, then immediately begin cooling to 675°C at a rate not exceeding 6°C per hour,
- Forge the part to its net shape
- Austenitize at 845°C with carbon content near 1.0%; quench in oil, and
- temper the hardened part at 175°C as soon as it has uniformly reached near-ambient temperature (38°C to 50°C), thereby converting the tetragonal martensite to a cubic, tempered martensite (a mixture of ferrite and carbide).

2. Alloy additions are used to obtain surface harnesses in the viscinity of HRC 60.
3. The lobes are induction hardened to a depth of approximately 2.5 millimeters prior to grinding to increase wear resistance.
4. Machining (grinding) is performed to achieve the desire lobe profile. Microfinishing lapping with coated abrasives may take place after fine grinding (the lobes received for this study were not lapped).

2.5 Properties of SAE 52100 Steel

The cam lobes examined were forged from 52100 steel which contains about 1% C and 1.5% Cr (Table 2.4 lists all the alloy additions). This particular steel is used for ball and roller bearings because of its high wear resistance and strength.

Table 2.4. Composition of 52100 steel[10]

ELEMENT	WEIGHT %
Carbon	0.98 - 1.10
Manganese	0.25 - 0.45
Phosphorous	0.025 (max)
Sulfur	0.025 (max)
Silicon	0.15 - 0.3
Cromium	1.3 - 1.6

During abusive grinding of the cam, the steel could be heated to temperatures in the austenitic region. Upon cooling, the bulk of the cam and the coolant quenches the surface rapidly resulting in the formation of martensite. Figure 2.2 shows a portion of the Fe-C phase diagrams emphasizing regions of proeutectoid ferrite and the eutectoid transformation of austenite.

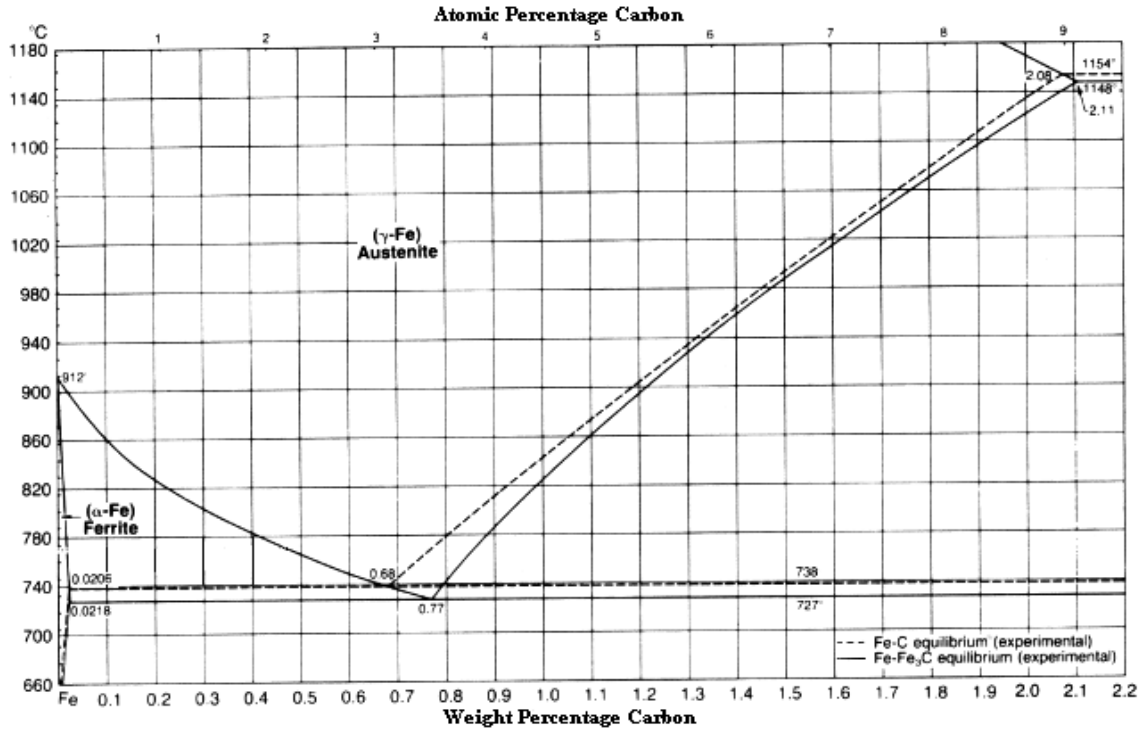

Figure 2.2. Enlarged section of the Fe-C phase diagram[11].

The phase transition temperature for one percent carbon hypereutectoid 52100 steel occurs at 727°C. If the temperature is further increased, transformation to a fully austenitic structure occurs at about 820°C. However, previous cold work or treatments allows austenitic transformation at lower temperatures[12]. Martensite is both hard and brittle, making it susceptible to surface cracking due to the impact or contact loads of the follower. To avoid this, the steel is tempered, thereby reducing brittleness without significantly reducing strength or hardness. Table 2.5 lists the forming temperatures and anticipated hardness of 52100 steel.

Table 2.5. Properties of 52100 Steel[13]

Astenitizing range:	815 to 870 °C
Annealing range:	730 to 790 °C
Martensite start temperature:	250 °C
Maximum forging temperature:	1120 °C
Minimum forging temperature	925 °C
Maximum hardness (water quench)	HRC 66
1 hour temper hardness (300°C)	HRC 57

2.6 Thermal Damage During Grinding

Friction between the abrasive in the grinding wheel and the lobe inevitably produces heat within the grinding zone (about 80 percent of the applied grinding energy goes into the workpiece as heat when using conventional abrasives[14]). This highly localized input of energy induces different thermal effects on the surface of the cam, many times deleterious to the integrity of the workpiece. Therefore, thermal damage can be defined as any grinding-induced thermal phenomena which has an adverse effect on the quality of the material. Among the important phenomena are grinding burn, phase transformations, tempering (or rehardening), unfavorable residual tensile stresses, cracks, and reduced fatigue strength. Following is a brief discussion on the most important forms of thermal damage.

In the realm of camshaft grinding, burn is one of the most common types of thermal damage. Grinding burn is the general term used to categorize metallurgical changes on the surface of the cam induced by sharp thermal gradients due to frictional forces between the wheel and the workpiece. Burn can be exacerbated by many factors including wheel dulling, an increase in depth of cut (higher material removal rate), and ineffective application of coolant. According to microhardness distributions in the subsurface of the ground lobe, burn can be categorized as two types: temper burn and rehardening burn. Temper burn occurs when the lobe s surface softens after grinding. As reported by Malkin[15] , the degree of softening by tempering of hardened martensitic structures is a complex phenomenon which is mainly due to carbon diffusion and is dependent upon both temperature and time. Rehardening burn, on the other hand, is characterized by an abrupt increase in hardness near surface as seen in Figure 2.3. Rehardening is caused by a reaustenitization followed by the formation of untemepred martensite.

Residual stresses are another type of thermal damage. They are defined as the stresses that result from the presence of elastic strains remaining in a component as a result of prior working or treatment[16]. Residual stresses are caused when thermal gradients or mechanical pressures are significant enough that the stresses developed exceed the yield strength of the material[17]. The residual stresses generated due to grinding can be of two types: compressive

and tensile. Being able to identify the type of residual stress present at the surface, or near-surface, of the cam is crucial in the study of the failure mode of the component. Compressive residual stresses generally increase fatigue resistance,[18, 19, 20] whereas tensile residual stresses facilitate crack propagation.[21, 22, 23, 24]

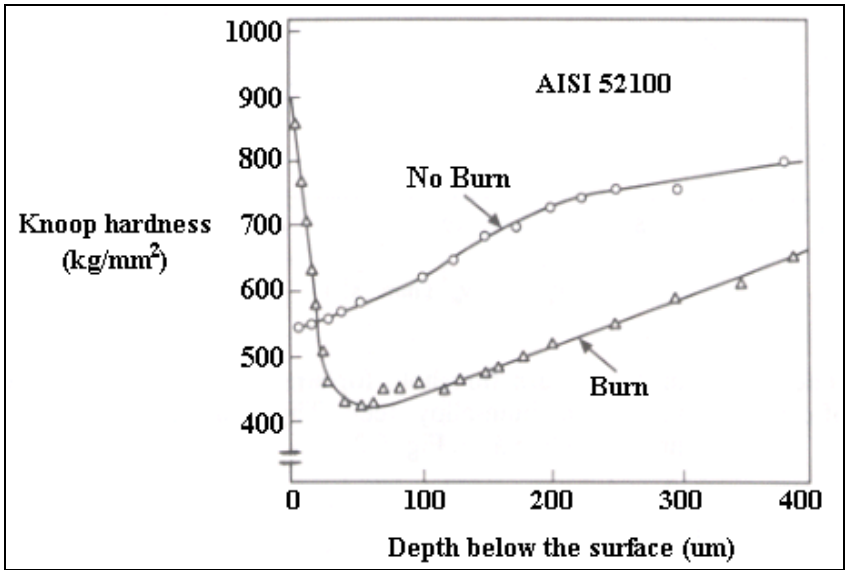

Figure 2.3 Microhardness vs. depth below the surface with and without burning for 52100 steel (Malkin).

As reported by Moller[25], mechanical pressures between the grinding wheel and the surface of the cam create stresses at least an order of magnitude less than thermal stresses. In addition, previous research has also shown that residual stresses during grinding are mostly thermal in origin[26,27]. Formation of compressive stresses at the surface of the cam can be attributed to the plastic deformation under a compressive field between the cam and the wheel, having the effect of lengthening the ground surface with respect to the interior. The hotter material closer to the surface is constrained by cooler subsurface material, inducing thermal compressive stresses at the surface. This localized thermal expansion, when sufficiently big, can lead to grinding cracks at the surface[28] (another type of thermal damage). Tensile residual stresses subsurface can be explained by the laws of mechanical equilibrium, which dictate that regions of residual compression must balanced by regions of residual tension.

Chapter 3

FORCE AND CONTACT STRESS ANALYSIS

Machinery is the new Messiah - Henry Ford

A basic understanding of the requirements involved in cam design is necessary to comprehend the after-effect of SVI testing on the integrity and efficiency of a cam lobe. This analysis will prove to be useful in explaining the increase in wear and spalling in different regions of the lobe. Thus, this section starts with a discussion of the procedure used to determine the lobe s shape, pressure angle and radius of curvature. Next, the contact forces between follower and cam will be determined by considering the cam speed, dynamic forces, linkage dimensions, pressure angle and spring forces. Finally, a Hertzian analysis of the contact stress field between the roller follower and the cam will be presented.

3.1 Determination of the Cam Shape

The shape of the cam was determined by placing the part in a lath and using a dial gage (with a precision of ± 0.0001 in) to measure displacement in 2° increments. These measurements were done by Brian Biggi[29]. Next, the first and second derivatives of the cam s radius with respect to angular displacement were calculated. These expressions are useful because they are found in both the radius of curvature and pressure angle formulas. The radius of the base circle from the center of the cam was measured, and the first derivative $\frac{dr}{d\theta}$ was calculated in 2° increments for every change in radius around the lobe.

Smoothing of the data was achieved by performing a least squares fit of the data (over a range of five points) to a parabola. Point by point, the numerical first and second derivatives were calculated. The cam displacement is determined by measuring the change in radius around the lobe, its velocity is given by $\omega\frac{dr}{d\theta}$ and its lift acceleration is given by $\omega\frac{d^2r}{d\theta^2}$ (ω is the angular velocity). Figure 3.1 shows a plot of the lift, velocity, and acceleration curves for the cam under consideration.

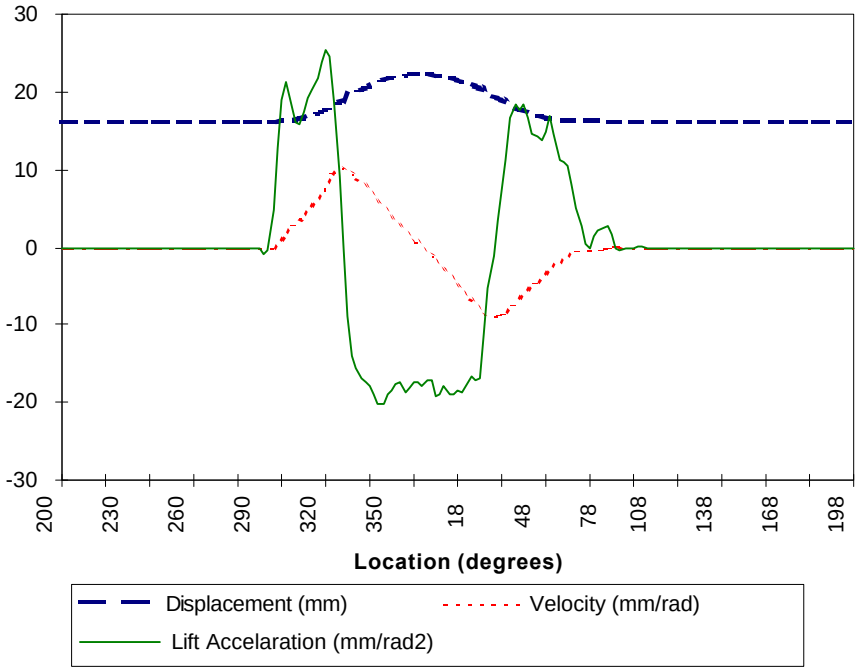

Figure 3.1 Lift, velocity and acceleration profiles for a typical cam at 1200 rpm. The units for the y-axis are shown in the data label.

The radius of curvature, ρ, was calculated using the following standard formula[30]:

$$r = \frac{\left((f(\theta))^2 + (f'(\theta))^2\right)^{2/3}}{(f(\theta))^2 + 2(f'(\theta))^2 - f(\theta)f''(\theta)} \tag{3.1}$$

where: $r = f(\theta)$, $\frac{dr}{d\theta} = f'(\theta)$, $\frac{d^2r}{d\theta^2} = f''(\theta)$

The pressure angle is defined as the angle between the tangent to the path of the follower motion and the line perpendicular to the tangent of the cam profile at the point of

cam-roller contact. It was calculated by taking the dot product of the radial vector from the center of the cam R and the local slope S given by $\frac{dr}{d\theta}$, and then dividing the result by the absolute value of the product between vectors R and S. The calculated pressure angle and radius of curvature (secondary axis) are shown in Figure 3.2 below.

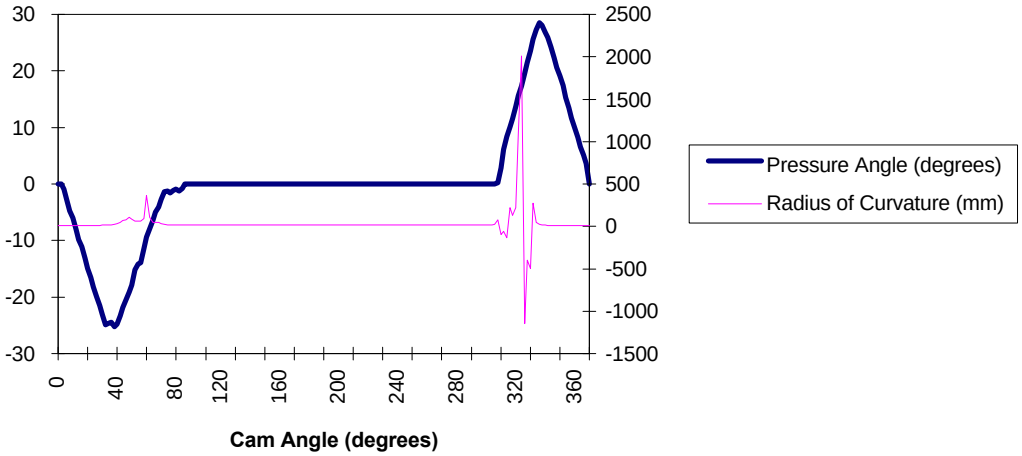

Figure 3.2. Pressure angle and radius of curvature as a function of angular position for the cam. Left scale corresponds to the pressure angle (degrees), and the right scale corresponds to the radius of curvature (mm).

3.2 Force Analysis

The forces acting on the roller follower can now be analyzed. As a first approximation, the forces acting against the direction of motion of the follower can be broken down into three components: spring forces, inertial forces and frictional forces.

The spring force, F_s, on the roller follows Hooke s law of the form[*] :

$$F_S = k(y - y_o) \quad \text{where: k = spring constant = 389.680 lb/in}$$

y = spring compression (in), and

(3.2)

y_o= spring compression at start of lift= 0.341in

The inertial force can be calculated as follows:

$$F_{inertial} = ma = m\frac{d^2r}{dt^2} = m\omega^2\frac{d^2r}{d\theta^2}$$

where: m= mass of rocker arm (lbs_m),

[*] Spring values were taken from input data to a computer model of an engine simulator provided by Ford.

ω = angular speed= 1200 rpm, and (3.3)

$\frac{d^2r}{d\theta^2}$ = second derivative of radius(mm/rad^2).

Finally the normal force between the cam and the roller, F_n, can be calculated from the following equation[31]:

$$F_N = \frac{P}{\cos\alpha - \left(2\mu\frac{l_1}{l_2} + \mu - \mu^2\frac{d}{l_2}\right)\sin\alpha} \tag{3.4}$$

where: P= force acting against the direction of motion of follower ($P= F_{inertial}+ F_{spring}$)

α= pressure angle (degrees)

l_1, l_2, d= Linkage dimensions,

μ= Coefficient of friction.

In this simple analysis, the frictional force is assumed to be negligible compared to inertial and spring forces (and thus, l_1, l_2, d are not needed). In this case equation 3.4 simplifies to:

$$F_N = \frac{F_{inertial} + F_{spring}}{\cos\alpha} \tag{3.5}$$

In order to understand the effect of angular velocity on F_N, force calculations were made at 1200 rpm (SVI testing velocity) and 2400 rpm. The results are given in Figure 3.3. The 0° position is taken at the nose of the cam. Note that the greatest normal force occurs at the nose, which decays rapidly throughout the ramps, and maintains a constant value of 116 lbs at the base circle. Furthermore, Figure 3.3 shows that at a higher angular velocity of the cam, a peak in the loading force is seen which is essentially symmetric in the opening and closing ramps. At low angular velocities, the normal force is not too different from the spring force.

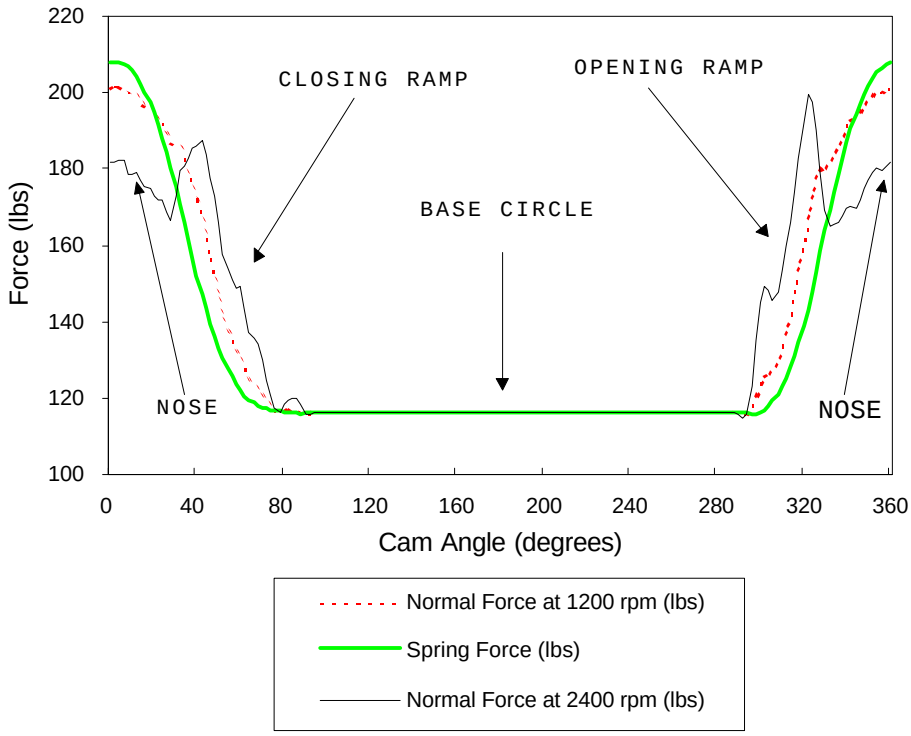

Figure 3.3 Forces acting at the cam-roller interface under different conditions of angular velocity.

3.3 Contact Stress Analysis

The contact stresses studied herein pertain to compressive stresses developed at the contact surface between the roller and the cam due to tangential and normal loads of the valvetrain. An analytical treatment of the fatigue performance of a cam-roller system was developed by Girardin[32]. The following sections summarize his approach in the characterization of the multiaxial stress field between the roller follower and the cam using Hertzian analysis. Results of this study are used, along with the force analysis developed in the previous section, to calculate the contact length and the maximum pressure at the cam-follower interface. These parameters will prove useful in explaining the failure behavior of the cam after engine testing.

3.3.1 Geometric Characteristics

The problem of the cam and the roller follower was simplified by assuming two parallel cylinders in contact. For the cam, different cylinder radii are considered depending on the location (see Figure 3.4(A) and 3.4(B)). This assumption plays an

important role in determining the magnitude of the stresses. If the follower radius is constant, a decrease in radius around the cam will increase the stresses because the same load is distributed on a narrower contact area.

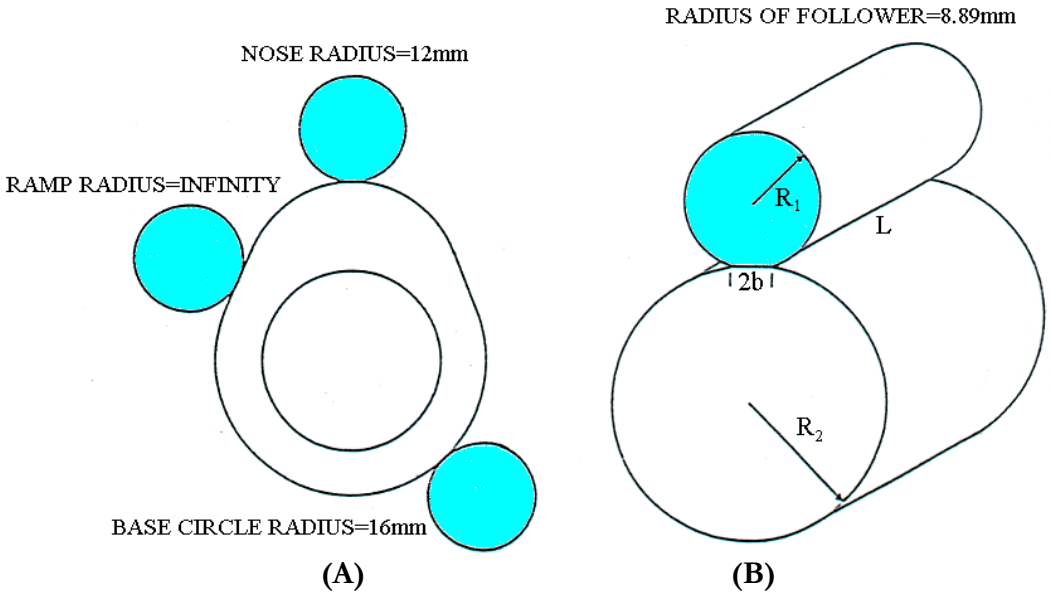

Figure 3.4 (A) Different radii for each region around the cam (the roller follower is represented in blue) (B) Nomenclature used for the Hertzian analysis of two parallel cylinders in contact.

3.3.2 Contact Area and Pressure Distribuition

According to Hertzian theory[33], the shape of the contact surface between the roller and the cam is rectangular of width 2b and length L, and the pressure distribution, p, is characterized by a semi-ellipse (see Figure 3.5).

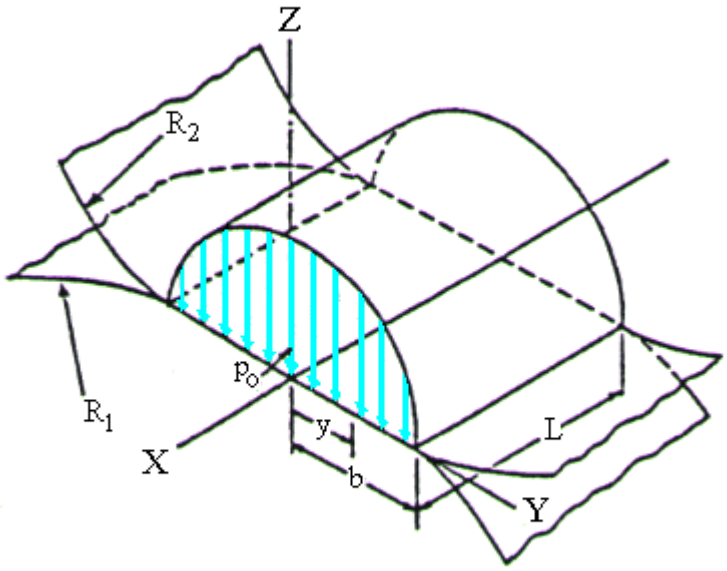

Figure 3.5. Pressure distribution between two parallel cylinders (Juvinall[34])

Implementation of the stress analysis for this case requires the knowledge of the pressure distribution, p, and the maximum pressure p_o. These values can be calculated by knowing the load, the radius of the cylinders, and the materials properties of SAE 52100 steel (such as Young s modulus and Poison s ratio):

$$p = p_o \sqrt{1 - \frac{y^2}{b^2}}\,; \tag{3.6}$$

where the maximum pressure p_o along the load axis (y=0) is given by:

$$p_o = 0.591 \sqrt{\frac{P\left(\frac{1}{R_1} + \frac{1}{R_2}\right)}{L\Delta}} \tag{3.7}$$

R_1 and R_2 are the radius of the follower and the cam respectively. The function Δ is given in terms of the Young s moduli and the Poisson s rations of the two materials:

$$\Delta = \frac{1-n_1^2}{E_1} + \frac{1-n_2^2}{E_2} \tag{3.8}$$

and the contact distance b along the y axis is defined by

$$b = 1.13 \sqrt{\Delta \frac{P}{L\left(\frac{1}{R_1} + \frac{1}{R_2}\right)}} \tag{3.9}$$

The Hertzian method has two limitations which are worth mentioning: the bodies are assumed to have elastic and isotropic material behavior, and the length L of the cylinders has to be very large in comparison with their radii, which is not the case for the cam and the follower configuration.

Using the results developed in section 3.2, the maximum pressure p_0 can be calculated as a function of cam angle using equation 3.7. The load P is taken at 1200 rpm, the radius of the follower is 8.89 mm, the contact length L is calculated by taking the average length of the wear track for all 24 lobes ($L \approx 8 \pm 0.2$mm), and Young s modulus and

Poisson s ratio are 206700N/mm^2 and 0.29 respectively. In a similar manner, the contact length b is calculated using equation 3.9. The results are displayed in Figure 3.6 below.

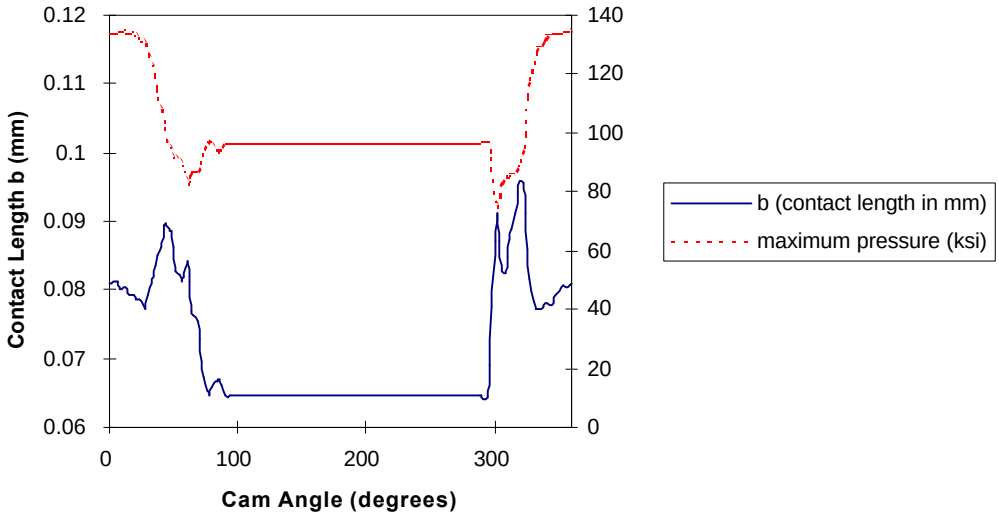

Figure 3.6 Contact length b and maximum pressure p_o (plotted in secondary axis) as a function of cam angle.

The maximum pressure occurs at the nose. This result is expected due to a combination of highest load (Figure 3.3) and smallest radius, therefore increasing the pressure because the same load is distributed on a narrower contact area. The maximum pressure distribution in Figure 3.6 is related to the contact stress by almost half the value[•]. The contact length follows an interesting trend, peaking at the opening ramp (about 320°). The reader is reminded that it is at this location where the radius of curvature goes to infinity (Figure 3.2).

3.3.3 Evaluation of the Contact Stresses

As reported by Smith and Liu[35], failure from contact stresses generally falls into two categories:

- localized deformation by yielding or distortion, and
- fracture by progressive spreading of a crack (fatigue).

Failure due to inelastic deformation is associated with the maximum shear stress defined by the equation:

[•] Ford reported a maximum contact stress value at the nose of 236ksi.

$$\tau_{max}=(\sigma_1 - \sigma_3)/2 \tag{3.10}$$

in which σ_1 and σ_3 are the maximum and minimum values of the principal stresses at the point of maximum shear. The maximum values of stress are necessary for the determination of failure location and life estimation. The objective of this section is to give the reader a synopsis to the results of the stress analysis developed by Girardin. For a more general overview of the effective stresses and the computation of the actual multiaxial stress field, the reader is referred to Girardin s master thesis[36].

The maximum shear stress that the material experiences depends on depth and location around the cam. Differentiating between plane stress and plane strain conditions is important because the maximum shear stress is different in each case. Plane stress is assumed to occur at a point on the material close to the edge. The normal and shear stresses in the axial direction at this location are zero. Plane strain is assumed to occur at a point in the middle of the body in the axial direction (x axis). In this case, the normal and shear strains in the axial direction are neglected.

The normal and shear plane stresses can be calculated adopting the method of Smith and Liu[37] in conjunction with the assumption that no sliding occurs between the cam and the follower (tangential loads are neglected). At the surface, the plane stresses adopt the following values:

$$\begin{aligned} \sigma_y &= -p_o \\ \sigma_z &= -p_o \\ \tau_{yz} &= 0 \end{aligned} \tag{3.11}$$

The subsurface stress field as a function of y, z, p_o and b can be calculated using the following relations:

$$\begin{aligned} \sigma_y &= -\frac{p_o}{\pi} z\left(\frac{b^2+2y^2+2z^2}{b}\Psi - \frac{2\pi}{b} - 3y\gamma\right) \\ \sigma_z &= -\frac{p_o}{\pi} z(b\Psi - y\gamma) \\ \tau_{yz} &= -\frac{p_o}{\pi} z^2\gamma \end{aligned} \tag{3.12}$$

where y and Ψ are a function of y, z, and b, defined by the following equations:

$$y = \frac{p}{K_1} \frac{1 - \sqrt{\frac{K_2}{K_1}}}{\sqrt{\frac{K_2}{K_1}} \sqrt{2\sqrt{\frac{K_2}{K_1}} + \frac{(K_1 + K_2 - 4b^2)}{K_1}}} \tag{3.13}$$

$$\Psi = \frac{p}{K_1} \frac{1 + \sqrt{\frac{K_2}{K_1}}}{\sqrt{\frac{K_2}{K_1}} \sqrt{2\sqrt{\frac{K_2}{K_1}} + \frac{(K_1 + K_2 - 4b^2)}{K_1}}} \tag{3.14}$$

and K_1 and K_2 are given by:

$$\begin{aligned} K_1 &= (b + y)^2 + z^2 \\ K_2 &= (b - y)^2 + z^2 \end{aligned} \tag{3.15}$$

Figure 3.7 shows the normal and shear plane stresses plotted as a function of distance along the y-axis at three depths: Surface, 0.5b below surface, and 1.0b below surface (b is half of the contact length along the y axis as seen in Figure 3.5).

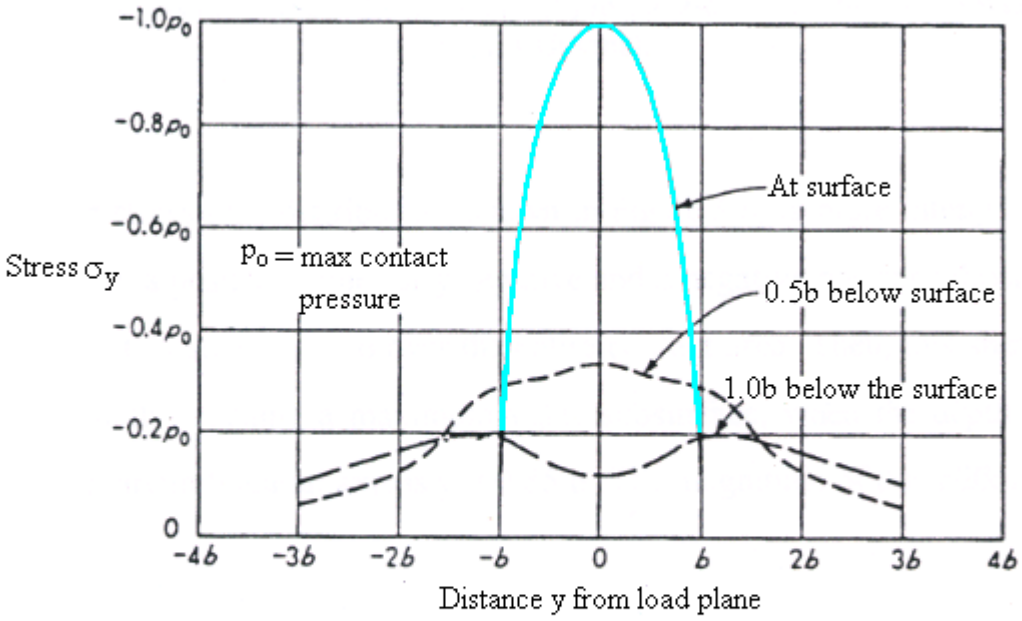

(A)

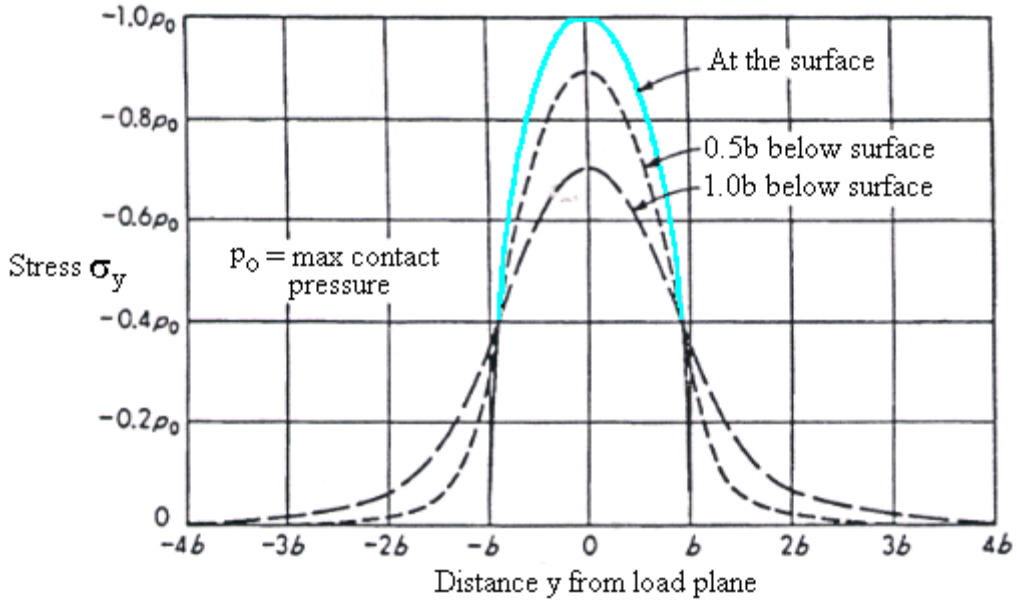

(B)

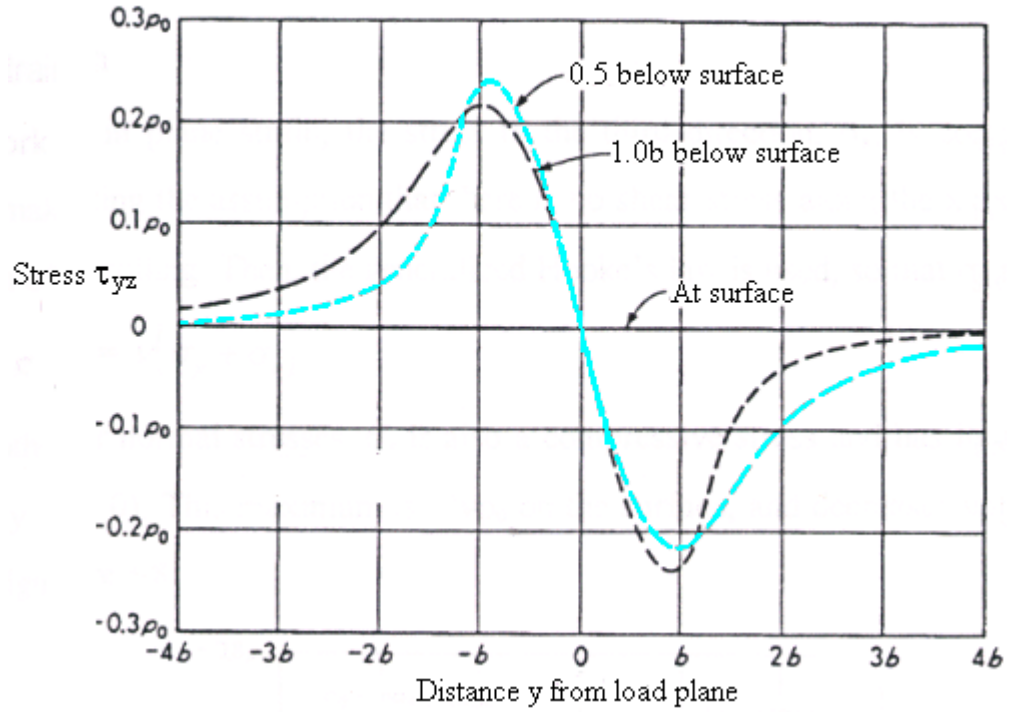

(C)

Figure 3.7 (A) Normal stress in the y-direction (B) Normal stress in the z-direction and (C) Shear stress in the y-z plane. Stresses are given in terms of the maximum Hertzian pressure p_o. Blue line represents the location of the maximum value in stress (Girardin[36]).

Normal stresses σ_y and σ_z are compressive over the entire contact area, with the maximum value of $-p_o$ at the surface. These stresses decrease with increasing depth. The shear stress is zero at the surface. It increases with depth, reaching a maximum value subsurface, at a depth of 0.5b. Therefore, fatigue cracks are expected to form first below the surface.

Results from the force and contact stress analysis presented in this chapter will prove useful in explaining many of the wear and cracking observations on the lobes after engine testing. In addition, the Hertzian analysis identifies the maximum cyclic stress component (occurring subsurface) and is useful for fatigue calculations presented in the next chapter. The following list summarizes the key results found in this chapter:

- the radius of curvature of the cam goes to infinity at the opening ramp (about 320°) as seen in Figure 3.2,
- at 1200 rpm (angular velocity adopted in the SVI engine testing), the normal force at the cam-follower interface is symmetric between the opening and closing ramps,
- the contact length b between the follower and the cam reaches a maximum at the opening ramp (about 320°), and
- the maximum cyclic shear stress occurs subsurface.

Chapter 4

LIFE PREDICTIONS

When man wanted to make a machine that would walk he created the wheel, which does not resemble a leg - Guillaume Apollinaire: Les Mamelles de Tir, sias (1918)

The forces and contact stresses of the cam-follower system were characterized in Chapter 3. This chapter will focus on the fatigue properties of the system as influenced by manufacturing and design parameters. The chapter is divided into two sections: first, an overview of the different failure modes at the interface of a cam/follower system will be discussed. In the second part, a fatigue damage model used to predict fatigue crack initiation will be presented.

4.1 Failure of Cams: Rolling Contact Fatigue

The various modes of contact-fatigue failure between a cam and a follower can be classified according to their appearance and the factor which promote their initiation and propagation. In this section, a general overview of the most common forms of failure for this system will be given.

The main failure modes of the cam-follower configuration are scuffing and pitting[37]. The probability of one of these occurring depends on several parameters such as material properties, lubricants, loads, engine speed, and temperature[38].

Scuffing occurs by a metal-to-metal contact of the surfaces (usually associated with oil breakdown) leading to welding and tearing[39]. This form of failure depends more on contact loads than on time, occurring at high contact loads while pitting occurs at lower loads. The main features of scuffing are[40]:

- significant plastic flow occurs on the worn surface,

- the scuffed surface shows the damage feature in the form of delamination, and
- fatigue striation characteristics can be seen in some places where the delaminated layers have just flaked off.

Pitting on the other hand, is a fatigue process that involves the initiation and propagation of cracks[41]. Surface layers fail as a result of cyclic stresses due to the rolling contact nature of the system, with material flaking off resulting in characteristic pitted surface. This form of failure depends both on stress and running time. The main characteristics of pitting cracks are[42]:

- the majority of cracks initiate on the very surface or from the bottom of micropits, propagating with a certain inclination downwards, and
- a smaller percentage of cracks initiate at a certain depth of sublayer and propagate parallel to the surface. These cracks can abruptly change direction of propagation upwards towards the surface, flaking-off a piece of material and leaving behind a pit.

Rolling contact fatigue cracks can be classified into two groups depending on where they are initiated: cracks may be initiated at the surface and propagate down into the bulk of the cam at a shallow angle to the surface, or cracks may be initiated below the surface, in a region of maximum cyclic shear stress.

Surface cracks can be initiated by the near-surface plastic deformation caused by the contact stress of the follower (Smith and Liu[43] have analyzed the surface and subsurface state of stress with tangential forces on the contact area and concluded that the maximum shear stresses shifts to the surface when sufficient tangential forces are present), by defects such as dents or scratches, or by thermal stresses generated during the manufacturing grinding process. Once they are originated, surface cracks usually propagate at an angle to the surface. After reaching a critical depth or length, these cracks either branch up toward the free surface, so that a piece of material is removed thus leaving behind a pit, or branch down at a steep angle causing catastrophic failure[44]. Miller and Clarke[45], and Miller[46], reported that surface cracks propagating deeply into the material can be arrested or worn out after a certain time.

Propagation of surface cracks is dominated by a fatigue mechanism driven by the contact stress associated with the rolling and sliding of the follower. As mentioned in the last chapter, these contact stress at the cam-follower interface form a compressive field which by intuition will prevent crack propagation. To explain the unusual form of fatigue associated with the propagation of surface cracks, three possible mechanisms have been proposed:

1. the cracks are propagated in a shear mode driven by the cyclic shear stresses caused by repeated rolling contact[47],
2. fluid is forced into the crack by the load, thus prizing apart the faces of the crack[48], or
3. fluid is trapped inside the crack and subsequently pushed towards the crack tip[49].

Subsurface cracks are initiated in regions of maximum shear stress. Subsurface fatigue cracks usually propagate parallel to the surface. When a subsurface cracks propagates upward towards the surface, it forms a pit. Photographs of subsurface cracks and the start of subsurface fatigue at oxide inclusions in 52100 steel have been published by Styri[50].

Nonmetallic inclusions act as stress concentrators and are the main cause for subsurface cracking. Most research done on contact fatigue originated at an inclusion has shown to be accompanied by changes in microstructure in the region of maximum subsurface shear stress[51]. Earlier research has employed fracture mechanics to characterize the driving force for subsurface crack growth[52]. Kaneta[53] analyzed the growth mechanism of a circular subsurface crack due to a Hertzian contact pressure associated with a surface traction. Results from this study shows that the shear mode crack growth rate increases with increasing crack size and traction force.

4.2 Fatigue Analysis: Life Predictions

Fatigue is a cyclic mechanism which leads to failure at a stress level below the ultimate tensile stress. To predict the service life of a cam lobe, a parameter has to be found to represent the combined multiaxial stress state resulting from residual stress and the cyclic stresses. Then, a procedure called the most damaged plane is used in conjunction with a fatigue model to find where failure is likely to occur for a particular stress state. After considering three models (Smith Watson Topper, Socie, and Morrow), Girardin concluded that Morrow s model, which predicts reasonable life estimates, is the best suited for this study. The following section summarizes this fatigue model[54].

4.2.1 Morrow s model

Morrow s model uses the Tresca effective stress which represents the multiaxial state of stress at a point. Because the stresses at the interface of the cam and follower are all compressive, the effective stress is assumed to have a negative value. Knowing the principal stresses, the Tresca effective stress can be computed:

$$\sigma_{effe.Tresca} = Max\left(|\sigma_1 - \sigma_2|, |\sigma_2 - \sigma_3|, |\sigma_3 - \sigma_1|\right) \tag{4.1}$$

In the Morrow model, at each location the stress amplitude, σ_a, and the mean stress, σ_m, are calculated for different depths from the effective stress cycle. These parameters are necessary to find the service life using the following relations[55]:

$$\varepsilon_a = \left(\frac{\sigma'_f - \sigma_m}{E}\right)(2N_f)^b + \varepsilon'_f (2N_f)^c \tag{4.2}$$

where: N_f = fatigue life,

E = Young s modulus, and

c, b, σ'_f , ε'_f = fatigue properties of the material.

The second term of the right hand side, which represent the plastic part of the deformation, is neglected and Hooke s law is used to solve for N_f:

$$N_f = \frac{1}{2}\left(\frac{\sigma_a}{\sigma' - \sigma_m}\right)^{\frac{1}{b}} \tag{4.3}$$

4.2.2 Predicted Service Life

Life predictions are obtained by incorporating the calculated stress states of lobes ground under various conditions (gentle, moderate, severe) into Morrow s model. Fatigue lives can then be correlated with the residual stress induced by different levels of grinding. Girardin calculated the predicted service life for a range of maximum Hertzian pressures p_o between 200 and 300 ksi for the opening ramp (as seen in Figure 4.1). This range is based on Ford design experience where a typical p_o is around 230 ksi on the cam lobe. He used the residual stress states generated by abusive grinding as measured by Courtney and shown in Figure 2.1.

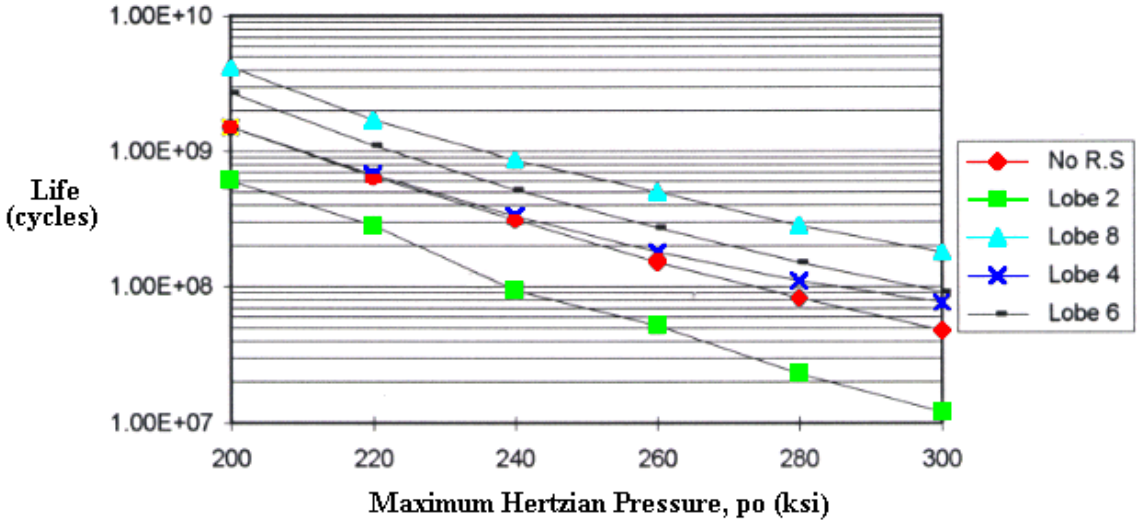

Figure 4.1. Life predictions on the ramp vs. Hertzian pressure for different levels of grinding (Giradin).

The shortest lives are found in the most abusively ground lobe (lobe 2) . The predicted service lives for lobe 8 and lobe 6 are considerably longer than lobe 2. Note that these lives are even longer than the case of no residual stress. This suggests that mild grinding of a cam tends to create subsurface compressive residual stress fields which extend the lifetime presumably by closing the cracks that try to open and propagate. Compressive subsurface residual stresses are a positive factor on service life. The correlation of service life as a function of maximum Hertzian pressure and residual stress is best analyzed by plotting these parameters in a 3-D graph seen in Figure 4.2 below.

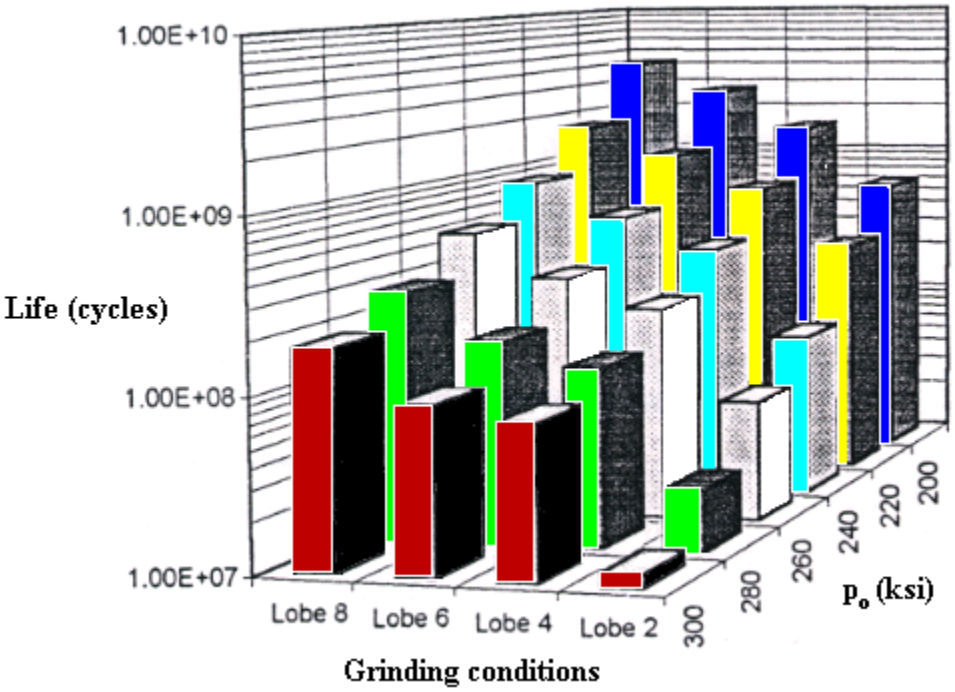

Figure 4.2. Life prediction as a function of lobe number (residual stress) and Hertzian pressure for the opening ramp (Girardin).

If the Hertzian pressure is increased by 100 ksi (from 200 ksi to 300 ksi), the predicted life is reduced by a factor of twenty. The life also follows this tendency when the grinding is more abusive. The more abusive the grinding, the shorter the predicted life at a constant Hertzian pressure as represented by each set of color bars. Lobe 2 (with the highest residual stress for that set) at a pressure of 300 ksi represents the worst case with the shortest life (brown bars). Lobe 8, which conforms with Ford s manufacturing grinding protocol, exhibits a predicted fatigue life about 15 times longer than that for lobe 2 at all Hertzian pressures. Once again, the life for gently ground lobes is increased through creation of a compressive subsurface residual stress field which prevents crack growth.

The predicted failure location is calculated by determining the critical plane where the stress amplitude is the largest. The maximum stress range is an important parameter to evaluate the degree of fatigue damage. Table 4.1 lists the predicted failure locations below the surface for a range of Hertzian pressures.

Table 4.1. Failure locations as a function of pressure and residual stress.

	Range of maximum Hertzian pressure (ksi)					
	200	220	240	260	280	300
LOBE 2	125μm	125μm	150μm	150μm	175μm	200μm
LOBE 4	150μm	175μm	175μm	175μm	175μm	200μm
LOBE 6	150μm	150μm	175μm	200μm	200μm	200μm
LOBE 8	150μm	150μm	150μm	175μm	175μm	200μm

The location of failure is subsurface, as predicted by Hertzian analysis. Note that these depths are 3 to 5 times greater than the depths of the peak residual stress (Figure 2.1) as found by Courtney. Abusively ground lobes tend to fail closer to the surface, due to tensile subsurface residual stresses; this is particular true for smaller pressures when the residual stress fields play an increasingly important role. This results imply that grinding and/or operation conditions which drive tensile residual stress deep below the surface should have a more deleterious effect than those stresses near the surface. Allison[56] has found that such stresses may be generated by grinding with CBN under certain conditions.

The forces and contact stresses generated by the contact between the cam and the follower were characterized in Chapter 3. These results, in addition to the predicted lifetimes found in this chapter will be used to determine the relationship between the camshaft state of stress and the camshaft lifetime. In the next chapter, experimental results from the fatigue tests of the three SVI-tested camshafts prepared under varying grinding protocols will be presented. These results will serve as a link needed to determine the dependency of the camshaft s lifetime on the residual stress distribution.

Chapter 5

EXPERIMENTAL PROCEDURE

It is much easier to make measurements than to know exactly what are you measuring
- J.W.N Sullivan: in R.L. Webster, More Random Walks in Science (1982)

In Chapter 3, an analysis was undertaken of both the forces and the contact stresses developed at the cam-follower interface. A fatigue life model used to estimate lifetimes for the cam-follower system as a function of grinding conditions was presented in Chapter 4. In this chapter, the three SVI-tested camshafts will be fully characterized using nondestructive and destructive evaluation techniques. Results will be used to understand the relationship between the camshaft state of stress (Chapter 3) and the camshaft lifetime (Chapter 4).

5.1 Experimental Matrix

As shown in Figure 1.6, several nondestructive and destructive techniques were used to evaluate the three SVI camshafts (see sections 2.1 and 2.3 for details on grinding protocol and engine testing conditions). It was critical to carefully plan an experimental strategy that will allow to extract as much information as possible from each lobe. The experimental matrix described herein was set up following the completion of the NDE phase, after the wear in each lobe was fully characterized. Each lobe was then selected for a specific experimental technique after careful analysis (due to the destructive nature of many experiments). In that sense, the triplicate camshaft runs allowed us to accommodate several experimental configurations. From the 24 lobes examined, only two were not loaded and left in the as-ground state (see Table 2.3). One was designated for X-ray residual stress analysis (evidence of stress relaxation) and the other was left for microhardness measurements (evidence of cycle softening). The choice of lobes for fractography studies was based on crack nature and size (see section 5.3.1.1). The remaining lobes were set up in an experimental configuration that allowed us to extract as much information as possible

without compromising the accuracy of the data. A summary of the experimental procedure in the form of a matrix can be found in appendix A.

The matrix is subdivided into eight columns (representing the eight lobes of each camshaft) and 6 rows. Each row describes the lobe s characteristics and evaluation techniques (nondestructive and destructive). The first row shows the number of cracks found on each lobe along with the lobe s SVI testing time in parentheses. The second row quantifies the degree of wear of each lobe. The depth of the groove caused by the follower on the surface of the cam is listed in the third row (note that grooves were only found on camshaft V-15). In order successfully examine fracture surfaces, lobes with the greatest degree of cracking were chosen (see section 5.3.1). Few lobes are suited for this purpose and they are selected by a check mark under crack mechanics. Finally, lobes were strategically selected for residual stress and hardness measurements to obtain data for different levels of abusive grinding.

5.2 Nondestructive Evaluation (NDE)

The objective of nondestructive inspection was to identify wear characteristics in each camshaft and determine whether the lobes cracked after being tested in an engine environment for 100,000 miles. The criteria for the selection of a suitable NDE method include the following: crack detection and evaluation, structure or microstructure characterization, and determination of the size and orientation of the cracks. Optical and electron microscopy, acoustic microscopy, and profilometry proved to be efficient techniques to meet these criteria. Figure 5.1 shows the first two stages of the project.

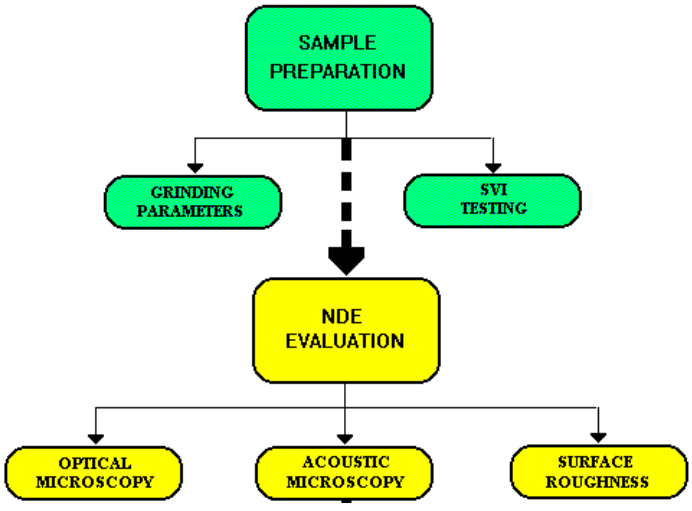

Figure 5.1 Flowchart showing the nondestructive evaluation techniques employed.

5.2.1 Optical Microscopy

The three camshafts were inspected using a Wild M3Z optical microscope with a Intralux 6000 light source. Prior to photographing, each camshaft was visually inspected for areas of extreme wear. In order to find a semiquantitative method to quantify wear, the lobe was divided into equidistant zones around its circumference. Figure 5.2 shows the contour of the lobe subdivided into eleven zones (each zone is aproximately 1cm in length):

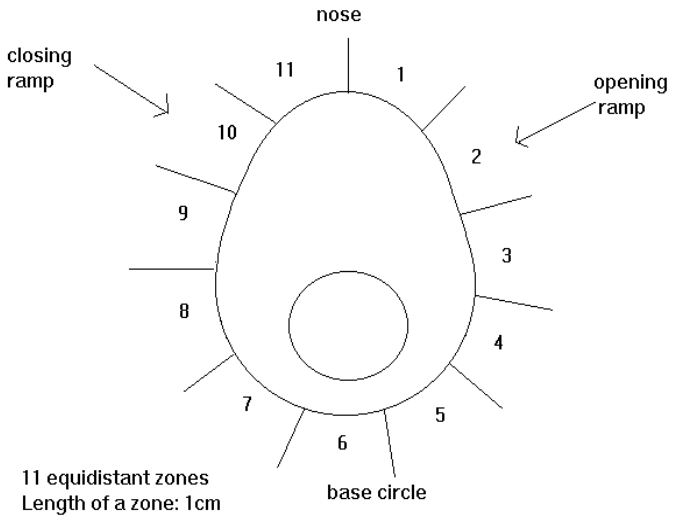

Figure 5.2 Characteristic lobe divided into 11 equidistant zones

The number of discontinuities (cracks, pits, scratches) within a zone were visually counted. Although this method is somewhat inexact, its consistency makes it a practical tool to visualize the relative degree of wear between the lobes. Every discontinuity, regardless of its nature or size, was given an arbitrary number to indicate the degree of wear present. They were labeled as dents to depict any impression or irregularity caused by the roller s friction against the lobe s surface.

Histograms showing degree of wear (scratches, dents, cracks) versus location around the lobe were generated for each lobe in all three camshafts (total of 24 histograms). Figure 5.3 shows a typical set of histograms for camshaft V-11 (full data for all 24 lobes are given in Appendix B).

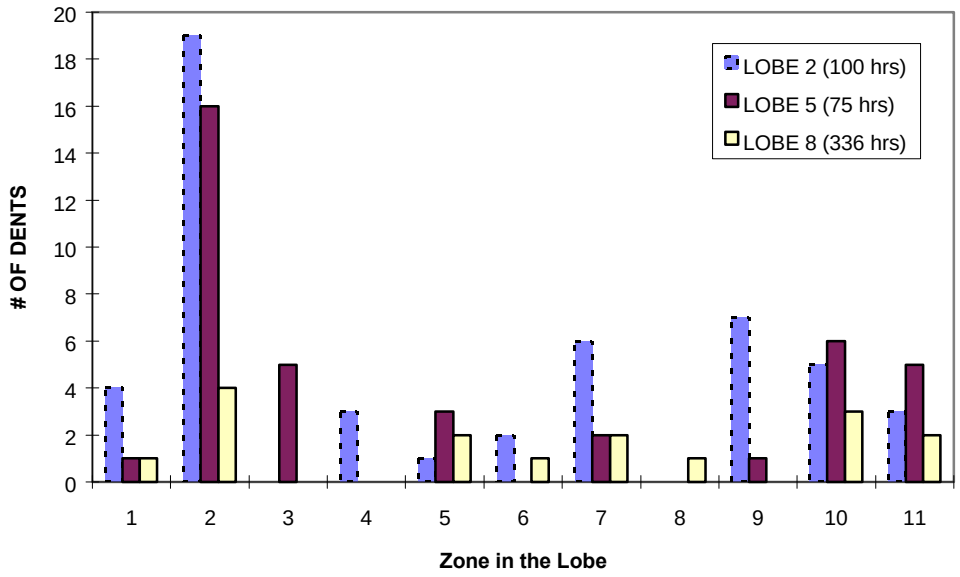

Figure 5.3 Wear conditions vs. zone in camshaft V-11. Note that the testing time for each lobe differed.

Notice that zone 2, which represents the opening ramp (onset of nose region), has the highest degree of wear within a lobe. Moreover, the wear in lobe 2 (most abusively ground) and lobe 8 (least abusively ground) differ considerably.

Inspection of all three camshafts showed cracking to occur predominantly in the opening ramps. A change in coloration of the steel s surface induced by the friction of the follower against the cam s surface was visible around the wear track of the most abusively ground lobes. The width of the wear track remained constant except for the onset of the nose region (see Figure 5.4(A)). Another interesting wear feature was found in almost every lobe in camshaft V-15. Throughout the nose region, the steel appeared to have softened to a point of smearing, causing a drastic change in wear track texture (see Figure 5.4(B)).

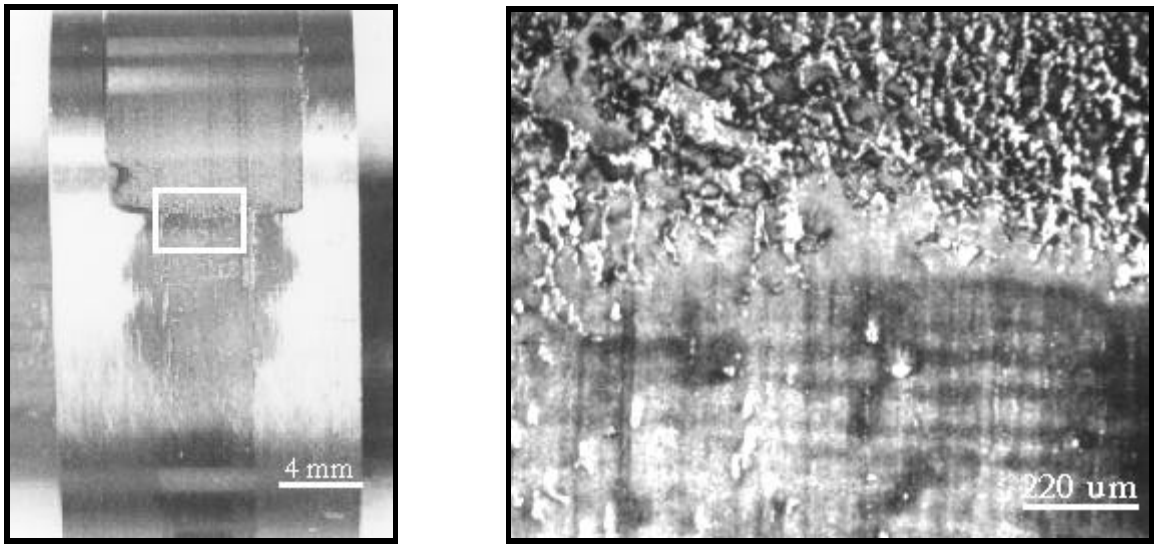

(A) **(B)**

Figure 5.4. (A) A profile of an abusively ground lobe in camshaft V-15 showing a characteristic wear track. Notice the drastic change in features of the wear track as it approaches the nose (~320° in Figure 5.5). (B) Magnified picture of the area marked by the white square in Figure 5.4(A), showing a pronounced change in wear track texture seen in the nose region of abusively ground lobes of camshaft V-15.

Two kinds of surface discontinuities were seen under the optical microscope: cracks and pits. Pitting was caused by material flaking off to depths of no more than 100 μm (see Figure 5.5(A)). Pits were found only within the wear track, and the degree of pitting was the greatest at the opening and closing ramps. Likewise, cracking occurred mostly at the opening ramp (with exception of one crack found on the closing ramp in camshaft V-13). Cracks propagated perpendicular to the direction of rotation as seen in Figure 5.5(B), where the crack is circled.

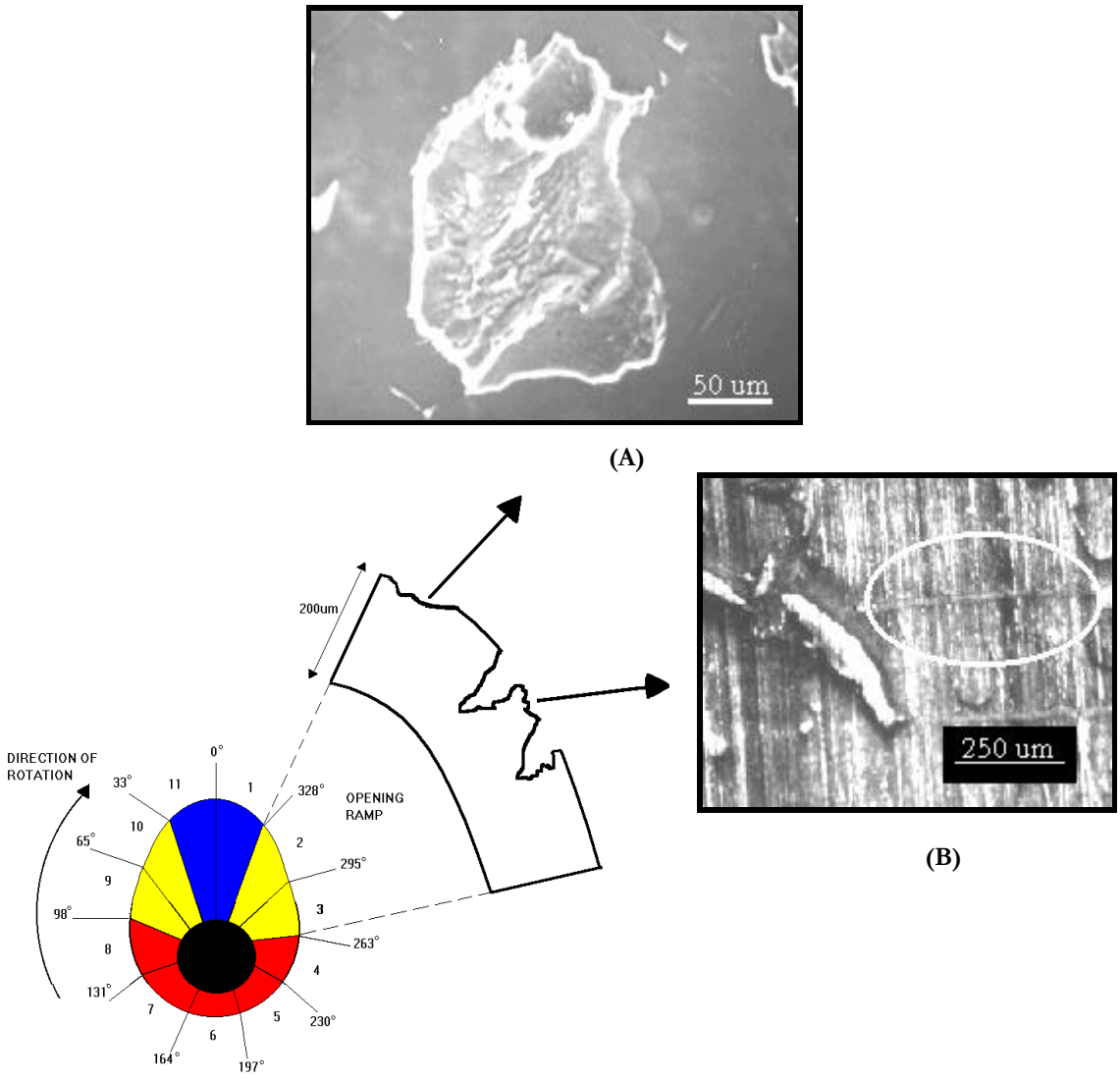

Figure 5.5 Profile of a lobe subdivided into 11 zones of equal length. The blue area represents the nose, yellow areas the ramps, and the red area the base circle. Zone 2 at 328° is where most of the cracking occurred. **(A)** SEM micrograph of a shallow pit. **(B)** Micrograph of pitting formed in the opening ramp. Notice the horizontal cracks which propagate to the right from each pit. These cracks are perpendicular to the direction of rotation of the cam lobe.

Photographs were taken of two distinct types of cracks: pitted and straight. The cracks differed in the way they propagated across the lobe. Straight cracks (Figure 5.6(A)) were about twice as long as pitted cracks (see Figure 5.7 for typical crack lengths), sometimes extending outside the wear path of the roller. Pitted cracks, on the other hand, were concentrated in areas of extreme wear damage as depicted in Figure 5.6(B).

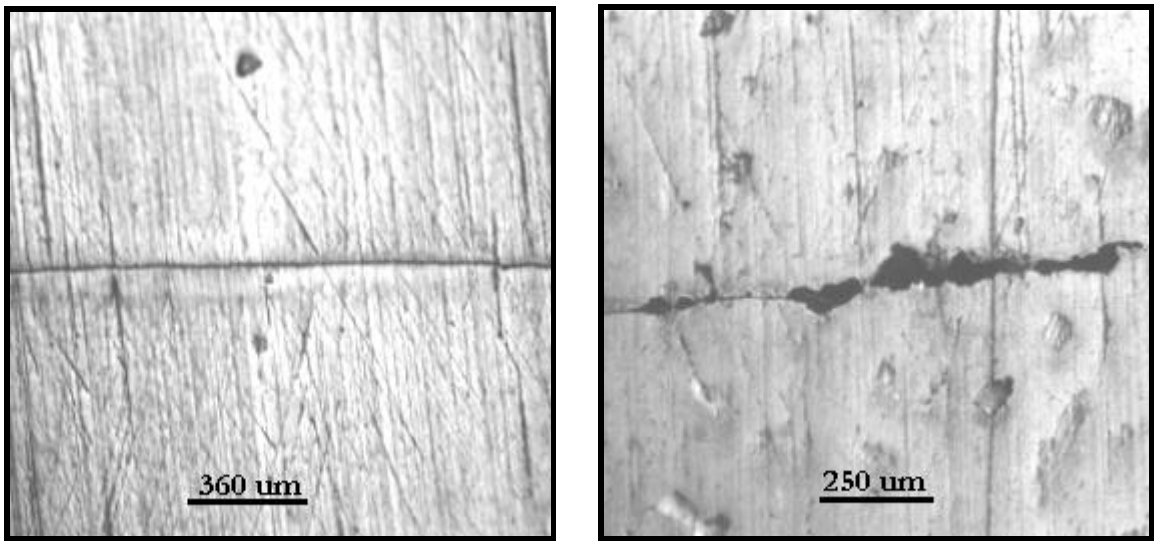

(A) **(B)**

Figure 5.6 (A) Straight crack found in the opening ramp of lobe 3, camshaft V-13. (B) Pitted crack found on the opening ramp of lobe 4, camshaft V-11.

The length of each crack was measured to the nearest tenth of a millimeter as displayed in Figure 5.7. All lengths listed are of cracks found in the opening ramp (zone 2 of figure 6.3) unless otherwise specified.

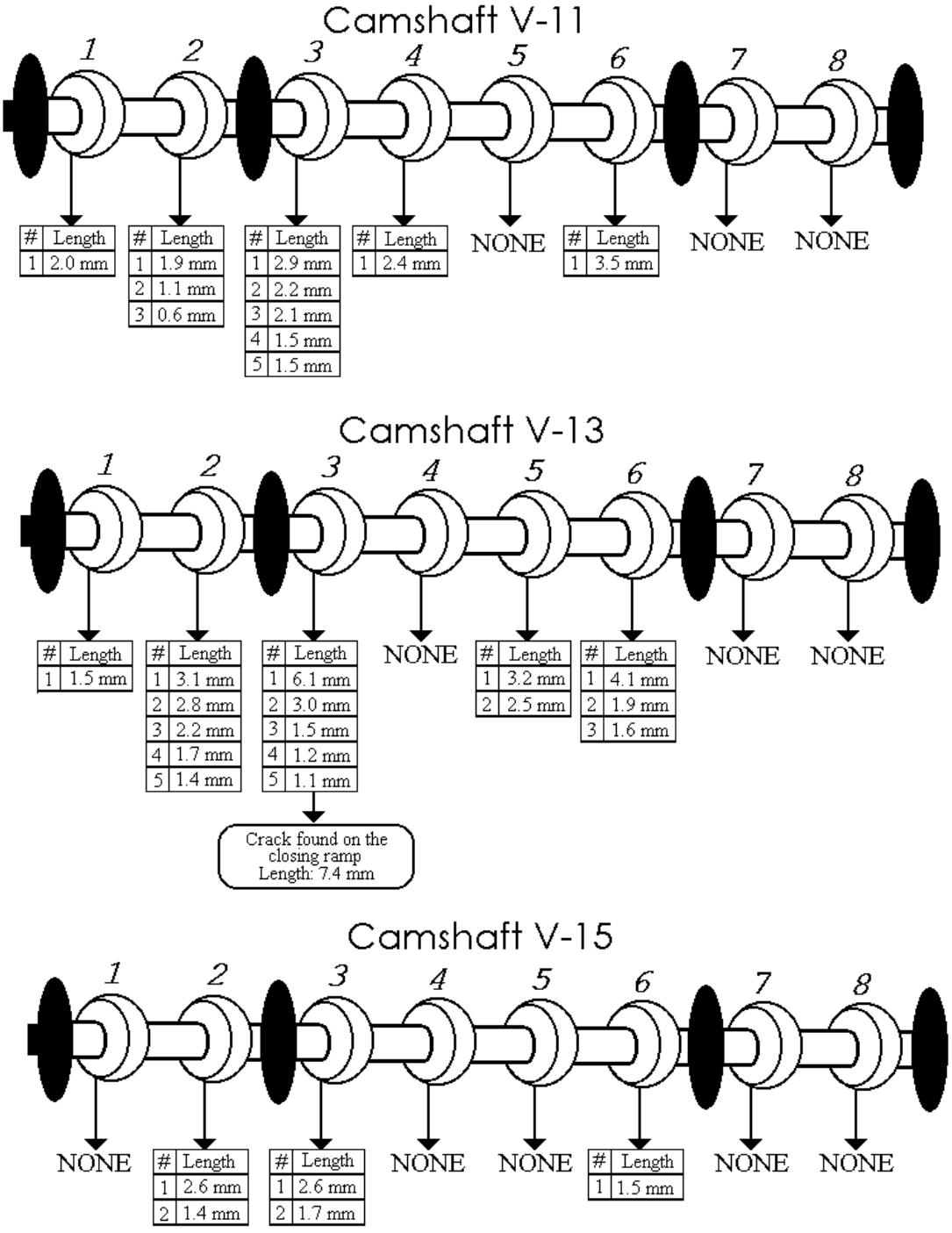

Figure 5.7. Crack lengths were measured to ± 0.1 mm. All cracks occurred in zone 2, onset of nose region (see figure 5.5 for degree location of zone 2). Lobes labeled none indicate that either the lobe exhibited no cracks, or it was not loaded (refer to Table 2.3 for loading conditions).

5.2.2 Grinding Cracks

Two untested camshafts prepared by Courtney with the same grinding protocol as the three SVI-tested camshafts were examined under the optical microscope. Grinding cracks were found on the opening ramp of the most abusively ground lobes (lobes 2 and 3), at the same locations where straight cracks were found after testing (cracks are circled in Figure 5.8).

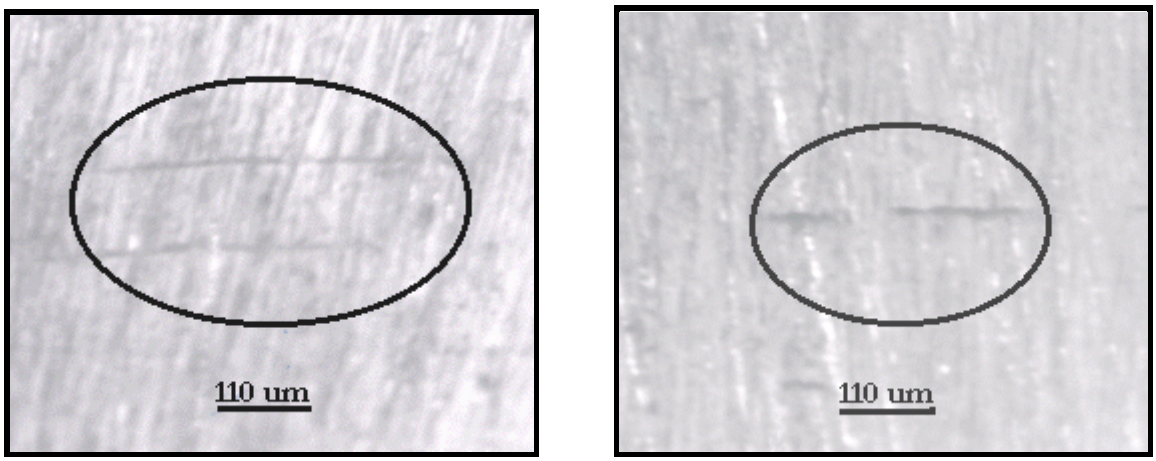

Figure 5.8. (A) Grinding cracks found on the opening ramp of lobe 2 camshaft labeled V-3 (B) Grinding cracks found on the opening ramp of lobe 2, camshaft labeled V-1

These cracks are much smaller but coincide with the same locations and in the same numbers as the cracks in the SVI-tested lobes. Almost no grinding cracks were found on lobe 1 (the most abusively ground), most of the cracks were found in lobes 2 and 3, and no grinding cracks were found on the moderate and mildly ground lobes (lobes 4-8). The grinding cracks seen in Figure 5.8 resemble straight cracks shown in Figure 5.6(A). The effect of SVI testing thus appears to not be a process of crack nucleation, but in fact a process of crack propagation throughout the cyclic loads generated by the roller follower.

5.2.3 Scanning Acoustic Microscopy (SAM)

SAM uses acoustic waves (called Raleigh waves) generated from an acoustic transducer to detect cracks[56]. Raleigh waves are especially sensitive to features such as cracks, grain boundaries, voids, and interfaces between phases[57]. By varying the focal length of the transducer (defocusing), subsurface cracks can be detected. When the microscope is used in focus there is no true Raleigh wave excitation on the surface of the specimen. As a result a crack will simply scatter the directly reflected ultrasound from the surface. By defocusing the lens, a crack at the surface will scatter and reflect the Rayleigh waves[58]. The reflected waves will interfere with the incident Raleigh waves to produce interference fringes surrounding the crack[59] as depicted in Figure 5.9.

Figure 5.9 Schematic diagram of acoustic lens. The transducer generates Rayleigh waves that interact with a surface crack, producing a characteristic fringe pattern.

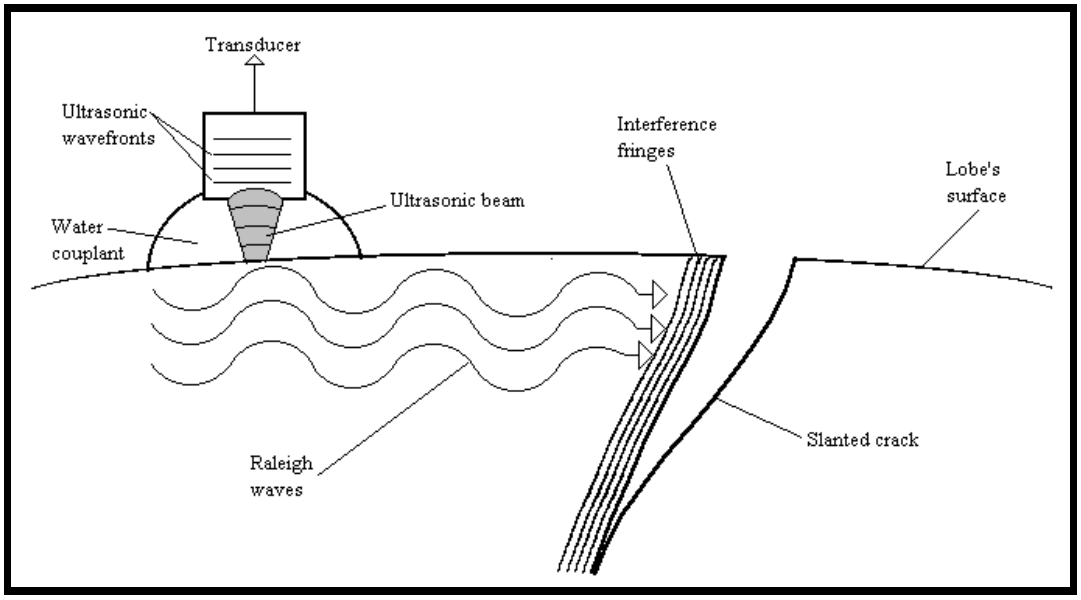

The compressive stresses developed at the cam/follower interface might be expected to cause subsurface tensile stresses parallel to the surface (see the contact stress analysis presented in section 3.3.4). A combination of subsurface stresses and residual tensile stresses due to grinding then might be expected to produce subsurface cracking parallel to the surface.

In order to test this expectation, the most abusively ground lobes of each camshaft (lobes 1, 2, and 3), where subsurface cracking is more likely to occur, were examined under the acoustic microscope. A subsurface crack, parallel to the surface will reflect the acoustic waves, thereby producing an interference pattern as the lens is defocused down into the material in increments of 25um. Table 5.1 summarizes the experimental layout.

Table 5.1. Lobes examined under the Scanning Acoustic Microscope (SAM).

Camshaft ID	Lobe #	Regions examined	Depth (μm)
V-11	**1**	**opening ramp**	**25, 50, 75, 100, 150**
V-11	**2**	**closing ramp**	**25, 50, 75, 100, 150**
V-11	**3**	**nose, base circle**	**50, 100**
V-13	**1**	**closing ramp**	**50, 100, 150, 200**
V-13	**2**	**opening ramp**	**25, 50, 75, 100**
V-13	**3**	**base circle**	**50, 100**
V-15	**1**	**nose, base circle**	**25, 50, 75, 100, 175**
V-15	**2**	**ramps**	**25, 50, 75, 100**
V-15	**3**	**opening ramp**	**25, 50**

In addition to examining lobes for subsurface cracking, SAM could also provide useful information on the direction of crack propagation, i.e. cracks either propagated perpendicular or at an angle to the surface of the lobe. Thus, surface cracks found on the opening ramp of lobe 6 in camshaft V-11 were examined to a depth of 175μm.

The lobes examined by SAM in the opening ramp for evidence of subsurface cracking yielded inconclusive results. Any subsurface void or crack should create a distinctive interference pattern. None was found in SAM analysis. This result, however, should not rule out the existence of subsurface cracking due to its shallow nature. A crack examined under the acoustic microscope yielded results seen in Figure 5.10 (Similar results were seen in lobes 3 of both camshafts V-13 and V-11).

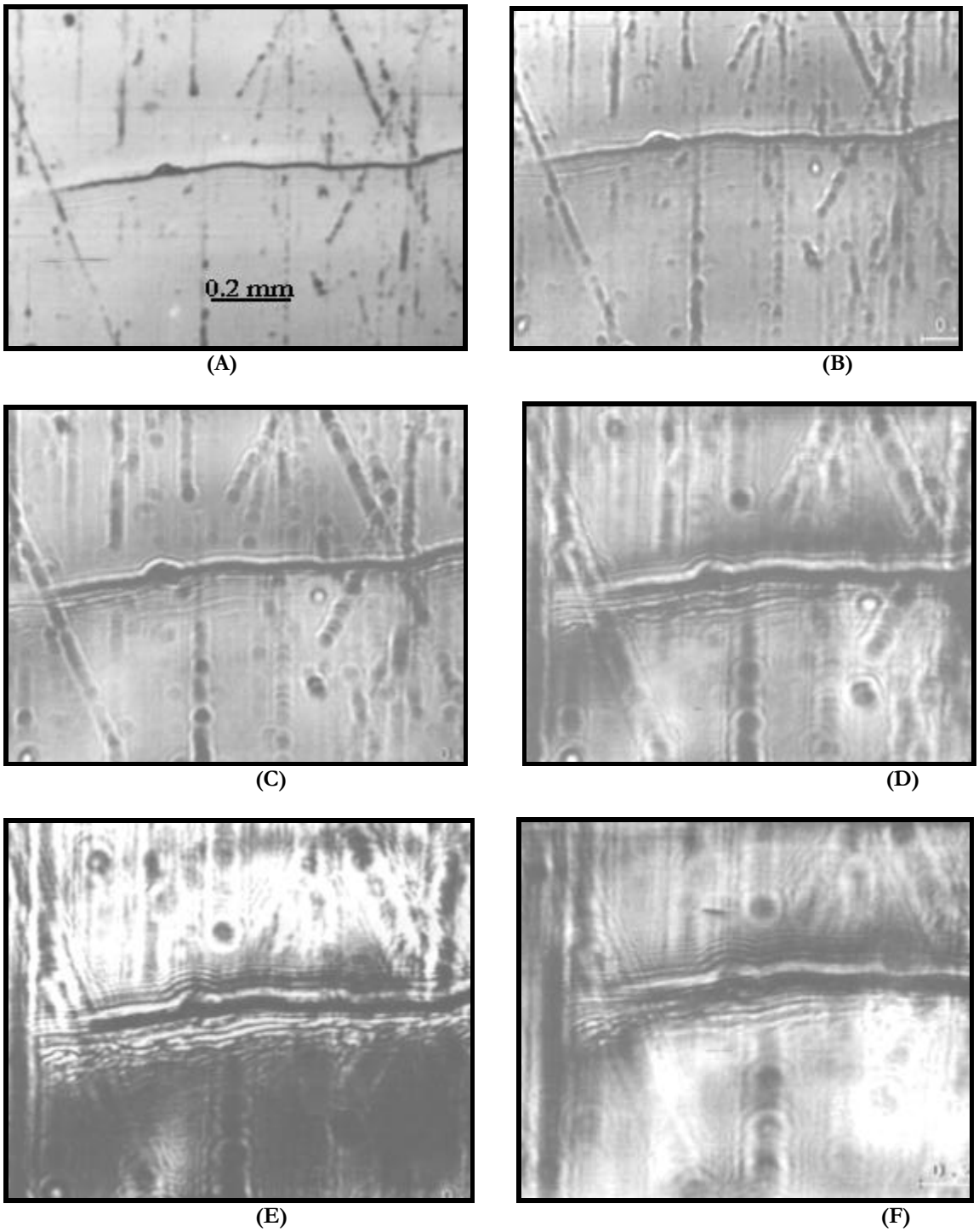

Figure 5.10 . Acoustic micrographs of a crack in lobe #6, camshaft V-11 (at a frequency of 200 MHz) under the following imaging conditions: **(A)** lens focused at the surface; **(B)** lens defocused 25 μm; **(C)** lens defocused 50μm; **(D)** lens defocused 100 μm; **(E)** lens defocused 125 μm; lens defocused 175 μm.

Note that as the lens is defocused deeper into the material, the Rayleigh wave contrast around the crack and the background contrast from grinding damage increased. It was found that interference fringes produced by the Raleigh waves occurred only on one side of the crack, suggesting that the crack is tilted rather than perpendicular to the surface of the lobe, as depicted in Figure 5.9. Previous research by Yamamoto[60] also indicate that surface cracks usually propagate inclined about 20 to 30 degrees from the rolling contact surface, opposite the direction of rolling.

5.2.4 Profilometry

Profilometry is a technique used to determine surface roughness. Roughness is defined as a measure of the topographic relief of a surface, which includes polishing and machining marks, grains, undulations, or marks left by the follower roller on the cam s surface. Evidence of a change in roughness along the wear track of the follower could provide useful information about the effect of residual stresses on the expected lifetime of each cam lobe.

Roughness measurements were done at Landis using a mechanical-stylus profilometer (with a diamond stylus probe that touches the surface). Height variations are measured as the stylus is moved across the length of the lobe s surface. The mechanical stylus movements are displayed on a chart record with the height exaggerated relative to the distance along the surface (see Figure 5.11).

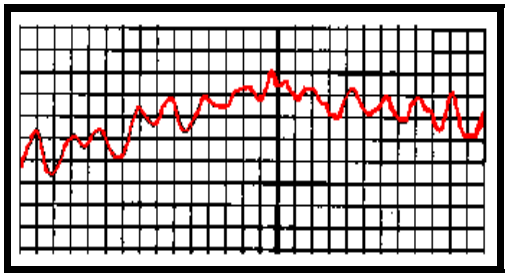

Figure 5.11 Typical roughness profile. Vertical scale = 20 μin, horizontal scale = .02 μin.

Surface roughness was measured at four points (base circle, opening ramp, closing ramp and nose) on every lobe of the three Kulhanek camshafts (total of 96 readings). Figure 5.12 shows a set of surface roughness data taken on an abusively ground lobe in camshaft V-13. These data show no evidence of a groove being formed due to the sliding or rolling friction of the cam follower. Figure 6.8(a) shows a crack about 180 μin deep located in the opening ramp[†]. In addition, slanted profiles indicate that the cam lobe was not ground exactly parallel to the shaft axis (Figure 6.8d).

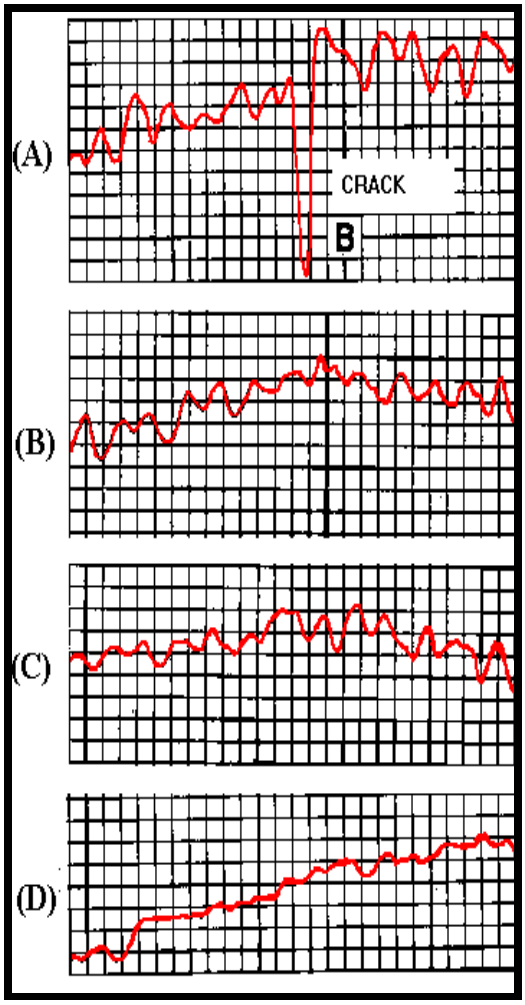

Figure 5.12 Surface roughness measurements on lobe 2, camshaft V-13 **(a)** opening ramp; **(b)** closing ramp **(c)** base circle; **(d)** nose. Vertical Division = 20μin. Horizontal division = 0.02μin.

In addition to roughness profiles, a surface statistical parameter called root mean square roughness (abbreviated R_{rms}) was automatically calculated and plotted by the instrument. This parameter is calculated by taking the average of the square of the absolute values of the surface height variations measured from a mean surface level (this quantity is automatically calculated by the test instrument).

[†] This observation was confirmed by optical and acoustic microscopy.

In an effort to correlate roughness with residual stress due to grinding, the area under the R_{rms} profile across the follower wear path for opening ramps in every lobe was determined as a function of lobe number. Figure 5.13 shows this relationship. This parameter gives a semi-quantitative estimate of the overall roughness of the cam lobe in the opening ramp. It is seen that there is only a slight variation in surface roughness with the level of abusive grinding. Recall that lobe 1 is the most abusively ground and lobe 8 is the least.

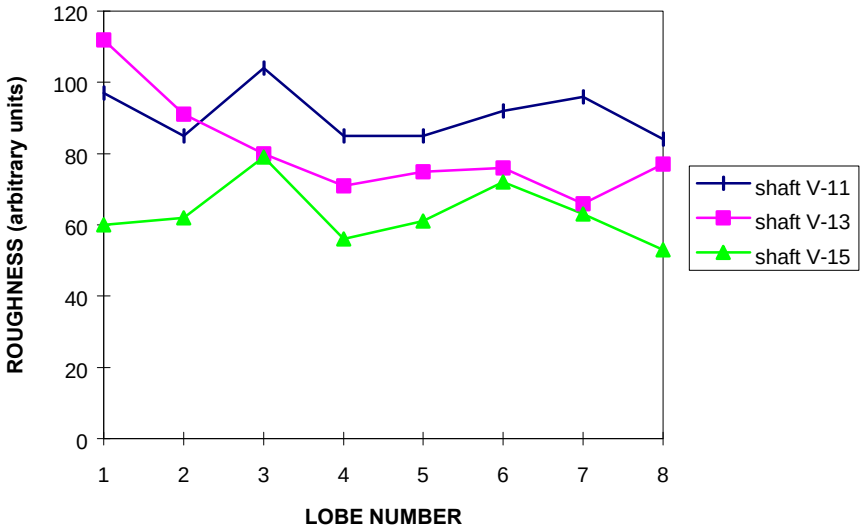

Figure 5.13 Estimated surface roughness in the opening ramp vs. lobe number

As noted previously, the nose region of the lobes in camshaft V-15 appeared to have softened due to a microstructural change in the steel (see Figure 5.4(B)). Profilometry results confirm this fact. Grooves as deep as 600 μin were found across the nose region in the most abusively ground lobes as seen in Figure 5.14 (each vertical division =100μin). Nevertheless, the is no direct correlation of groove depth with induced residual stress due to grinding.

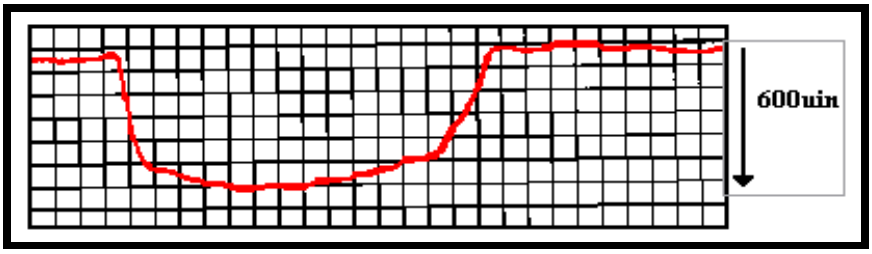

Figure 5.14 Groove produced by the wearing friction of the roller on lobe 6 camshaft V-15. Note that material was displaced toward the boundaries of the wear track forming ridges.

5.3. Destructive Evaluation

Several destructive techniques were used to characterize the failure life of the SVI-tested camshaft lobes. The criteria for the selection of suitable evaluation methods was based on two major requirements: ability to characterize the thermal effects due to grinding and ability to understand the mechanical effect of testing on the service life of the component. The experimental procedure was divided into four main destructive evaluation techniques (see Figure 5.15): fracture mechanics, x-ray residual stress, metallography, and hardness measurements. Each experiment was run according to specifications predetermined by the experimental matrix found in Appendix A.

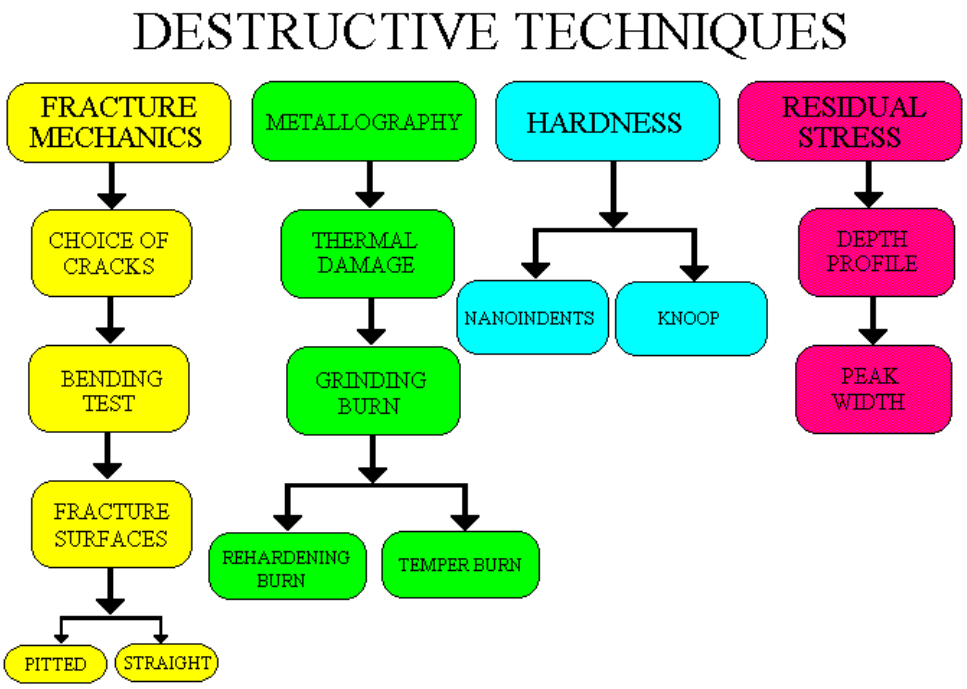

Figure 5.15 Diagram of the different destructive techniques employed.

5.3.1 Fractography

The lobes that received the most abusive levels of grinding showed cracking to occur almost exclusively in the opening ramp region. The objective of the fracture mechanics study presented is to examine these cracks in detail. The lobes were sectioned across the opening ramp, and crack propagation was induced by applying a bending moment at the end of the specimen as shown in Figure 5.16. The nature of the fracture surface was examined to determine the depth of the crack, growth mechanisms, and microstructure.

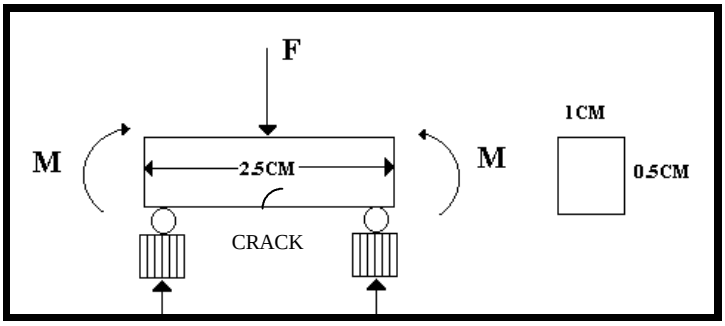

Figure 5.16 Diagram showing force F being applied to the specimen, causing two equal and opposite bending couples.

5.3.1.1 Choice of Cracks

The cracks observed in all three camshafts were suspected to be fatigue cracks due to the cyclic loading of the follower on the lobe s surface. Only a few cracks found on the most abusively ground lobes are suitable for fracture mechanics studies. For our method, the cracks need to be long and deep in order to allow the lobe to be split , exposing the fracture surface. The crack locations chosen for this experiment are as given in Table 5.2.

Table 5.2. Cracks chosen for fracture mechanics studies

CAMSHAFT ID	LOBE #	LOCATION	CRACK LENGTH	CRACK TYPE
V-13	3	Closing Ramp	7.4±0.1mm	straight
V-13	3	Opening Ramp	6.1±0.1mm	straight
V-15	3	Opening Ramp	2.6±0.1mm	pitted

As noted before, all but one of the cracks occurred in the opening ramp, at the onset of the nose region[†] . Only one crack was found in the closing ramp of all 24 lobes examined. This crack was the longest crack found, extending outside the roller s path (see Figure 5.17(A)). Due to its nature and size, this crack was a logical choice for fracture mechanics studies. All the cracks in the opening ramp fell into two categories: pitted or straight. The cracks differed in the way they propagated across the lobe s surface. Straight cracks were usually a factor of 2-3 longer than pitted cracks. Pitted cracks, on the other hand, were concentrated in areas of extreme wear damage. Therefore, of the remaining two cracks chosen for fracture mechanics studies, one was pitted and the other straight, as seen in Figure 5.17(B) and 5.17(C).

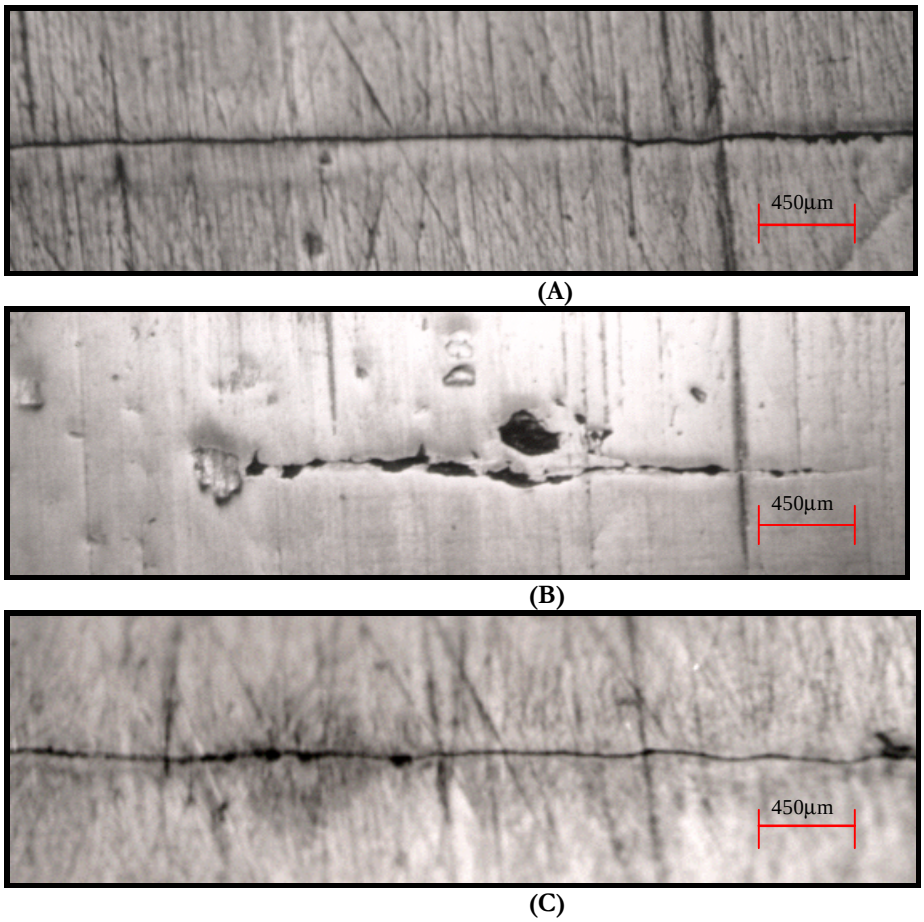

Figure 5.17 Fracture mechanics cracks: (A) Crack found in the closing ramp of lobe 3, camshaft V-13 (B) Crack found in the opening ramp of lobe 3, camshaft V-15 (C) Crack found in the opening ramp of lobe 3, shaft V-13.

[†] A single crack was found in the closing ramp and 34 cracks were found in the opening ramp

5.3.1.2 Bending Test

After the cracks were chosen, the lobes were sectioned using a diamond cutting wheel. Cutting speeds and coolant flow were selected so as not to overheat or damage the surface of the lobe. Each crack was covered with a protective adhesive prior to cutting. There were two main concerns when cutting the test specimens:

1. The lobes had to be sectioned to a depth greater than the crack itself. The thickness, in the other hand, had to be kept to a minimum so as to avoid large bending stresses in the testing machine and the specimen.

2. The geometry of the specimen around the crack needed to be as symmetrical as possible to insure proper crack propagation and avoid slippage of the specimen during testing. This task was not easy due to the asymmetrical curvature of the lobe. Figure 5.18 shows the specimen geometry prior to testing.

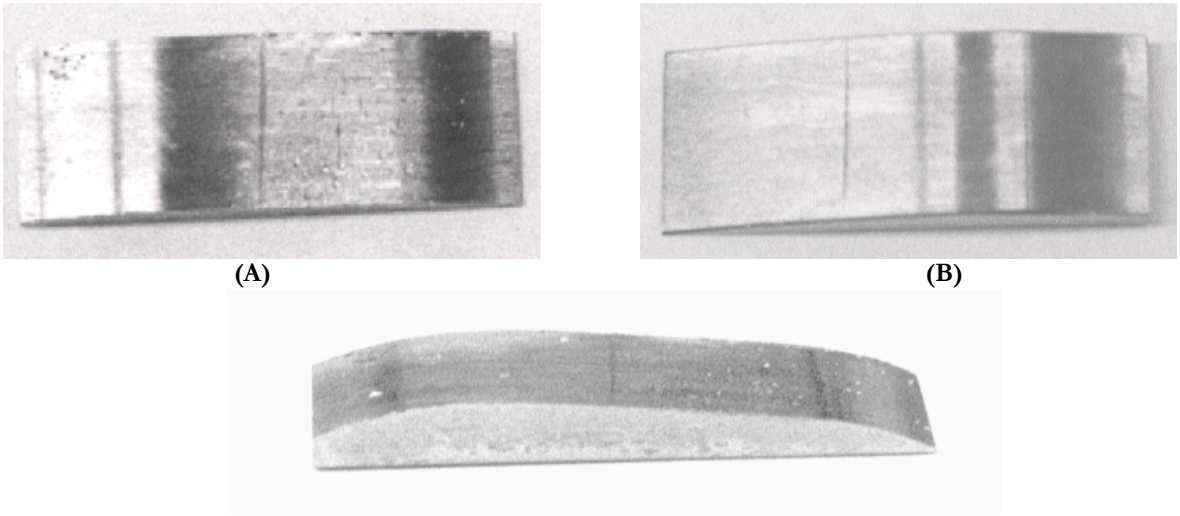

Figure 5.18 Specimen s geometry prior to testing. Cracks found on lobe 3 of camshaft V-13 (A) Opening ramp (B) Closing ramp (C) Side view of testing specimen showing an uneven surface curvature.

The specimens were tested in a Instron testing machine. Figure 5.19 shows the experimental setup with the specimen in place, ready for loading.

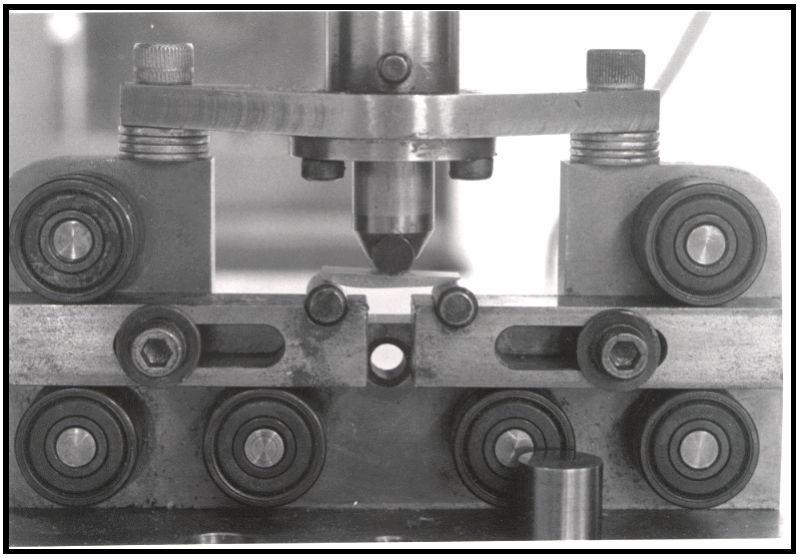

Figure 5.19 Experimental setup showing the specimen prior to loading

Typical loading histories are shown in Figure 5.20 below:

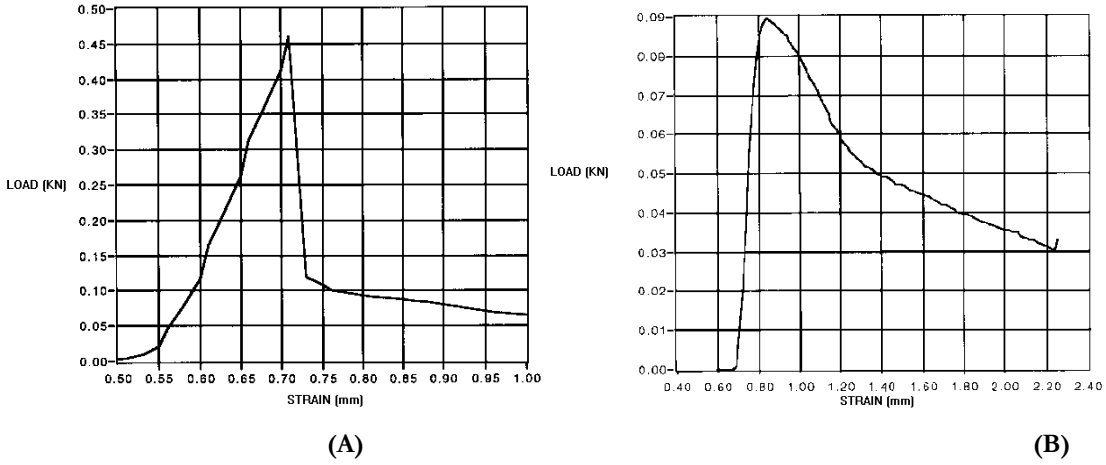

Figure 5.20 Load/strain plots. Crack found in (A) opening ramp and (B) closing ramp of lobe 3 in camshaft V-13

Notice in Figure 5.20(B) that the crack found in the closing ramp propagated in a more ductile manner than the other two cracks, as indicated by the broadening of the peak load over almost 1mm.

5.3.1.3 Fracture Surfaces

The fracture surfaces shown in this section are representative of two types of cracks: pitted and straight. A closer look at these surfaces provides useful evidence of the loading history, material quality and environmental effects on the surface of the cam.

The crack found in the closing ramp was the longest (about 7.4mm in length) and fell in the category of a straight crack (see Figure 5.17(A)). A lateral view of the resulting fracture surface is shown in Figure 5.21.

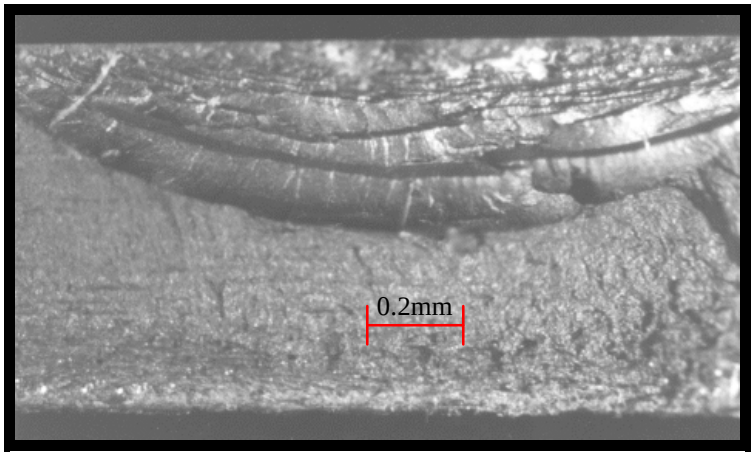

Figure 5.21 Fracture Surface of crack found in the closing ramp of lobe 3, camshaft V-13.

This fracture surface reveals unique characteristics. Lines emanating from the surface of the specimen go as far as 200μm, resembling flowing lava , not quite the typical beach marks found in fatigue fracture surfaces. Figure 5.22 shows an enhanced picture of these lines.

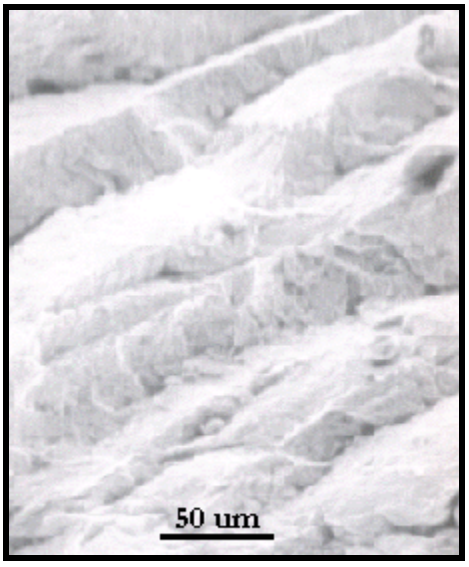

Figure 5.22 Flowing Lava fracture surface lines.

A very different fracture surface was obtained from the pitted crack found in the opening ramp of lobe 3 (Figure 5.17(B)), camshaft V-15 as depicted in Figure 5.23.

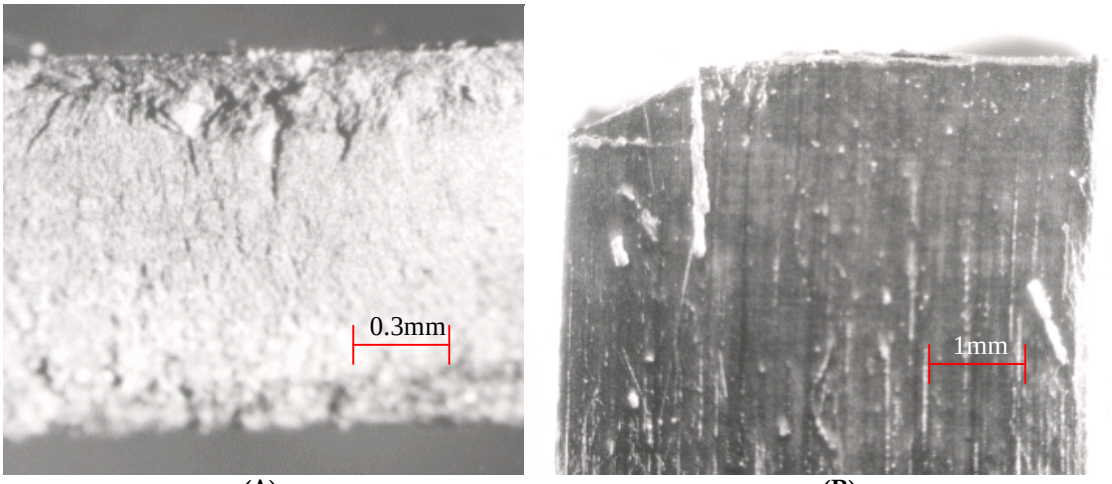

Figure 5.23 (A) Fracture surface for the opening ramp region of lobe 3, shaft V-15 (B) Fracture surface viewed from the top.

Instead of the flowing lava characteristics seen the fracture surface for the closing ramp crack, this fracture surface shows a shallower effect. A view from the top of the fracture surface shows that the crack propagated nonlinearly around a heavily pitted area.

The straight crack found on the opening ramp of lobe 3, camshaft V-13 (see Figure 5.17(C)) exhibited similar characteristics to the one found on the closing ramp i.e. a straight crack with no surface pitting. Figure 5.24 below shows this fracture surface.

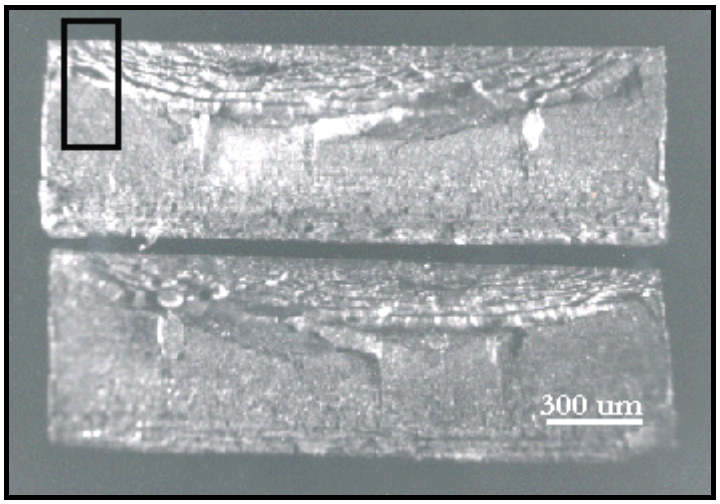

Figure 5.24 Back to back fracture surfaces for a straight crack found in the opening ramp of lobe 3, camshaft V-13. See Figure 5.25 for expanded view of marked region.

As expected, the fracture surface for the straight crack depicted in Figure 5.24 shows the flowing lava appearance previously observed. In order to capture all features from the top surface of the lobe to the inner core region, a collage of SEM micrographs was taken of the area delineated by the white square in Figure 5.24. These micrographs, seen in Figure 5.25, show three distinct regions of the fracture surface. The top region shows dark areas of grinding burn and debris. The middle region is characterized by white lines that give the fracture surface the flowing lava appearance. Unlike typical fatigue fracture surfaces where curved lines concentric about the crack origin are often seen and mark the progress of the crack (beach marks)[61], these lines may be explained by a rubbing behavior along the inner walls of the crack. Rubbing surfaces could have been promoted by the normal force generated by the follower as it traverses one side of the crack to the other. Finally, the bottom region shows the brittle inner core of the lobe to depths greater than 300µm

Figure 5.25. Sequence of SEM micrographs showing the different characteristics of the fracture surface from Figure 6.14.

5.3.2 Metallography

The lobes selected for microhardness testing (Table 5.3) were prepared for metallographic studies. The following list outlines the experimental procedure:

1. Lobes were sectioned in half along the opening ramp (starting at 328° and ending at approximately 270° as shown in Figure 5.26)
2. Specimens were plated with Nickel for edge retention
3. Plated specimens were then mounted and polished.
4. Polished surfaces were etched with aqua regia.
5. Regions of rehardening burn and temper burn were photographed
6. The interior portion of each lobe, after etching, was examined and photographed (see Figure 5.27).

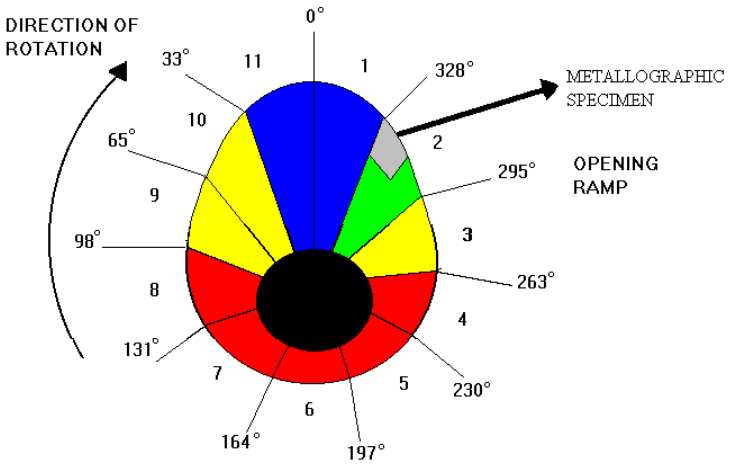

Figure 5.26 The degree location of the metallographic specimen seen in Figure 5.28 is marked as the gray area. Remember that zone 2 (green) is where most of the wear and cracking occurred round the lobe.

After etching, the interior portion of the lobe was examined. Figure 5.27 shows that the induction hardened regions extends to about 1.6mm below the surface of the lobe, as represented by the middle dark layer. The softer core region (bottom white) starts at about 2mm deep into the material.

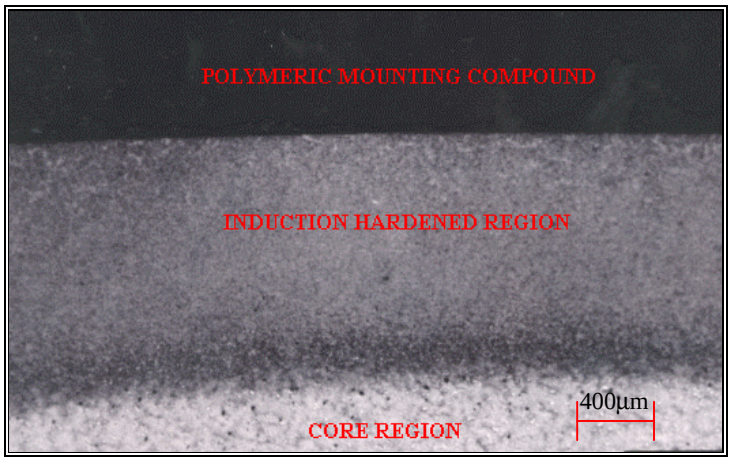

Figure 5.27 Micrograph of the metallographic specimen across the opening ramp. Two regions are exposed after etching: Induction hardened and core regions.

Grinding burn within the grinding affected zone (the first 100µm nearest to the surface), was found in the most abusively ground lobes 1 and 2. Figure 5.28 shows a portion of the specimen taken from the opening ramp of Lobe 2 (note that the thin white surface layer about 20µm thick is plated Nickel for edge retention).

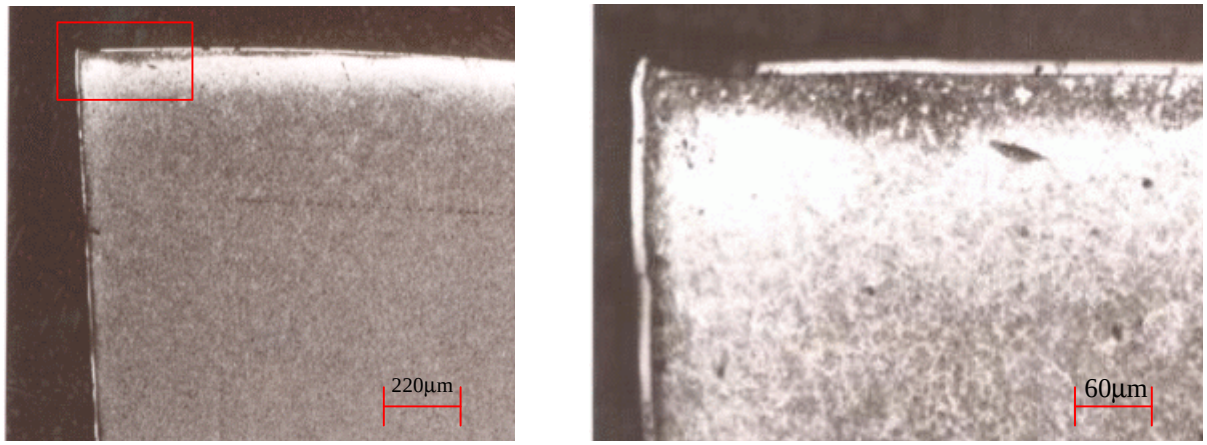

Figure 5.28 (A) Burn mechanism seen in the opening ramp of lobe 2, camshaft V-11. (B) Enhanced view of the portion of the lobe marked by the red rectangle.

Note from Figure 5.28(B) that the layer formed by the first 30µm to the surface experienced temper burn, as indicated by dark regions which reflect an increase in the size of carbides. The section of the lobe depicted in Figure 5.28(A) and (B) is where most of the cracking occurred. Its exact degree location with respect to the nose and the base circle is shown in Figure 5.26.

Lobe 1 in camshaft V-13 was also examined for burn. Unlike lobe 2 in shaft V-11, the grinding affected zone (first 30μm to the surface) of lobe 1 showed regions of rehardening burn as seen in Figure 5.28. Regions of rehardening burn lighten, as martensitic regions preferentially etch leaving behind a light retained austenite phase.

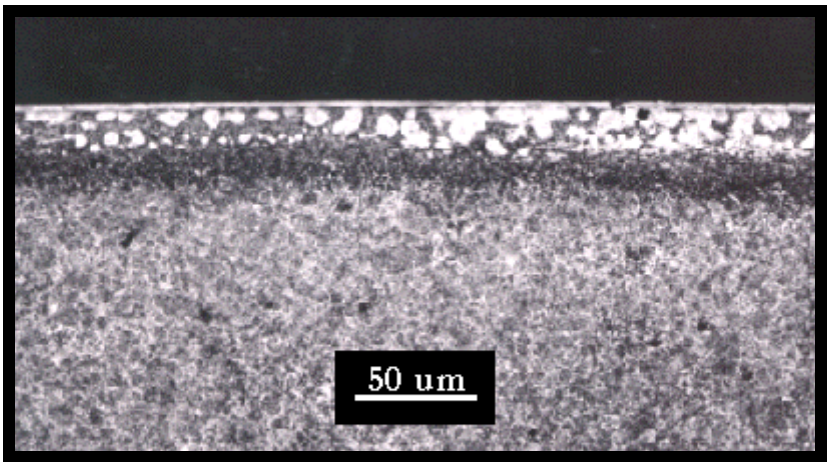

Figure 5.28 Burn found in the opening ramp of Lobe 1 of camshaft V-13

5.3.3 Microhardness

Metallurgists define hardness as resistance to permanent deformation. Hardness is measured by means of an indenter of a particular geometry which is pressed into the test specimen at a given load. The hardness value is calculated by measuring the ratio of the applied load to some measure of the size of the indentation.

In many instances, the engineer is required to explore hardness variations over small areas. Microhardness techniques allow the determination of hardness gradients in the micro-scale level by placing small indentations on the surface of the sample.

In the case of the cam/follower system, the thermal effect induced by the grinding wheel on the lobe can cause the induction hardened lobe to soften locally (temper burn), or it can increases hardness (rehardening burn), depending on the temperature reached at the lobe-follower interface. By measuring the microhardness as a function of depth below the lobe s surface, the thermal effects of grinding can be characterized. Two methods were employed: Nanoindenter and Knoop hardness.

5.3.3.1 The Nanoindenter

The Nanoindenter uses load and displacement data collected throughout the indentation process to determine the hardness. The area of the indent is calculated from a knowledge of the geometry of the tip of the diamond indenter. The load is constantly monitored, allowing hardness to be reported as a function of displacement. Measurements of sample stiffness from unloading data permit a separation of the plastic and elastic components of displacement, and the projected areas for indents can be calculated on the basis of the plastic depth of the indents[62]. Figure 5.29 shows a schematic of the Nanoindenter.

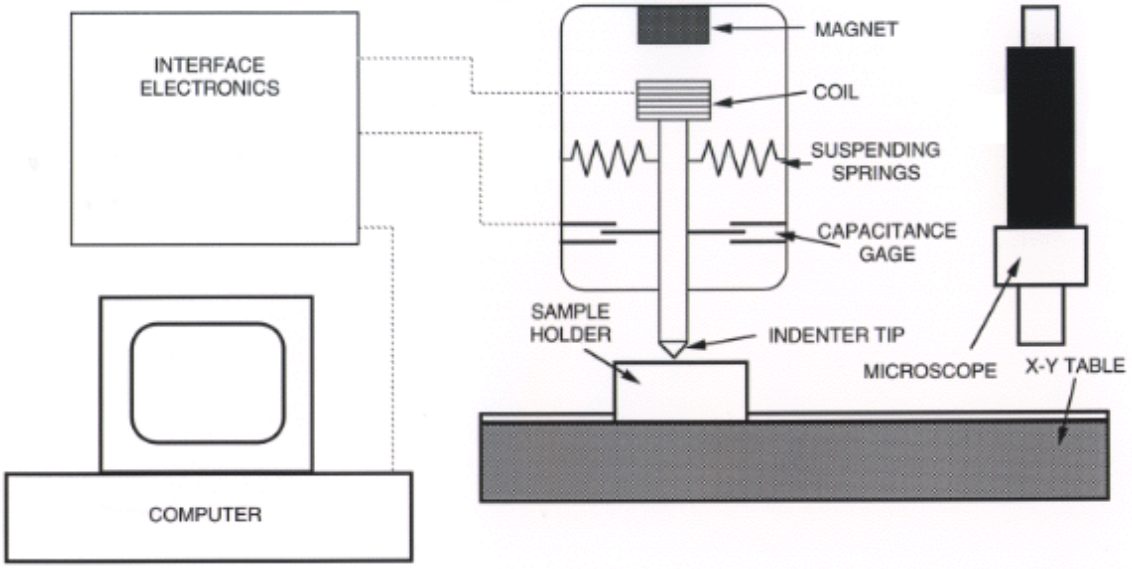

Figure 5.29 Schematic Diagram of the indenting mechanism of the Nanoindenter (Courtesy of L. Ritchter at Oak Ridge National Lab)

The Nanoindenter bypasses the need to image very small indentations to arrive at a harness number. Its major advantages are excellent resolution (it can measure indent depths to ±0.2nm), repeatability, and the ability to achieve single phase resolution in multiphase alloys[63]. Four lobes were prepared for microhardness measurements as shown in Table 5.3.

Table 5.3 Lobes chosen for microhardness measurements

LOBE #	ID	TESTING TIME	COMMENTS
2	V-11	100 HOURS	The greatest # of cracks were found on lobes 2 & 3
7	V-11	NOT LOADED	Hardness measurements of a lobe prior to SVI testing
1	V-13	336 HOURS	One expects to find the greatest # of cracks on the most abusively ground lobe 1. That this is not the case is a curious anomaly, likely to be a temperature dependent effect which could be revealed by hardness measurements
7	V-15	NOT KNOWN	Grooves were found on the nose region (≈1800 μin deep)

All four lobes were sectioned in half perpendicular to the shaft axis and coated with nickel to a thickness of 40μm for edge retention. The lobes were next mounted in a thermosetting polymer and polished down to a 1μm grit.

Microhardness measurements using the Nanoindenter were performed at Oak Ridge National Laboratory. Hardness data were taken in sets of five indentations at each depth, 15 μm apart near the surface and about 50 μm apart in the inner core of the lobe (measurements were taken as deep as 300 μm). An optical micrograph of the lobe s surface showing the indentations made by the Nanoindenter is seen in Figure 5.30 below.

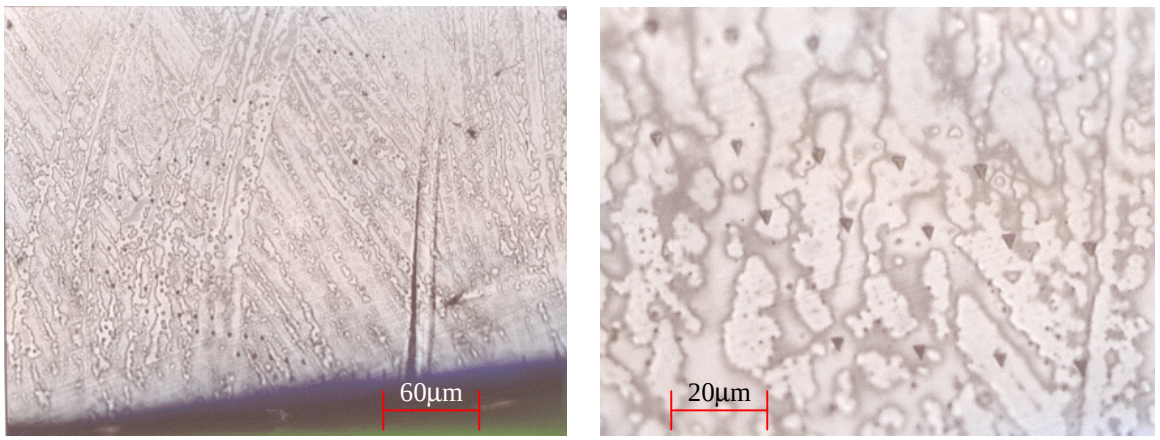

(A) **(B)**

Figure 5.30 (A) Micrograph showing the lobes surface, with small indentations located to the left of the mark. (B) A magnified view of the triangular indentations grouped in sets of five at each depth.

The lobes were not etched until the Nanoindenter measurements were complete; otherwise, it would have been difficult to accurately measure the indent dimensions. Knoop hardness measurements were made after metallography, allowing measurement of the hardness at the precise location of burn exposed by the etchant.

Hardness data showed a similar trend for lobes 2 and 7 of camshaft V-11. A slight surface hardening is seen in the first 20 μm of lobe 7. Lobe 1 in camshaft V-13 showed a different trend as seen in Figure 5.31. Surface hardness for this lobe was measured at about 6.5 GPa, a significantly lower value than for the other two lobes which showed surface hardnesses in the viscinity of 8 GPa. Lobe 1 experienced softening in the first 30 μm (grinding affected zone), with hardness values increasing rapidly in the inner core (at about 7.4 GPa at 100 μm).

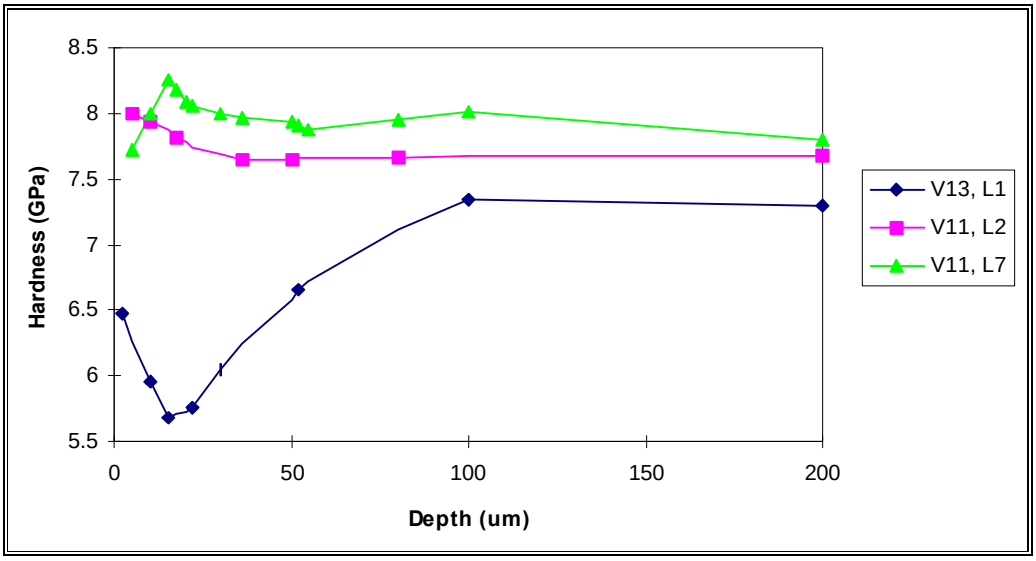

Figure 5.31 Nanoindenter microhardness versus depth at the opening ramp for lobes receiving different levels of abusive grinding.

Measurements using the Nanoindenter were made at arbitrary locations in the opening ramp. It was not until the specimens were etched that one was able to pinpoint the exact location where burned occurred.

5.3.3.2 Knoop Hardness

The Knoop hardness indenter is a sensitive diamond indenting tool suitable to measure the hardness change in hard steel resulting from grinding burn. The Knoop indentator is ground to a pyramidal form that produces a diamond shaped indentation having long and short diagonals of approximate ratio of 7 to 1. By keeping the long axis parallel to the surface of the sample and adjusting the applied load, it is possible to measure microhardness at intervals of 10um without overlap (zigzag pattern).

The test has several limitations[64]:

1. the samples need to be scratch-free and mounted normal to the testing surface,
2. small loads produce very small indentations and the error associated with the location of the actual ends of the indentation becomes greater, and
3. the part being tested must be thick enough to prevent any bulge or other markings from appearing on the surface opposite to the indentation.

The Knoop hardness number is obtained by measuring the ratio of the applied load to the unrecovered projected area according to the following equation[65]:

$$\text{Knoop Hardness } (H_k) = \frac{L}{A} = \frac{L}{l^2 C_P}$$

- L = Load (in Kg)
- A = unrecovered projected area of indentation (mm^2)
- l = measured length of long diagonal
- C_p = Constant relating l to the projected area

Knoop hardness measurements were taken on the same lobes listed in Table 5.3 using a load of 50 grams. The error associated with the light load chosen for indentation was counterbalanced by the need of small indentations within the first 50 μm of the surface (thermal damaged zone). These lobes were first etched, exposing regions of temper burn and rehardening burn. As many as 10 hardness readings on each lobe have been obtained by staggering the indentations in a zigzag pattern. Readings were taken in 15 μm increments near-surface, then at 50 μm to a depth of 200 μm. Hardness gradients were obtained at different regions of thermal damage, specifically where the lobes showed the highest degree of cracking.

Knoop hardness profiles were obtained in regions where microstructures indicated either tempering or rehardening These gradients provided more indicative results of the hardness variations where cracking occurred in the opening ramp.

A much different trend was obtained with Knoop hardness than for the Nanoinenter data. Lobe 1 experienced rehardening burn in the first 30 μm from the surface as seen in Figure 6.21. Lobe 2 and Lobe 7, in the other hand, experienced a slight softening in the first 30 μm. All three lobes reached stable hardness values in the inner core of the lobe (after the first 100 μm).

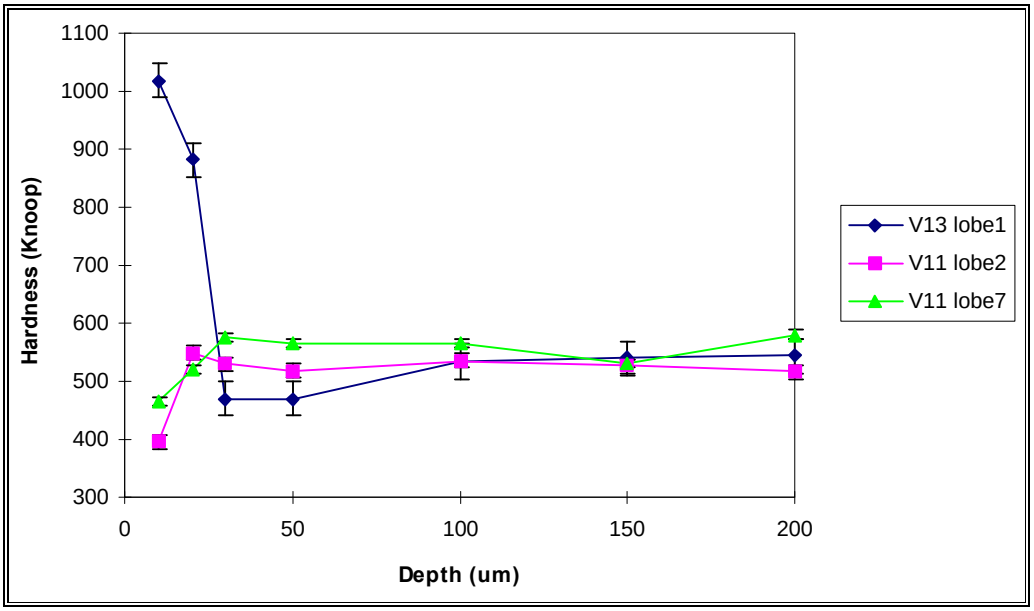

Figure 5.32 Knoop microhardness versus depth for Lobes receiving different levels of abusive grinding (Lobe 1 is the most abusively ground, Lobe 7 is the least). The effects of burn are most severe nearest to the surface.

5.3.4 X-ray Residual Stress Measurement

The basis for the use of X-rays to measure residual stresses in materials lies in the Bragg s law for diffraction given below:

$$n\lambda = 2d\sin\theta; \quad (1)$$

where n is an integer denoting the order of diffraction, λ is the wavelength, d is the lattice spacing of the crystal planes, and 2θ is the diffraction angle.

A Cr x-ray tube produces one very intense wavelength λ. A polycrystalline material is composed of atoms arranged in planes with some spacing d. Because X-rays are electromagnetic radiation, they are scattered by the electrons in the atoms. An x-ray detector is moved over a range of angles 2θ to find the angle, θ, that satisfy Bragg s law. When this geometric condition is satisfied, waves are scattered from successive planes, adding constructively. Thus, the difference in the paths of the scattered beams from these planes is a multiple n of the wavelength λ[66] (Figure 5.33).

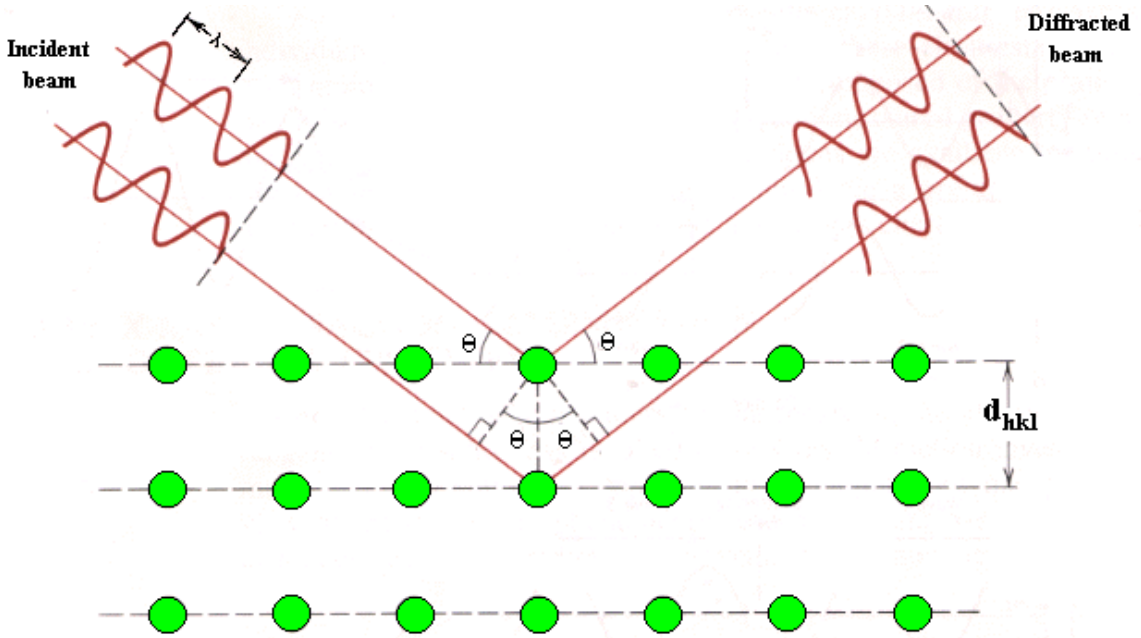

Figure 5.33 X-ray radiation of wavelength λ being diffracted by a plane of atoms.

This diffraction takes place from a thin surface layer about 5-20 um thick, depending on the X-ray wavelength and atomic number of the sample. If the surface of the specimen is in compression (in the plane of the surface), the d-spacings of these planes parallel to the surface is larger than in the unstressed state, while those planes perpendicular to the surface are less than in the stress free material. Conversely, when tensile stresses are encountered, the d-spacings of the planes parallel to the surface are smaller, while those perpendicular to it are larger. Basically, the parameter of interest is the microstrain, as measured by the change in interplanar spacing.

Lattice strains are determined from the peak positions of the diffraction curves at different directions of ψ (angle between the normal to the diffracting lattice planes and the sample surface). If there is no stress in the sample, the diffraction curves will superimpose However, the presence of stresses will reduce the uniformity of the d-spacings, causing a peak shift as seen in Figure 5.34. Microstrains are calculated from these peak shifts and then converted into stresses using Hooke s law and the X-ray elastic constants.

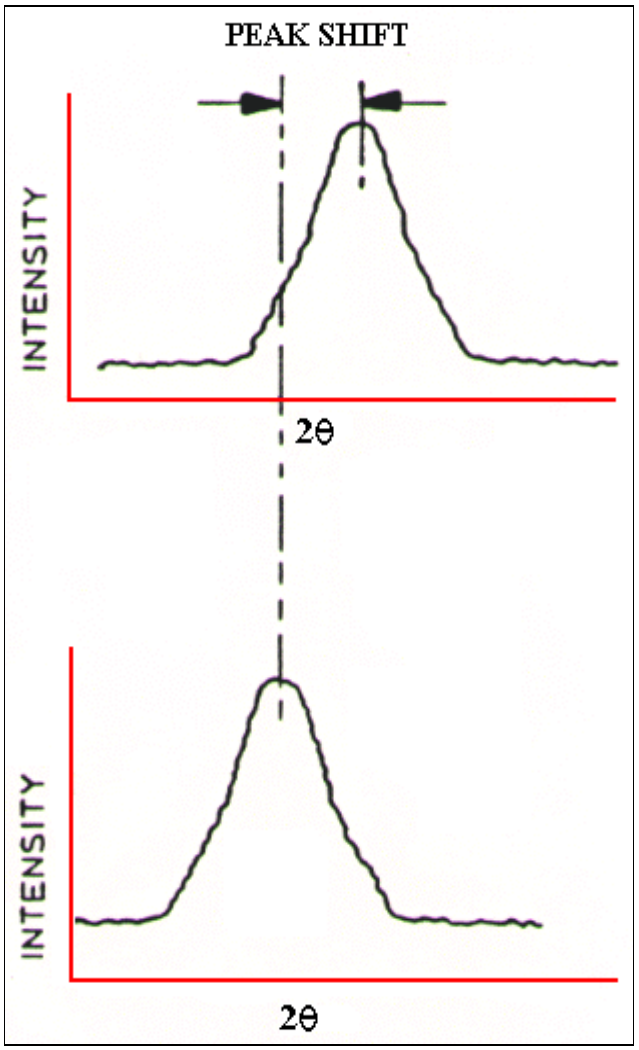

General uses of X-ray diffraction residual stress techniques are the determination of subsurface residual stress distributions, nondestructive surface residual stress measurement for quality control, and measurement of residual stresses associated with failures caused by fatigue or stress corrosion.

Some of the limitations of this technique are: (i) it requires expensive, delicate apparatus and is generally limited to a laboratory shop (ii) only a shallow surface layer is measured, requiring electrolytic etching to remove layers for subsurface measurement, and (iii) the samples must be polycrystalline, of reasonably fine grain size, and without texture.

Figure 5.34 Plots of intensity vs. angle of tilt showing peak shift

As reported by Liurade[67], the fatigue strength of engineering parts is affected by residual stresses by the following factors:

- the tri-axiality or the condition of the residual stress,
- the value, the direction and the orientation of these stresses compared to the applied stress field,
- the strength of the material in the highly-stressed areas, and its ductility,
- the amplitude of the applied cyclic stresses,
- the treatment or the process used to create the residual stresses, and
- the effect of residual stresses on their stability

However, Wohlfahrt[68] stated that for hard steels (which is the case for SAE 52100), it is the distribuition of the residual stresses with respect to the depth, compared to the applied stresses, which is important for the fatigue strength.

X-ray residual stress measurements were made using the TEC PARS 1610 x-ray stress analysis system. Figure 5.35 shows the experimental set up for x-ray diffraction residual stress measurements.

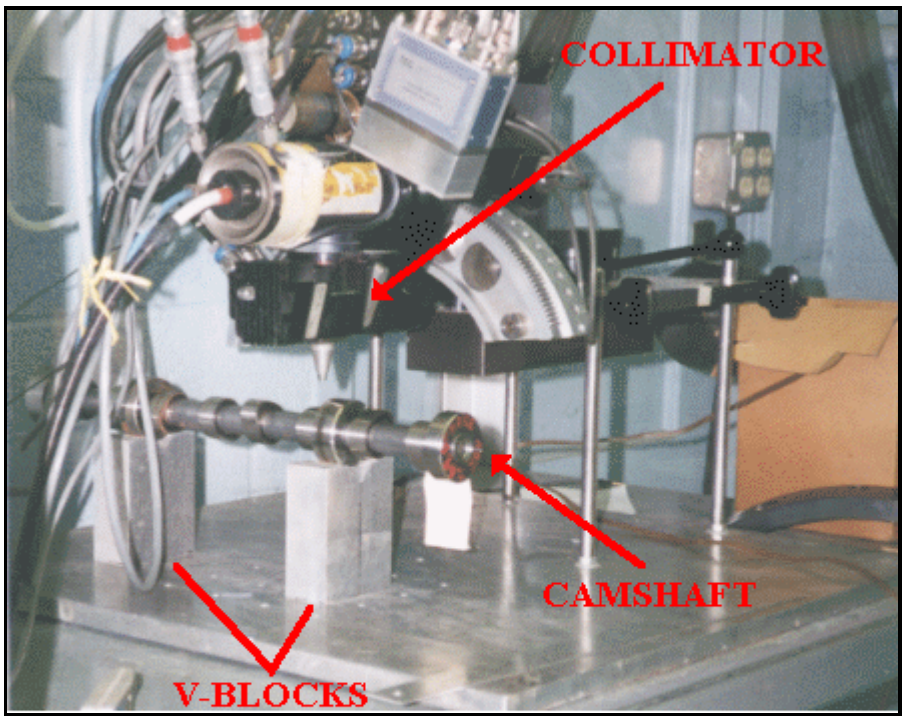

Figure 5.35 X-ray collimator from TEC PARS 1610 system poised over a SVI-tested Kulhanek (2.3L) camshaft.

Data were taken using chromium radiation diffracted from the (211) planes of steel. This offered the duplex advantage of large 2θ angle and high multiplicity (M=24), thus offering good detected intensities, sensitivity to peak shifts, and low errors. Speed was achieved through the use of one-dimensional position-sensitive proportional counter. All x-ray residual stress measurements were made in the axial direction as a function of depth. Only the opening ramp region was examined, where cracking mostly occurred. A total of 19 residual stress profiles were generated.

Lobes were strategically selected to cover all levels of grinding (gentle, moderate, abusive) as seen in Appendix A (experimental matrix). Table 5.4 lists the lobes selected for this study along with the depth of measurement (depths differed depending on how far the tensile stress filed extended down the bulk of the cam).

Table 5.4 Lobes selected for residual stress measurements

Camshaft ID	Lobe #	Depth (μm)
V-11	1	300
V-11	4	250
V-11	5	250
V-11	6	200
V-11	8	150
V-13	2	200
V-13	4	250
V-13	5	250
V-13	6	250
V-15	1	250
V-15	2	250
V-15	4	250
V-15	5	250
V-15	6	250
V-15	8	150
V-2 (Courtney)	1	250
V-2 (Courtney)	2	250

All layer removal was performed using a Proto Manufacturing Model 8818 portable electropolisher. This device lets the user set voltage, timer and flow rate; corrosion current is limited to 3 amperes and is determined by area of contact, corrosive agent, and applied voltage. The etchant used in this device was a supersaturated salt water solution comprised of 90 grams of salt dissolved in 500ml of distilled water serving as the electrolyte. This was quickly and cheaply created by agitating rock salt in distilled water, then pouring the supersaturated solution through a coffee filter into the electropolisher storage tank. Calibration of etch depth with time yields an electropolish time of 12 seconds for 10±2μm in depth[69].

A plot of several axial x-ray diffraction residual stress profiles for camshaft V-11 is given in Figure 5.36. All measurements were made in the opening ramp to a depth of 250μm.

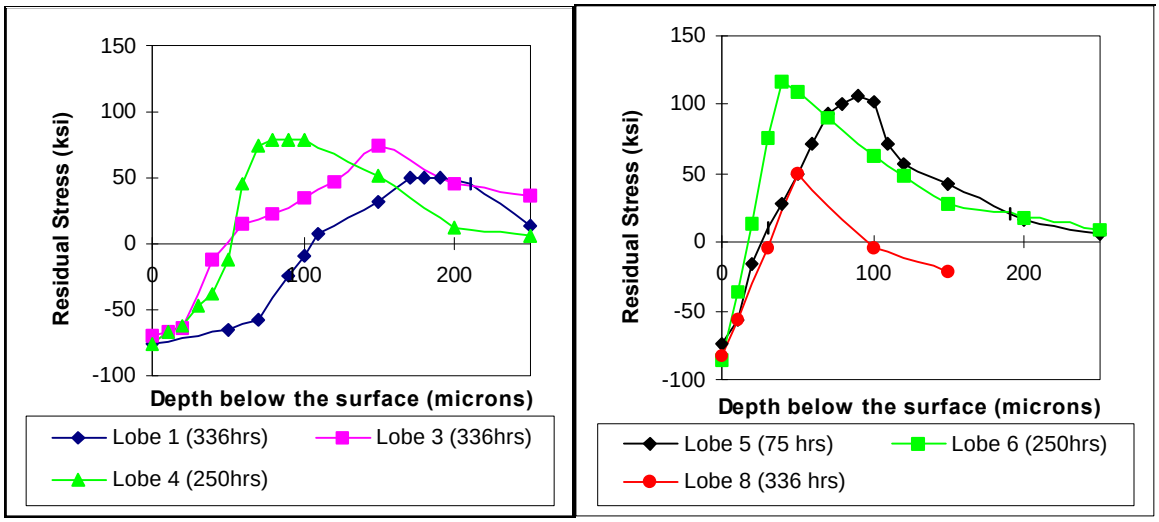

(A) **(B)**

Figure 5.36 X-ray residual stress profiles with depth at the opening ramp of Camshaft V-11 (A) Lobes 1, 3 and 4, and (B) Lobes 5, 6, and 8.

Figure 5.36 shows that all measured residual stress at the surface are compressive. In addition, depth profiles do not follow the grinding stresses as determined by Courtney (see Figure 2.1). The lobes that received the largest depth of cut (most abusive grinding) did not exhibited the highest tensile peak residual stresses. For these lobes (Figure 5.36(A)), peak stresses occurred significantly deeper into the material (at approximately 200 μm) than the pre-tested stresses seen in Figure 2.1. Lobes ground with the smallest depth of cut (mild grind) showed peak tensile residual stresses close to 100ksi (except for lobe 8) closer to the surface of the lobe, whereas before SVI testing, these stresses were completely compressive. Similar plots for residual stress, to depths of 250μm, in the opening ramp of camshaft V-13 are seen in figure 5.37.

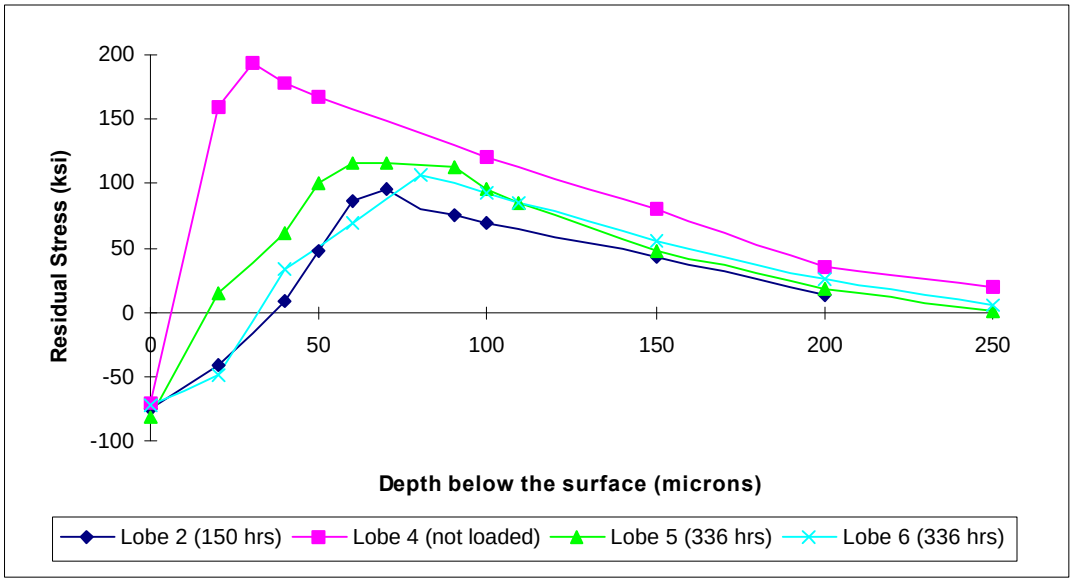

Figure 5.37 X-ray residual stress profiles with depth for the opening ramp in camshaft V-13. Notice that lobe 4 was not tested in the engine simulator.

The largest peak tensile residual stresses in Figure 5.37 corresponds to lobe 4 (which was not loaded) with a value of almost 200ksi. For the remaining three lobes, peak tensile residual stresses appear at depths of 75 to 100μm below the surface, with values much lower than lobe 4 at approximately 100 ksi. Again we see the reduction in the value of the peak tensile residual stress for tested lobes similar to the stress profiles for camshaft V-11. These lobes peak in the range of 75 to 100 ksi, deeper into the material at about 75 μm. Finally, Figure 5.38 shows x-ray residual stress profiles for the remaining camshaft V-15. The profiles are plotted in two graphs for sake of clarity.

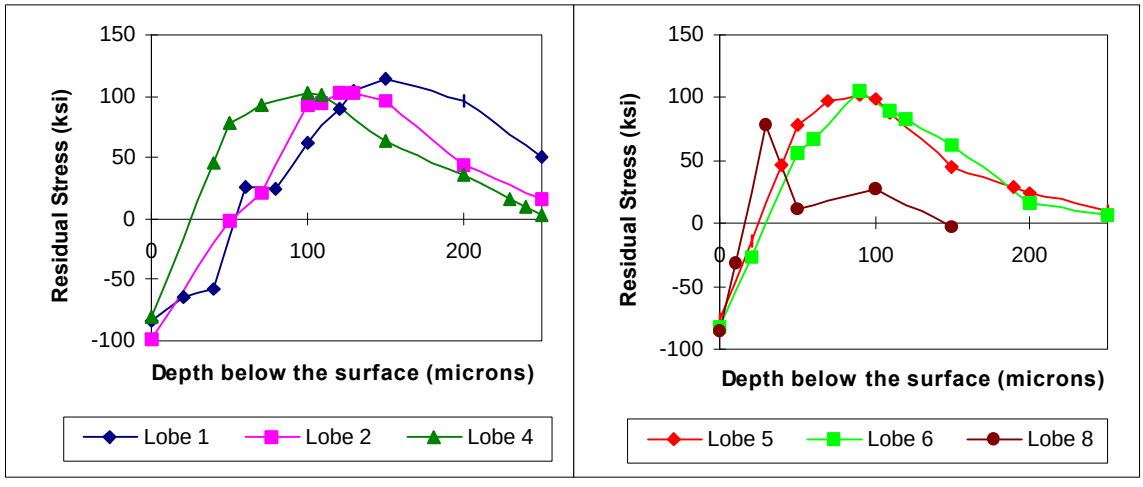

(A) **(B)**

Figure 5.38 X-ray residual stress profiles with depth at the opening ramp of camshaft V-15. (A) Most abusively ground lobes 1, 2, and 4. (B) Gently ground lobes 5, 6, and 8.

From these data, it is seen that the peak tensile residual stress for the most abusively ground lobes is approximately 150μm below the surface — some 5 times deeper than that observed by Courtney. It is also noted that the peak tensile residual stress for abusively ground lobes did not differ much from the moderately ground lobes (most profiles peak approximately at 100 ksi). This result is distinct to what Courtney measured (see Figure 2.1), who found peak tensile residual stress for lobe 2 to be twice as large as for lobe 4.

From the residual stress data presented in this section, the following key observations can be made:

1. after SVI-testing, a change in the stresses is observed, resulting in a reduction of the initial stresses,
2. peak tensile residual stresses shifted deeper into the material, and
3. residual stresses appear to stabilize after a certain number of cycles, regardless of the level of grinding.

Chapter 6

DISCUSSION

Liberty without learning is always in peril, and learning without liberty is always in vain

¾ *John F. Kennedy, May 18, 1963.*

Research objectives established at the beginning of the project called for a better understanding of the grinding process and it s effect on the workpiece residual stress state. More important for design engineers, however, is the vinculum between induced residual stress and lifetime of the cam lobe. This chapter addresses this problem by linking the results found experimentally to the contact stress and fatigue life analysis presented in Chapters 3 and 4. An attempt is made to present each aspect of this analysis/discussion in a logical order by dividing the chapter into subsections, each one addressing a different experimental observation.

Cracking occurred almost exclusively in the opening ramp:

Microscopy results show the highest degree of pitting to occur at the ramps. Moreover, experimental results show cracking to occur almost exclusively at the opening ramp, onset of the nose region. The force analysis presented in Chapter 3 indicates that the dynamic and static loading forces are greatest in the nose, and that the distribution of forces is almost symmetric between the ramps (Figure 3.6). Therefore, the observed statistically significant increase in the number of cracks in the opening ramp is most likely due to the residual stresses due to grinding. Courtney s data show the greatest normal grinding force to occur at the opening ramp (see Figure 6.1). Consequently, higher grinding forces generate higher temperature gradients that produce larger subsurface tensile residual stresses which facilitate crack initiation.

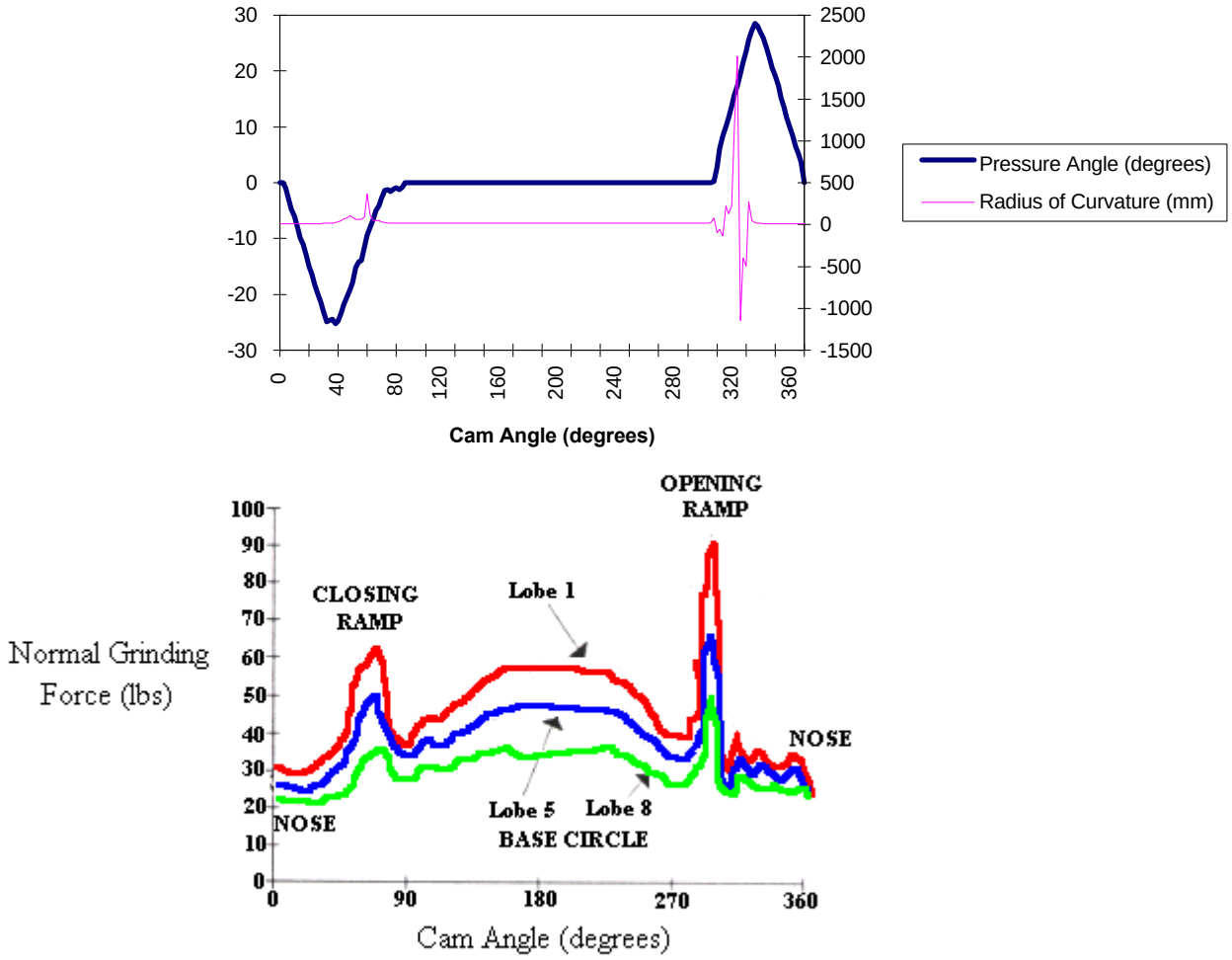

Figure 6.1 Relationship between lobe geometry and grinding force. X-axis for both plots is the same (Courtney[70])

The imbalance between forces in the opening and closing ramps may be caused by lobe geometry. The radius of curvature goes to infinity (convex) at approximately 320° to 330°, dictating a faster acceleration at the opening ramp. The drastic change in radius of curvature induces higher normal grinding forces (as a direct result of the increase in contact area between the grinding wheel and the lobe). It is at this location (~320° to 330°) where all the cracking took place (see Figure 5.5).

The correlation between residual stress and damage production:

Wear prediction is an important parameter to be consider when implementing a method to predict the lifetime of a lobe. Therefore, a link between the grinding process and damage production is needed. The engineer should be able to determine and estimate unacceptable wear via a judicious control of the grinding process, which is influenced by a host of variables such as work speed, stock removal rate, and wheel sharpness. The ultimate goal is to be able to generate favorable surface residual stress (subsurface compressive stresses) and improve fatigue characteristics.

Peak residual stress after testing was plotted as a function of the defect production rate (which includes cracks, pits, dents, scratches) for lobes in camshaft V-11 (Figure 6.2).

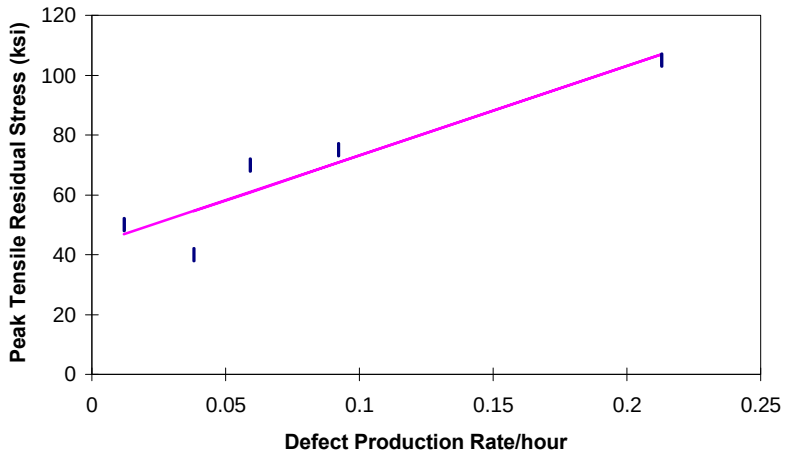

Figure 6.2 Peak tensile residual stress (after SVI testing) versus defect rate measured at the opening ramp of lobes in shaft V-11. Note that testing time was not the same for all lobes.

We find that the formation of defects at the opening ramp is stress dependent. Nevertheless, more fatigue data is need to be able to rationalize this dependency. An endurance limit related to the maximum tensile sub-surface residual stress can be set for quality control. For example, if we determine that an acceptable defect rate for production is 0.05 (which means that after 300 hours of service at 1200 rpm, 15 defects will be produced at the opening ramp), the corresponding peak tensile residual stress fall in the range of 50-60 ksi. These values correlate with values found for lobes 6, 7, and 8 prior to

testing. Hence, one can increase the depth of cut to 0.05 (Table 2.1) and still produce damage-free workpieces.

The difference between pitted and straight cracks:

Optical microscopy shows evidence that the nucleating sites for many cracks found in the SVI-tested lobes are grinding-induced rather than fatigue-induced. Small grinding cracks were found at the exact location (320° to 330° range) where straight cracks were found after engine testing. In addition, crack density in tested lobes versus as-ground (untested) lobes is similar. In other words, no grinding cracks are found in lobe 1, most occur in lobes 2, 3, and 4, and none are found in the gently-ground lobes 5,6,7, and 8. This results support the hypothesis that straight cracks were nucleated due to the localized thermal expansion produced by the friction between the abrasive grinding wheel and the lobe s surface and then propagated as a result of the cyclic loading during engine testing.

In comparison, nucleation of pitted cracks is assumed to occur due to the synergistic effect of tensile residual stresses due to grinding and the impact loads administered by the follower during SVI-testing. The fact that pitted cracks are only found in areas of extreme wear damage (spalling, pitting, dents) and that these cracks are much shorter than straight cracks (see Figure) uphold this beleif. In addition, the number of grinding cracks is less than the number of straight and pitted cracks combined. Thus, not all the cracks could have been nucleated due to the grinding process.

Scanning acoustic microscopy (SAM) results obtained during the nondestructive evaluation phase of the project indicated crack depths ranging from 200 μm to 250 μm. These results were confirmed by fracture surfaces showing the flowing lava characteristics as deep as 250 μm. Fracture mechanics studies also unveiled a significant difference between the fracture surfaces of pitted cracks and straight cracks. The mechanism of propagation of straight cracks appears fatigue like in some respects, but lava flow structure suggest the possibility of a lateral rubbing motion between the faces of the cracks. Normal forces delivered by the follower as it transverses one side of the crack to the other causes one side to deflect an amount δ with respect to the other side. Spacings between lava flow lines in Figure 5.21 are very small in the first 50 μm from the surface, but as the crack grows longer and deeper, local stresses are relieved and the deflection δ becomes larger, evidence of the increase in the spacings between lava flow lines from 50 μm to 150 μm into the material.

The mechanism of propagation for pitted cracks is not very well understood. It is believed that the cracks propagate by pits joining each other as they become close enough to each other. Individual pits are nucleated from small areas of material being flaked-off due to the coupled effect of impact loads and sharp residual stress gradients near surface. Photographs in the opening ramp of lobes tested to short times (75-100 hours) show very shallow pits, isolated from each other. Lobes tested to full time (336 hours) exhibit and increase in the density of both pits and pitted cracks.

The most abusively ground lobes showed the highest degree of cracking, except for lobe 1:

A correlation exists between an increase in crack density with increasing grinding infeed (and thus with residual stress), except for the most abusively ground lobe 1. This anomaly can be explained by microhardness results that show evidence of surface hardening of lobe 1 in the first 50 μm from the lobe s surface. Lobe 1 received the highest depth of cut which was accompanied by the highest normal grinding forces between the wheel and the workpiece, resulting in the highest temperatures (we speculate that temperatures above 700° Celsius were attained during grinding). Grinding temperatures for lobe 1 were sufficient to induce an austenitic phase transformation, with brittle martensite forming on rapid coooling by the lobe s inner core and the coolant. Rehardening of lobe 1 was further confirmed by metallography (Figure 5.28) which shows regions of rehardening burn to lighten after etching, as martensitic regions preferentially etch and leave behind a light retained austenite phase. Evidence of rehardening burn was also reporeted by Courtney[71], who measured a drop in Barkhausen noise amplitude (BNA) in the opening ramp of lobe 1 which correlates with hardening of the metal in burn regions. Grinding temperatures for Lobe 2 were not high enough to produce the rehardening of the lobes surface. This lobe experienced temper burn, as confirmed by the softening of the lobe surface at the opening ramp region to depths of approximately 50μm. Metallography confirms the presence of temper burn by the slight darkening of tempered regions, reflecting an increase in the size of carbides.

These results show that crack formation is inhibited by an increase in hardness due to rehardening burn. The increase of the yield strength in the highly-stressed surface layer (first 50μm) increases the fatigue strength of the material. Earlier research by Legus[72] also shows that an increase in the hardness generally has a beneficial effect on the fatigue characteristics

by increasing the endurance limit of the material. In addition to the increase in hardness, the distribution of the residual stresses with respect to depth may have a positive effect on fatigue strength. X-ray residual stress data show that peak tensile residual stresses migrated deeper into the material for lobe 1 (see Figure 5.36), becoming tensile at depths greater than 100μm. Crack initiation, which is expected to occur subsurface, will be retarded by the compressive stresses extending deeper into the material.

The formation of untempered martensite in the first 50μm is accompanied by localized thermal expansion of the material, due to the distortion of the ferrite lattice into a body-centered tetragonal (BCT) structure. This volume change creates local compressive stresses near surface. This process can be compared to the induction hardening of the outer-layer of the lobe in a micro-scale level.

Grooves found on the nose of camshaft V-15:

Profilometry results show no overbearing tribological effect on the surface of the cam. All three camshafts show a slight negative slope indicating that there is only a weak correlation between surface roughness and residual stress. Comparison of surface profiles across all three camshafts shows reproducibility of the experiment to be good. Plowing grooves parallel to the direction of rotation and SEM results suggest that camshaft V-15 is statistically different from camshafts V-11 and V-13. Possible explanations suggest that either the heat treatment or the metallurgy of camshaft V-15 is different from the other two shafts. However, neither microhardness nor metallography data taken on lobe 7 in camshaft V-15 shows any significant difference to support this theory. X-ray residual stress profiles taken at the opening ramp of various lobes in shaft V-15 also show inconclusive results.

Residual stress relaxation:

The residual stress fields were characterized only after the grinding operation. However, fatigue tests under the SVI engine simulator allowed us to study the aftereffect of loading on the preexisting residual stress fields. An assumption of stress relaxation (rearrangement of residual stress fields) was proposed by Girardin[73]. He stated that relaxation was possible over the first few cycles of loading via cyclic softening of the material. A model developed by Landgraf and Chernenkoff[74] was used to represent this behavior, in which the

relaxed mean stress after N cycles σ_{mNth} is computed from the original mean stress using the following equation:

$$\sigma_{mNth} = \sigma_{1st} (N)^{r} \tag{6.1}$$

where r is the stress relaxation rate:

$$r = 8.5 \times 10^{-2} \left(1 - \frac{\Delta e}{\Delta e_{th}} \right) \tag{6.2}$$

and $\Delta\varepsilon$ = applied strain range which can be calculated from the stress range

$\Delta\varepsilon_{th}$ = strain threshold relaxation below which relaxation can not occur

$$\Delta\varepsilon_{th} = 2\exp(-8.41+5.36*10^{-3}(HB)) \tag{6.3}$$

where HB= Brinell Hardness.

Girardin found that the residual stress fields within the grinding affected zone reached stability subsurface (after the first 600 cycles). He also noted that this phenomenon was more important on the burned lobes (lobes 1 and 2), with stresses at a depth of 25μm decreasing by 50% when stability was attained and by 35% at a depth of 50μm.

Earlier research[75] has shown that the stability of the residual stresses are affected by several factors, such as:

1. the nature and the mechanical properties (hardness, elastic limit) of the material,
2. the nature, the direction and the amplitude of the applied cyclic loading,
3. the number of loading cycles,
4. the direction, the level and the gradient of the residual stresses,
5. the temperature.

X-ray residual stress measurements performed after engine testing confirm the hypothesis of stress relaxation. The design of the experimental matrix purposely allowed one lobe in each camshaft to remain unloaded for this kind of study. Figure 6.3 shows residual stress gradients for lobe 4 (moderately ground) in all three camshafts.

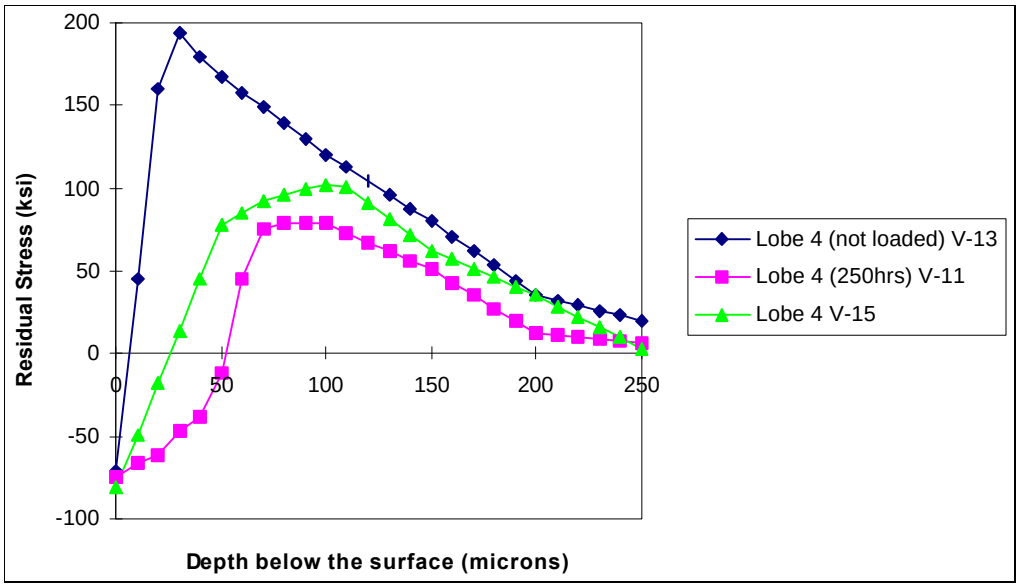

Figure 6.3. Evidence of residual stress relaxation. Note that the testing time for lobe 4, camshaft V-15, is unknown.

The unloaded Lobe 4, camshaft V-13 shows peak residual stress in the vicinity of 200 ksi, similar to those values found by Courtney, at a depth of about 30μm. The other two lobes exhibit peak stresses in the range of 75 to 100 ksi, half the value of the unloaded lobe. In addition, the residual stresses appeared to have migrated into the material, to a depth of about 100μm.

Another interesting observation is seen on the residual stress state of lobe 1 after engine testing. The reader is reminded that lobe 1 is the only lobe in which rehardening burn was seen, with the formation of untempered martensite in the first 50 μm from the surface. Tensile residual stresses for lobe 1 in both shaft V-11 and V-15 have migrated deeper than any other lobe, peaking at depths greater than 150 μm. The peak stress values have been relaxed to less than half the original value of 200 ksi observed by Courtney (their values are 45 ksi for lobe 1 of shaft V-11, and 105 ksi for lobe 1 of shaft V-15). This results suggest that the unstable BCT structure of untemepered martensite promotes a deeper relaxation .

Relaxation of the stresses seen in Figures 5.36, 5.37, and 5.38 may be determined by the movement of dislocations. Rolling contact loads generated by the follower may induce transformation of residual austenite into a more stable microstructure. Relaxation seems to stabilize after a certain number of cycles, as indicated by the bunching up of the residual stress profiles at about 100 μm and with values in the range of 50 to 100 ksi (even for the

moderately ground lobes). Stabilization after a determined number of cycles corresponds to the adaptation of the material resulting from the elastic limit of the material being exceed at the macroscopic level. This observation was confirmed by Girardin, who found that yielding may be anticipated at the opening ramp of the most abusively ground lobes.

X-ray diffraction peak width:

Courtney hypothesized that X-ray peak width may be used to estimate the degree of crystalline imperfection, hence serving as a tool to determine grinding burn[76]. Diffraction peaks broaden with the reduction in uniformity of d-spacings, and narrow as the uniformity of the crystal structure increases. This dual effect can be promoted by cold work in the case of peak broadening or tempering in the case of peak narrowing. X-ray peak width is affected by the following parameters:

- crystal size,
- nonparallel incident x-rays,
- a non-monochromatic beam, and
- subcrystals, regions of high dislocation density, and other means of micro strain inside the material.

X-ray peak width is measured by taking the full width of the diffraction peak at half maximum intensity (integral breadth). This value is calculated automatically by the TEC computer.

Courtney's FWHM data as a function of cam angle show the greatest peak narrowing to occur at the opening ramp (about 320°) for the most abusively ground lobes. Moreover, he reported a correlation between peak broadening and residual stress as shown in Figure 6.4. It is to be noted that these data should be representative of the pre-SVI testing results for the lobes reported here.

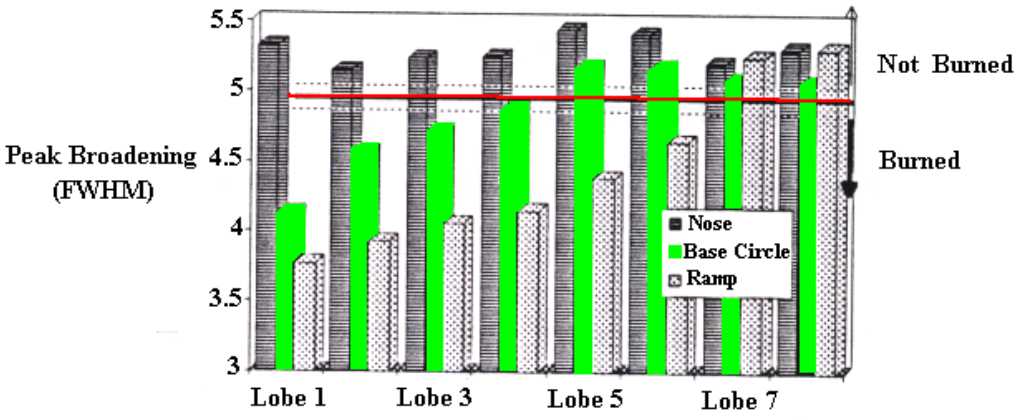

Figure 6.4. X-ray peak width response versus lobe number. Note that as the level of abusive grinding increased, the FWHM values decreased (narrowing) suggesting grinding burn (Courtney).

As the level of abusive grinding increases (going from right to left in Figure 6.4), the X-ray peak broadening decreases. This trend is more perceptible in the ramp that it is in the nose or base circle. Courtney defined a threshold value of FWHM (indicated by the horizontal red line) which identified if burn was present or not. Allison has made an in-depth study of this effect under CBN grinding and has confirmed the original hypothesis.

An analysis of the effect of fatigue engine testing on the X-ray diffraction peak width was performed on lobes examined previously by X-ray diffraction residual stress (Table 5.4). Plots of the X-ray peak width response versus depth for lobes tested in the SVI are seen in Appendix C. Results show inconclusive evidence of any correlation between FWHM values and residual stress. Surface FWHM values for most lobes (regardless of testing time) were grouped in the range of 2.5 to 3 degrees 2θ, a much lower value than any surface values observed by Courtney or Allison in research done with alumina and CBN grinding wheels, respectively. Figure 6.5 shows a plot of FWHM versus peak residual stress for selected lobes in all three camshafts of the present study.

The very low values of FWHM found in the opening ramp were accompanied by a grouping of the peak tensile residual stress in the range of 75 ksi to 125 ksi. Two out of the three FWHM values greater than 3 came from lobes 8 of shafts V-11 and V-15, suggesting that these lobes did not experience burn.

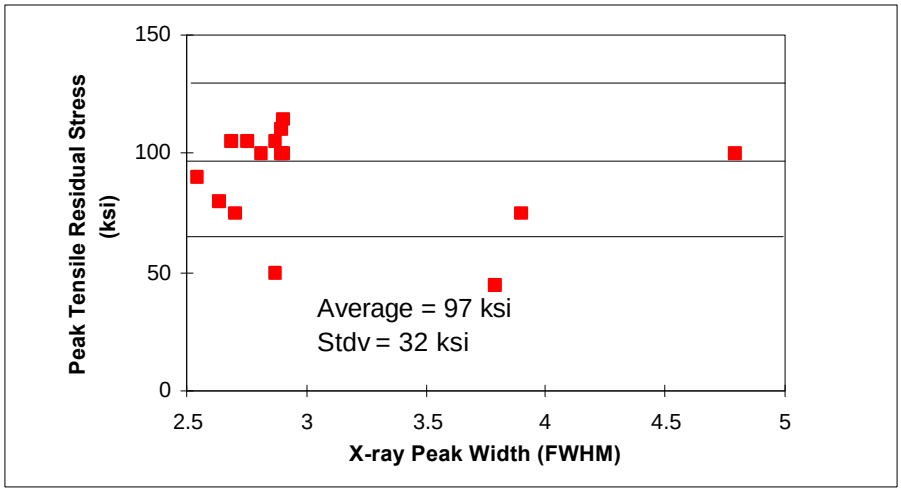

Figure 6.5. Peak residual stress versus full width half maximum (FWHM) value at the surface. Data were taken at the opening ramp, where most cracking occurred. Each point represents a surface measurement for all 16 lobes examined in all three camshafts (Table 5.4).

Peak narrowing should consort with an increase in uniformity in the crystal structure. What is then the effect of the rolling contact stresses on the structure of the steel? Residual stress relaxation is seen to decrease peak tensile residual stresses and drive them deeper into the material. We speculate that the driving force for this process is the plastic deformation followed by softening of the material due to the cyclic loading of the follower. Stored energy in the form of crystalline imperfections from cold work and heat treatment is relieved by this process. This driving force allows carbon atoms to diffuse in the martensitic structure (which is a metastable phase characterized by a distorted BCT lattice).

Chapter 7

CONCLUSIONS

I think and think for months and years. Ninety nine times, the conclusion is false, the hundredth time I am right — Albert Einstein, Life, January 9, 1950.

Following a fatigue and stress analysis of three SVI-tested camshafts, each fully characterized using nondestructive and destructive techniques, the following conclusions can be drawn:

1. Cracking occurred almost exclusively in the opening ramp of the most abusively ground lobes. It was induced by tensile residual stresses generated during grinding, and to a lesser extent by dynamic loading. Cracks were confirmed to propagate as deep as 300 μm below the surface of the lobe.

2. Residual stress relaxation was measured and confirmed to occur in the most abusively ground lobes after SVI engine testing. Peak tensile residual stresses were reduced and shifted deeper into the material. These residual stresses stabilized after a certain number of cycles, regardless of the level of grinding.

3. A correlation between residual stress and wear production is seen in the opening ramp of the tested lobes: formation of defects increases linearly with increasing subsurface peak tensile residual stress.

4. Two types of cracks were identified after simulated engine testing: straight and pitted. Nucleation of straight cracks occurs during grinding by the localized thermal expansion of the steel. Pitted cracks are nucleated by the synergistic effect of subsurface tensile residual stresses and impact loads generated by the follower during testing. Propagation of straight cracks has fatigue characteristics, with "lava flow" fracture surfaces suggesting lateral rubbing of crack surfaces due to cyclic loading. Propagation of pitted cracks is closely related to the process of pit formation (pieces of material are flake-off due to impact loading, leaving behind a pit). These cracks propagate by pits joining together.

5. Metallography and microhardness results confirm the rehardening of the most abusively ground lobe and the tempering of all other lobes. These results explain why cracking was inhibited in the first lobe, and promoted in the other lobes.

Chapter 8

REFERENCES

1 Hugnell, Anders & Anderson, Soren (n.d). *Simulating follower wear in a cam-follower contact S-100 44*, Stockholm, Sweden: Machine elements, Department of Machine Design. The Royal Institute of Technology.

2 Jemsen, P., *Cam Design and Manufacture* , Marcel Dekker Inc., New York, (1987).

3 Thiessen, F. and Dales, D., *Automotive Principles and Service*, Reston Publishing Co., Reston-Virginia, (1980).

4 Girardin, B., *Contact Stress Analysis and Fatigue Life Prediction for a Cam-Roller Follower System*, Master of Science Thesis, Blacksburg, Virginia: Virginia Polythechnic Institute and State University, (June 1994).

5 Courtney, S.G., *A Rapid Non-Destructive Test to Detect Camshaft Lobe Grinding Burn,* Master of Science Thesis, Blacksburg, Virginia: Virginia Polytechnic Institute, (December 1993).

6 Lugosi, R., Brauer, M. and Cook, J. *Assembled Camshaft for I.C Engines with Forged Powder Metal Cams,* SAE Paper 870129.

7 Clark, Joel P. and Field, Frank R. III. *An Economimc Assesment of Alternative Manufacturing Processes for the Camshaft,* SAE Paper 901741.

8 Hanard, M.R. *Production Grinding of Cam Lobes with CBN*, Technical Paper MR85-272, Society of Manufacturing Engineers, Dearborn, (1985)

9 Unterweiser, P.M., Boyer, H.E. and Kubbs, J.J. *Heat Treater s Guide: Standard Practices and Procedures for Steel*, ASM, Metal s Park, (1982), p. 205.

10 Harvey, Philip D., ed. *Engineeing Properties of Steel*, American Society for Metals, Metals Park (1991), pp. 154-159.

11 Krauss, G., *Steels: Heat treatment and Processing Principles*, (1990).

12 VanderVoort, G.F., ed. *Atlas of Time-Temperature Diagrams for Irons and Steels.* ASM Intl., Metal Park (1991), p.127.

13 Harvey, Philip D., pp. 154-159.

14 Shaw, Milton C. *Temperatures in Cutting and Grinding,* Transport Phenomena in Materials Processing — 1990, HTD-146, pp. 17-24, (November 25-30, 1990).

15 Malkin, S., *Grinding Technology- Theory and Applications of Machining with Abrasives*, Ellis Horwood Limited, (1989).

16 Dieter, George E., *Mechanical Metallurgy*, McGraw-Hill Book Co., New York, (1976), pp. 430-432.

17 Hertzberg, Richard W., *Deformation and Fracture Mechanics of Engineering Materials*, 3rd ed., John Wiley & Sons, (1976), pp20-26.

18 El-Helieby, S.O.A. and Rowe, G.W. *A quantitative Comparison between Residual Stresses and Fatigue Properties of Surface-Ground Bearing Steel (En 31),* Wear, 58, (1980), pp. 155-172.

19 James, M.R. *Relaxation of Residual Stresses ¾ An Overview,* Advances in Surface Treatments, Technology, Applications, Effects, Niku-Lari, A., Pergamon Press, (1987), pp. 349-365.

20 Landgraf R.W. and Chernenkoff R.A. *Residual Stress Effects in Fatigue,* Residual Stress Effects on Fatigue of Surface Processed Steels, ASTM, Champoux, R.L., Underwood, J.H. and Kapp, JA., Philadelphia, (1988), pp. 1-12.

21 Flavenot, J.F. *Effect of grinding conditions on fatigue behavior of 42CD4 Grade Steel. Fatigue Strength estimation incorporating residual stresses using different fatigue criteria,* Residual Stress in Science and Technology, 2, (1986), pp. 735-742.

22 Hahn, R.S. and Lindsay, R.P. *Principles of Grinding . . . Part II ¾ The metal removal parameter,* Grinding — Theory, Techniques and Troubleshooting, Batheja, C. and Lindsay, R., Society of Manufacturing Engineers, (1982), pp. 11-17

23 Herzog, R.; Sollich A. and Wohlfahrt, H. *Residual Stresses of Heat Treated Steels with Different Hardness after Grinding with Cubic Boron Nitride (CBN),* ICRS2 Conference Proceedings, (November 23-25, 1986), pp. 740-746.

24 Snoeys, R., Maris M. and Peters, J. *Thermally Induced Damage in Grinding,* Annals of the CIRP, 27 (2), (1978), pp. 571-581.

25 Moller G.V., *Residual Stress due to Grinding,* Master of Science Thesis, Blacksburg, Virginia: Virginia Polythechnic Institute and State University, (July 1995).

26 Cooper, W., *Kinematics and thermal modelling of industrial camshaft grinding,* PhD. Dissertation. University of California Los Angeles (August, 1995)

27 Skalli, N., Turbat, A., and Flavenot, J., *Prevision of Thermal Residual Stresses in Surface Plunge Grinding of Steels ,* Annals of the CIRP. 31(1), pp. 451-455.

28 Hahn, R.S. and Lindsay, R.P. *The Influence of Process Variables on Material Removal, Surface Integriy, Surface Finish and Vibration in Grinding,* 10th Int. MTDR Conference, pp 95-117, (1969).

29 Biggi, B., *The Effect of Grinding Protocol on Residual Stress in Simulated Cam Lobes ,* Report to Ford Motor Company, June 29, (1995).

30 Jensen, P.W., *Cam Design and Manufacture,* Marcel Dekker Inc., New York (1987), p. 95.

31 Jensen, P.W., pp 147-148.

32 Girardin, B., *Contact Stress Analysis and Fatigue Life Prediction for a Cam-Roller Follower System*, Master of Science Thesis, Blacksburg, Virginia: Virginia Polythechnic Institute and State University, (June 1994).

33 Hertz, H.R, J. Reine Angew. Math. (Crelle s J.), vol. 92, pp. 156-171 (1881) or Hertz, H.R., Miscellaneous Papers, pp. 146-162, Jones and Schott, London 1896.

34 Juvinall, R.C., *Stress, Strain and Strength*, pp. 370-397, McGraw-Hill 1967.

35 Smith, J.O. and Liu, C.K., *Stresses due to Tangential and Normal Loads on an Elastic Solid with Application to some Contact Problems,* Journal of Applied Mechanics, vol. 20, pp. 157-166, June 1953.

36 Girardin, B., *Contact Stress Analysis and Fatigue Life Prediction for a Cam-Roller Follower System*, Master of Science Thesis, Blacksburg, Virginia: Virginia Polythechnic Institute and State University, (June 1994).

37 Kano, M., and Kimura Y., *Quantitative Analysis of Cam Follower Wear in Relation to Various Material Properties* Wear,162-164, pp. 897-905, (1993).

38 Cam and Tappets: A Survey of Information; British Technical Council of the Motor and Petroleum Industries, December 1972.

39 Love R. J., and Wykes F. C., *The scuffing of Automotive Cams and Followers,* Tribology Practical Reviews, pp 75-80, May 1975.

40 Jiajun, L., Zhiqiang, L., and Yinqian C., *The Study of Scuffing and Pitting Failure of Cam-Tappet Rubbing Pair,* Wear, Vol.140, pp 135-147, (1990).

41 Keer, L. M., and Bryant, M. D., *A Pitting Model for Rolling Contact Fatigue* ASM Journal of Lubrication Technology, Vol. 105, pp 199-205, (1983).

42 Jiajun, L., Zhiqiang, L., and Yinqian C., p 138.

43 Smith, J.O. and Liu, C.K., p.157.

44 Friction, Lubrication, and Wear Technology, ASM Handbook, Vol. 18, pp 490-513.

45 Clarke, T. M., Miller, G. R., Keer, L. M., and Cheng, H. S., *The role of Near Surface Inclusions in the Pitting of Gears,* ASLE Trans., 1984.

46 Miller, G R., *On the Fatigue Analysis of Contact Mechanics,* Ph.D. thesis, Northwestern University, 1984.

47 Keer, L M., and Bryant, M. D., *A Pitting Model of Contact Fatigue,* ASME Journal of Lubrication Technology, Vol. 105, Apr. 1983, pp 198-205.

48 Kaneta, M., Mukarami, Y., and Yatsuzuka, H., *Analysis of Surface Crack Propagation in Lubricated Rolling Contact,* ASLE Trans., Vol. 28, pp 210-217, (1985)

49 Bower, A.F., *The Influence of Crack Face Friction and Trapped Fluid on Surface Initiated Rolling Contact Fatigue Cracks,* ASME Journal of Tribology, Vol. 110, pp704-711, (1988).

50 Styri, H., *Fatigue Strength of Ball Bearing Races and Heat Treated 52100 Steel Specimens,* Porceedings, ASTM, Vol. 51, p 682, (1951).

51 Littman, W. E., and Widner, R. L., *Propagation of Contact Fatigue from Surface and Subsurface Origins,* Journal of Basic Engineering, Trans. ASME, Vol 88, pp 624-636, (1966).

52 Fleming, J. F., and Suh, N. P., *Mechanics of Crack Propagation in Delamination Wear,* Wear, Vol. 44, pp. 39-56, (1977).

53 Kaneta, M., Mukarami, Y., and Yatsuzuka, H., p. 138.

54 Girardin, B., pp 54-65.

55 Dowling, N. E., *Mechanical Behavior of Materials*, pp233-275, Prentice Hall 1993.

56 Allison, H. D., Master of Science Thesis under preparation, Material Science and Engineering Department, Virginia Polytechnic Institute and State University.

57 Briggs, G. A. D., *An Introduction to Scanning Acoustic Microscopy* , Royal Microscopical Society Hadbook 12, Oxford University Press, (1985).

58 Yamanaka, K., and Enomoto Y., *Observation of Surface Cracks with Scanning Acoustic Microscope,* Journal of Applied Physics, Vol. 53, pp 846-850, (1982).

59 Briggs, G. A. D., *An Introduction to Scanning Acoustic Microscopy,* RMS Hadbook, Vol. 12, (1985).

60 Yamanaka, K., and Enomoto Y., (1982).

61 Yamamoto, T., Crack Growth in Lubricated Rollers, in Solid Contact and Lubrication, Ed. H. S. Cheng and L. M. Keer, ASME AMD, Vol. 39, 1980, pp. 223-236.

62 Dowling, N. E., p 358.

63 Doerner, M. F., and Nix W. D., *A Method for Interpreting the Data from Depth-sensing Indentation Instruments,* Journal of Matrerials Research, Vol 1 No. 4, pp 601-609, (Jul/Aug 1986)

64 Oliver, W. C., and Pharr, G. M., *An Improved Technique for Determining Hardness and Elastic Modulus using Load and Displacement Sensing Indentation Experiments,* Journal of Materials Research, Vol.7 No. 6, pp 1564-1583, (June 1992)

65 Oberg, E., Jones, F., Horton, H.L. and Ryffel, H.H., Machinery s Handbook, 24th ed., Industrial Press, New York, (1992), p.494.

66 Dieter, p.399.

67 Cullity, B.D., Elements of X-ray Diffraction, 2nd ed., Addison-Wesley, (1978), p. 446.

68 Lieurade, H. P., *Advances is Surface Treatments* Vol. 4 Residual Stresses, Pergamom Press, New York, p 455.

69 Wohlfahrt, H., *Kugelstrahlen und Dauerschwingverhalten ,* 1st in Conference on Shot Peening, Paris. Edit. Pergamom Press, (1981).

70 Biggi, B., *The Effect of Grinding Protocol on Residual Stress in Simulated Cam Lobes* , Report to Ford Motor Company, June 29, (1995).

71 Courtney, S.B., *A Rapid Non-Destructive Test to Detect Camshaft Lobe Grinding Burn,* Master of Science Thesis, Blacksburg, Virginia: Virginia Polytechnic Institute, (December 1993).

72 Courtney, S.B., p. 56.

73 Legus, El Haddad, Topper. The effect of cold rolling on the fatigue properties of a SAE 1010 steel in Materials experimentation and design in fatigue . Proc. of Fatigue 81 - Westbury House, P. 97-105.

74 Girardin, B., *Contact Stress Analysis and Fatigue Life Prediction for a Cam-Roller Follower System*, Master of Science Thesis, Blacksburg, Virginia: Virginia Polythechnic Institute and State University, (June 1994).

75 Landgraf, R. W. and Chernenkoff, R. A., Residual Stress Effects on Fatigue on Surface Processed Steels, Analytical and Experimental Methods for Residual Stress Effects in Fatigue, ASTM STP 1004, R.L. Champoux, J.H. Underwood and J. A. Kapp Eds., American Society for Testing and Materials, Philadelphia 1988, pp. 1-12.

76 Flavenot, J. F. and N. Skalli (1983) Fatigue Strength Estimation incorporating residual stresses. Annals of the CIRP, Vol. 32.1.

77 Courtney, S.B., *A Rapid Non-Destructive Test to Detect Camshaft Lobe Grinding Burn,* Master of Science Thesis, Blacksburg, Virginia: Virginia Polytechnic Institute, (December 1993).

APPENDIX A: EXPERIMENTAL MATRIX

	LOBE #	1	2	3	4	5	6	7	8
V-11	**# OF CRACKS**	1 (336 hours)	3 (100 hours)	5 (336 hours)	1 (250 hours)	NONE (75 hours)	1 (250 hours)	NOT LOADED	NONE (336 hours)
V-11	**DEGREE OF WEAR**	**1**	**1**	**1**	**2**	**3**	**3**	**3**	**3**
V-11	**GROOVE SIZE**	**-**	**-**	**-**	**-**	**-**	**-**	**-**	**-**
V-11	**RESIDUAL STRESS**	**opening ramp**		**opening ramp**	**opening ramp**	**opening ramp**	**opening ramp**		**opening ramp**
V-11	**CRACK MECHANICS**	**-**	**-**	**-**	**-**	**-**	**-**	**-**	**-**
V-11	**HARDNESS**		**base circle, ramps, nose**					**base circle, ramps, nose**	

CS#	**# OF CRACKS**	1 (336 hours)	5 (150 hours)	5/ (150 hours) WEIRD CRACK ON CLOSING RAMP	NOT LOADED	2 (336 hours)	3 (336 hours)	NONE (336 hours)	NONE (150 hours)
V-13	**DEGREE OF WEAR**	**2**	**1**	**1**	**-**	**2**	**2**	**3**	**3**
V-13	**GROOVE SIZE**	**-**	**-**	**-**	**-**	**-**	**-**	**-**	**-**
V-13	**RESIDUAL STRESS**		**opening ramp**		**opening ramp**	**opening ramp**	**opening ramp**		
V-13	**HARDNESS**	**base circle, ramps, nose**							
V-13	**CRACK MECHANICS**	**-**	**-**	✓	**-**	**-**	**-**	**-**	**-**

CS#	**# OF CRACKS**	NONE	2	2	NONE	NONE	1	NONE	NONE
V-15	**DEGREE OF WEAR**	2	1	1	2	2	2	3	3
V-15	**GROOVE SIZE(μin)**	-	2500	2100	200	250	600	1800	900
V-15	**RESIDUAL STRESS**	**opening ramp**	**opening ramp**		**opening ramp**	**opening ramp**	**opening ramp**		**opening ramp**
V-15	**CRACK MECHANICS**	-	-	✓	-	-	-	-	-
V-15	**HARDNESS**							**base circle, ramps, nose**	

DEGREE OF WEAR: 1-HEAVLY DAMAGED 2-MODERATELY DAMAGED 3- NO DAMAGE

APPENDIX B: WEAR HISTOGRAMS

CAMSHAFT V-11

LOBE 1

336 hours

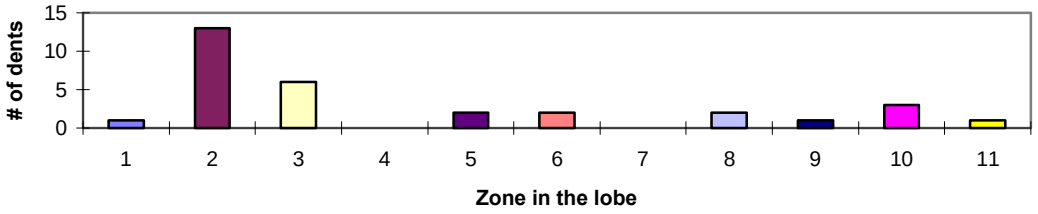

LOBE 2

100 hours

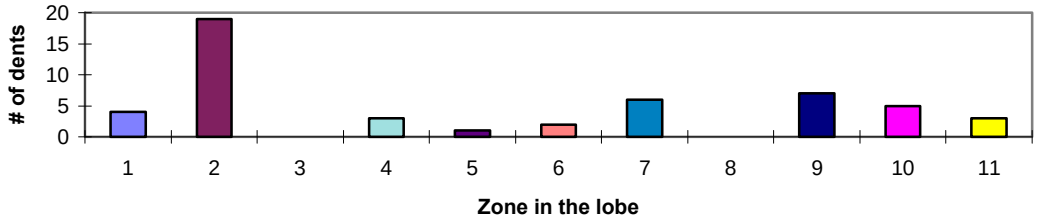

LOBE 3

336 hours

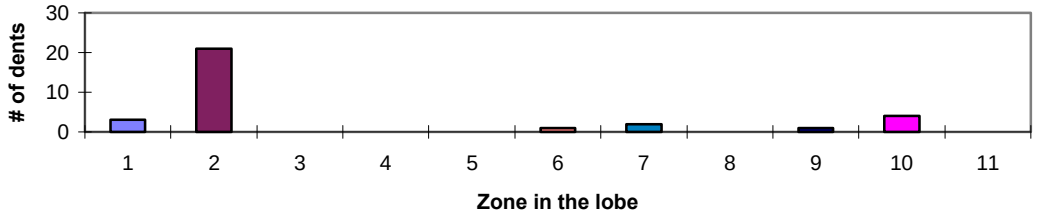

LOBE 4

250 hours

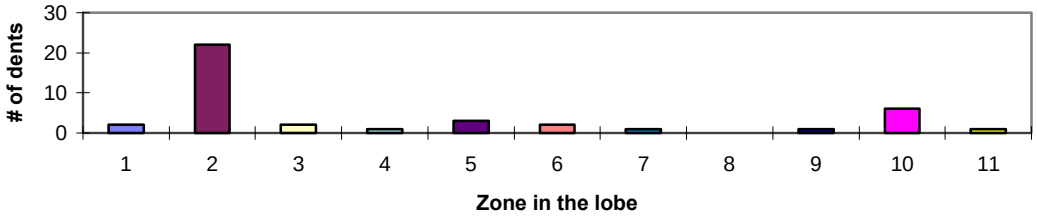

CAMSHAFT V-11

LOBE 5
75 hours

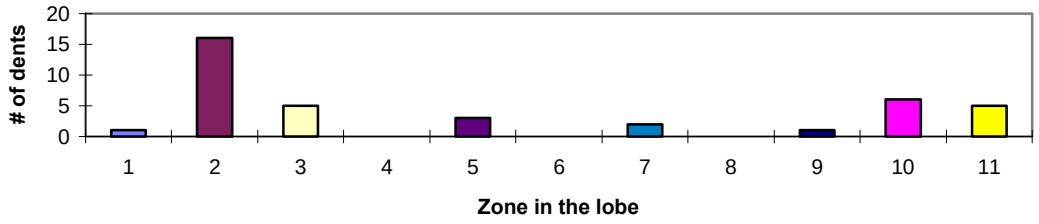

LOBE 6
250 hours

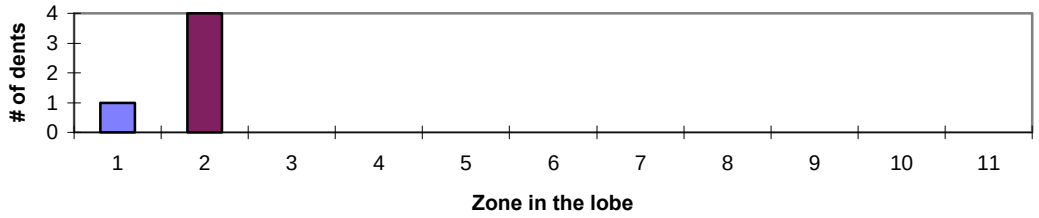

LOBE 8
336 hours

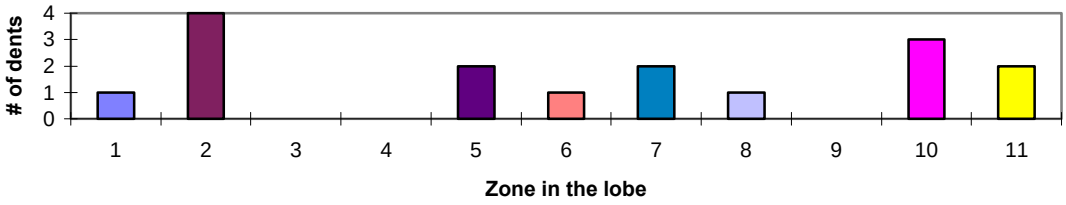

CAMSHAFT V-13

LOBE 1

336 hours

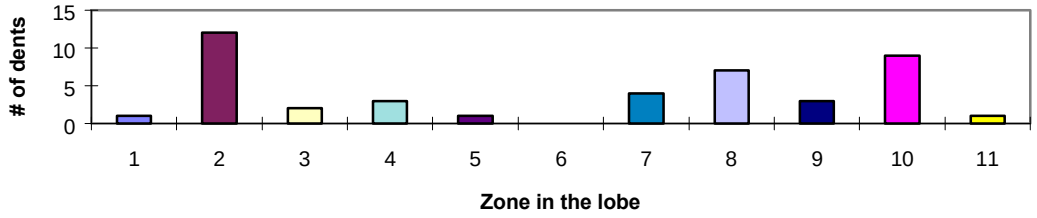

LOBE 2

150 hours

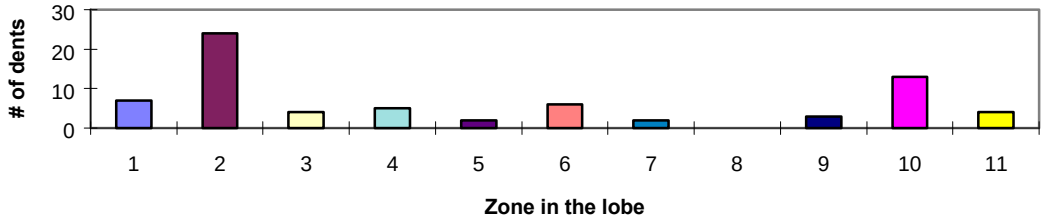

LOBE 3

150 hours

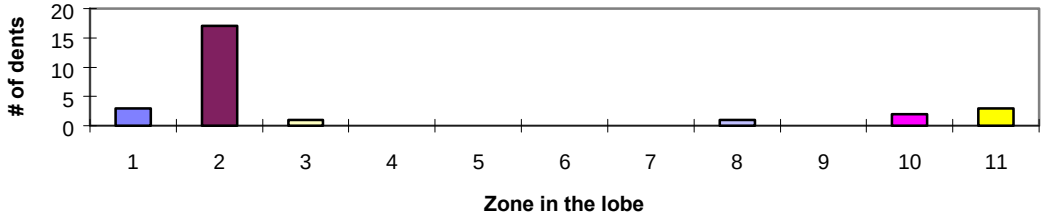

LOBE 5

336 hours

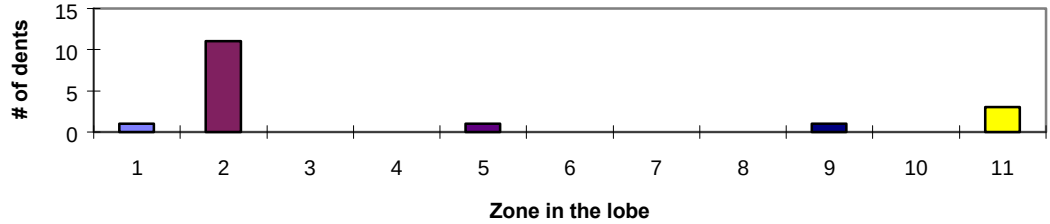

CAMSHAFT V-13

LOBE 6
336 hours

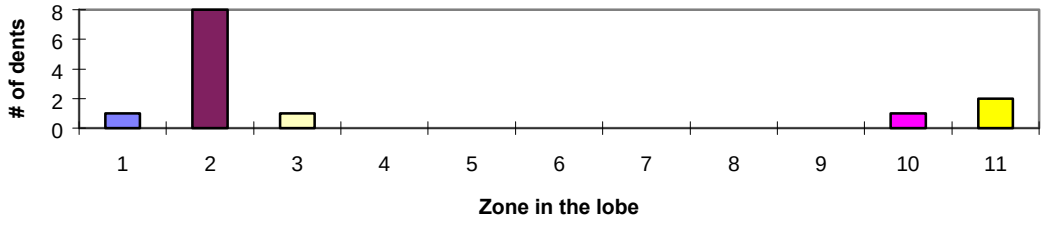

LOBE 7
336 hours

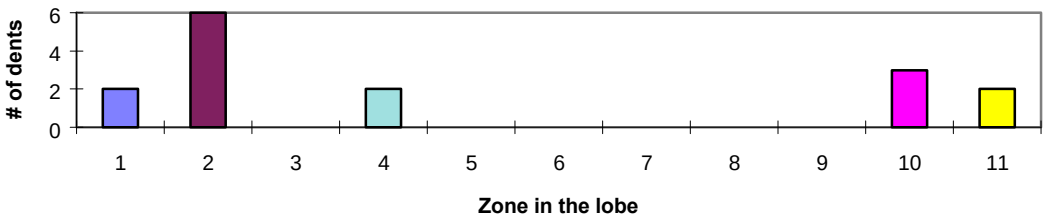

LOBE 8
150 hours

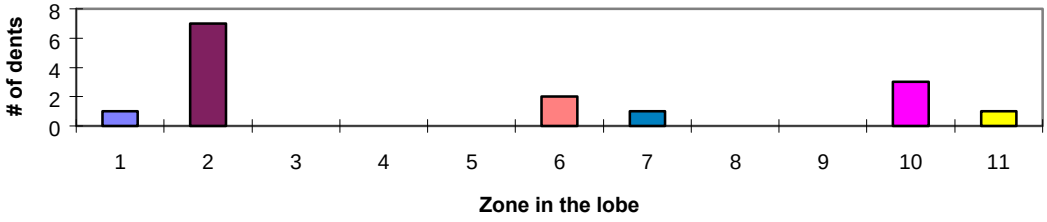

CAMSHAFT V-15

LOBE 1

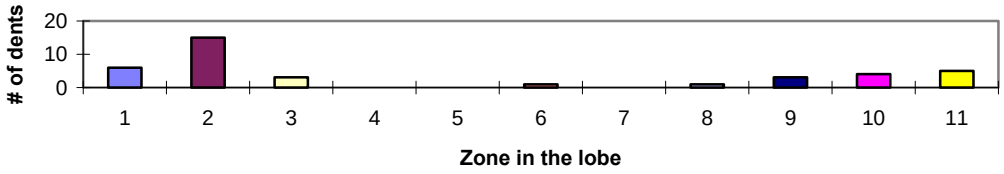

LOBE 2

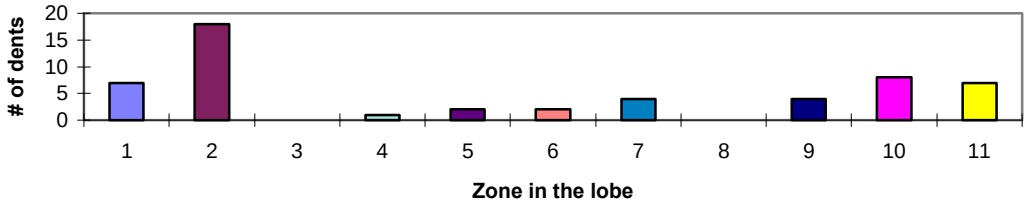

LOBE 3

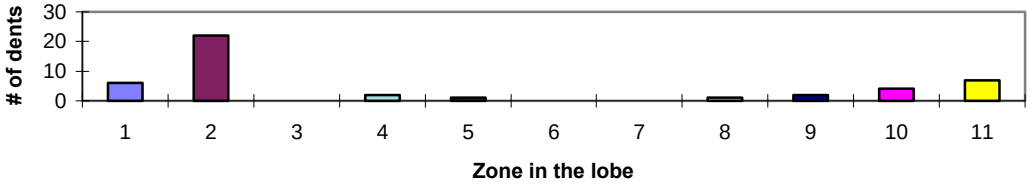

LOBE 4

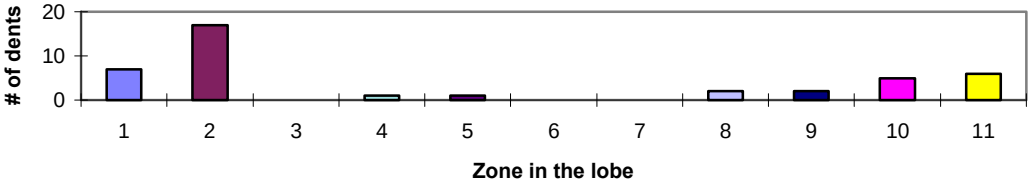

CAMSHAFT V-15

LOBE 5

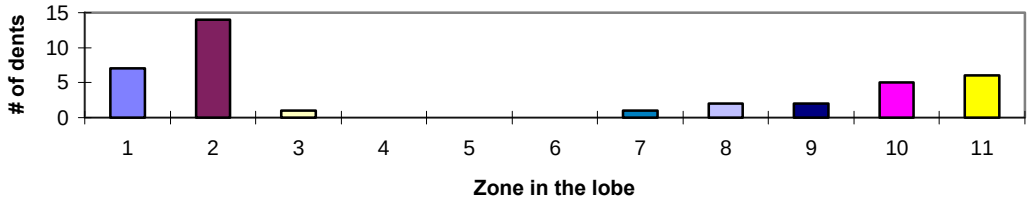

LOBE 6

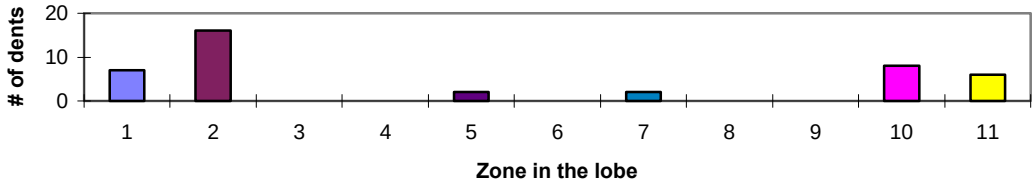

LOBE 7

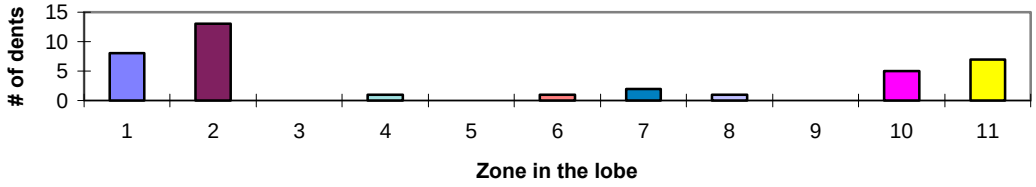

LOBE 8

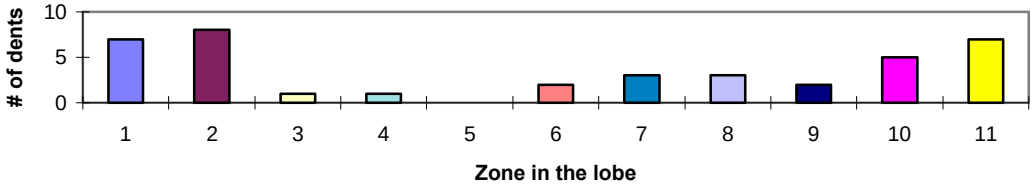

APPENDIX C:
FWHM DATA FOR CAMSHAFT V-11

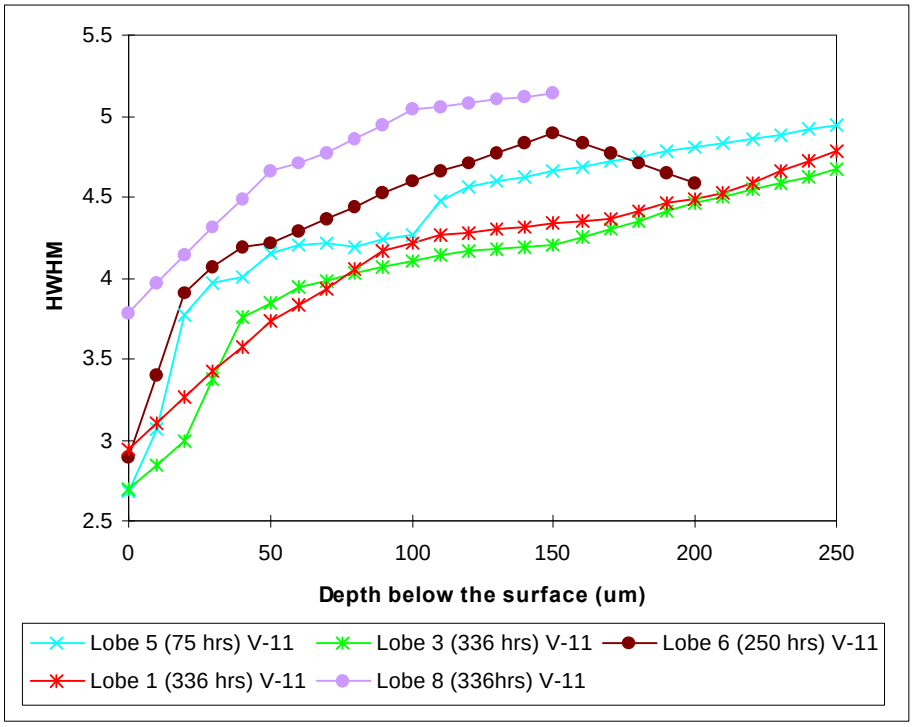

APPENDIX C: FWHM DATA FOR CAMSHAFT V-13

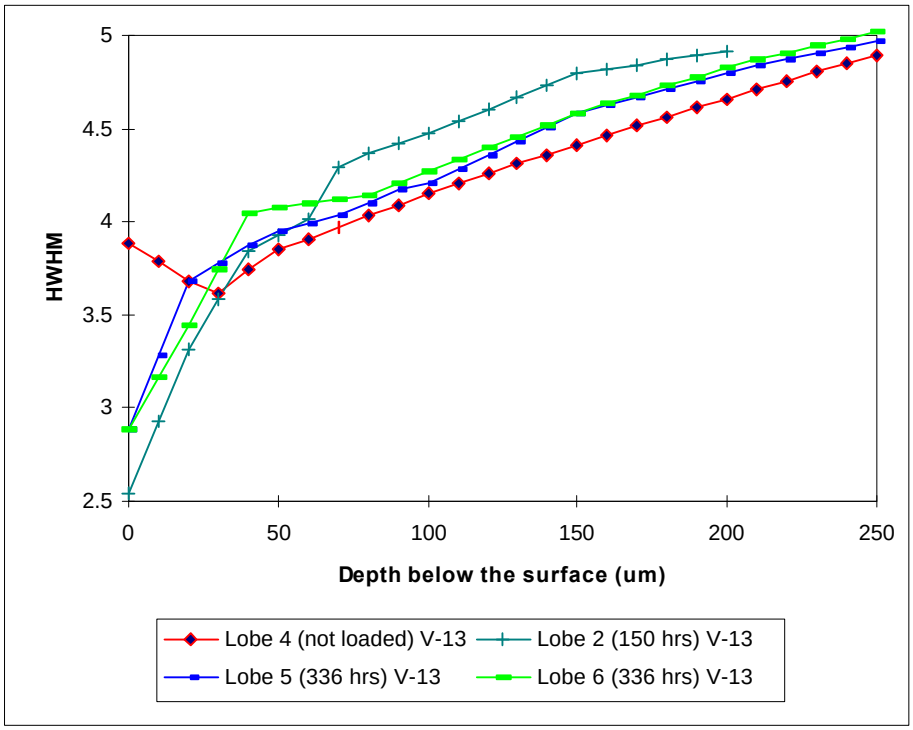

APPENDIX C: FWHM DATA FOR CAMSHAFT V-15

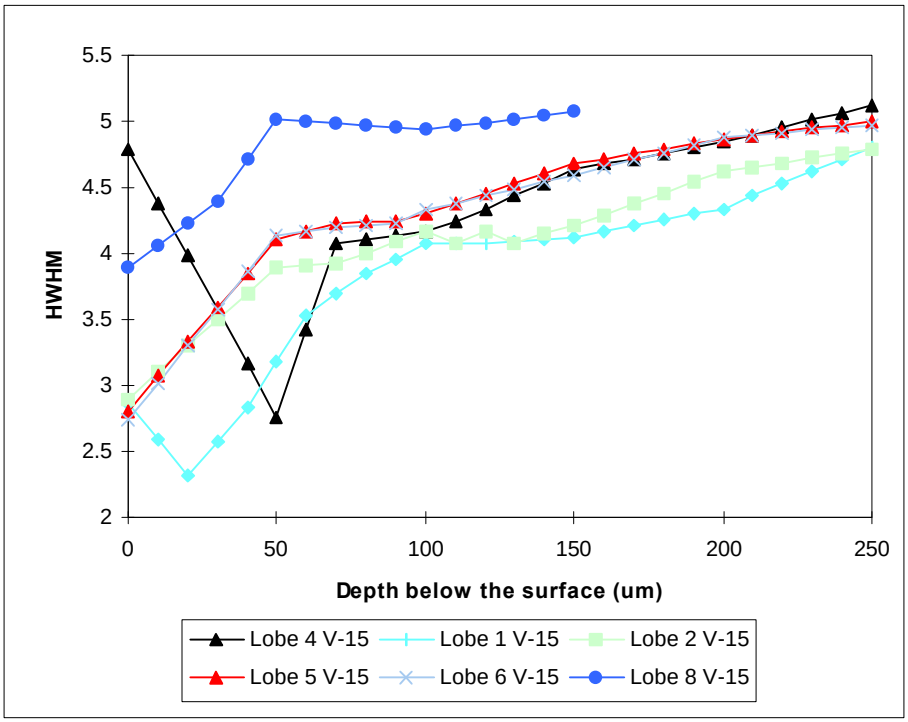

VITA

Jose Alejandro Escobar was born January 6, 1972 to Ricardo Escobar and Marcela Granier. His birthplace, Cochabamba, is a beautiful Bolivian city situated on the valley flanks of the colossal Andes mountain chain. At the age of two, his family moved to Costa Rica, leaving behind a country ruled by a repressive military regime. The author spent his childhood years happily in the southern-most part of the country, in the middle of banana and oil palm plantations. In 1981, a promising future led his family to move to Manaus, the capital city of the Brazilian state of Amazon. Here, he was re-alphabetized in Portuguese.

In 1987, in the most important decision in his life, Escobar moved yet another time to Bangkok, Thailand. The Land of the Smiles had a profound impact on his life. He was overwhelmed by the beauty, richness and sophistication of Thai culture. Though he never could master the Thai language, he appropriated many facets of the Thai s way of life, social values, and Theravada Buddhism. Escobar enrolled in an American high school, which imposed a greater challenge than he thought. In order to graduate on time, Escobar had to learn English in seven months before being asked to read and interpret works by William Shakespeare and Nathaniel Hawthorne. This experience, however, opened new horizons in his life. Two years later he would be leaving for the United States in pursuit of an engineering degree at Virginia Polytechnic Institute and State University. He earned his bachelor s degree from the Materials Science and Engineering department in May of 1994. Convinced that he needed to expand his education, he returned to Virginia Tech in pursuit of a Master s degree in the same field. Upon completion, the author plans to return to Latin America in search of a fulfilling professional career.